

UNCLASSIFIED

AD 400 946

*Reproduced
by the*

ARMED SERVICES TECHNICAL INFORMATION AGENCY
ARLINGTON HALL STATION
ARLINGTON 12, VIRGINIA



UNCLASSIFIED

NOTICE: When government or other drawings, specifications or other data are used for any purpose other than in connection with a definitely related government procurement operation, the U. S. Government thereby incurs no responsibility, nor any obligation whatsoever; and the fact that the Government may have formulated, furnished, or in any way supplied the said drawings, specifications, or other data is not to be regarded by implication or otherwise as in any manner licensing the holder or any other person or corporation, or conveying any rights or permission to manufacture, use or sell any patented invention that may in any way be related thereto.

63-3-1

①

946

AD No. ~~400~~

ASTIA FILE COPY

⑤ 16 600

400 946

Ford Motor Company
AERONUTRONIC DIVISION

ASTIA
APR 12 1963
S/A

16 11 50

RE-ENTRY SYSTEMS PROGRAM,

⑦ TECHNICAL NOTE on

⑥ STUDY OF HYPERSONIC FLOW FIELDS AND
AERODYNAMIC FORCES ON SHARP CONES AT
ANGLE OF ATTACK IN LOW-DENSITY FLOW.

Prepared for: Ballistics Systems Division
United States Air Force
Los Angeles, California

⁽¹²⁾
~~Under~~ Contract: AF 04(694)-23

⑬ NA

⁽⁵⁾
~~Prepared~~ by: W. Leon Francis and
C. O. White

⑨ 27 November 1962, ⑩ 1v. incl. illus. tables, 35 refs.

ABSTRACT

↓

This report summarizes the results of a series of studies to establish engineering methods for estimating the flow fields and aerodynamic forces over sharp cones during hypersonic re-entries. The effects of ablation and turbulent flow are not considered.

The flow fields and aerodynamic forces on sharp cones at zero angle of attack are first examined by a comparison of various techniques of determining the boundary layer displacement thickness and shock wave geometry. Good agreement is obtained between a modified viscous interaction theory and experimental force data. The work is then extended using viscous interaction theory to obtain a correlation of experimental data for flow conditions ranging from continuum to free molecule flow. The approximate form of the interaction theory derived shows that the parameter, $M^{3/4}/\sqrt{Re}$, is the proper correlating parameter for the drag of slender cones over a wide range of Mach numbers and Reynolds numbers. Excellent agreement is obtained for experimental data correlated according to this parameter.

↑

The zero angle of attack case is then extended to include the effects of the angle of attack range, 0 to 90 degrees, on the aerodynamic forces and the flow properties at the most windward streamline. Comparison was again made between the theory and experiment, where generally good agreement was found to exist.

This work was conducted by Aeronutronic Division of Ford Motor Company under Contract AF 04(694)-23 to the Ballistic Systems Division of the United States Air Force.

CONTENTS

| CHAPTER | | PAGE |
|---------|---|------|
| 1 | INTRODUCTION. | 1-1 |
| 2 | REVIEW OF VISCOUS INTERACTION THEORY | |
| | 2.1 General. | 2-1 |
| | 2.2 Sharp Flat Plate | 2-1 |
| | 2.3 Sharp Cone | 2-16 |
| 3 | BOUNDARY LAYER GROWTH AND SHOCK SHAPE ON SHARP CONES AT ZERO ANGLE OF ATTACK | |
| | 3.1 Comparison of Analytical Methods for Boundary Layer Growth | 3-1 |
| | 3.2 Determination of Equivalent Power Law Body and Shock Shape. | 3-20 |
| 4 | FLOW FIELD DETERMINATION OVER 6.33 AND 10 DEGREE SEMI- VERTEX ANGLE CONES | |
| | 4.1 Boundary Layer and Shock Layer Profiles. | 4-1 |
| | 4.2 Heat Transfer and Skin Friction on Cones | 4-2 |
| | 4.3 Axial Force Coefficient at Zero Angle of Attack. | 4-11 |
| 5 | APPROXIMATE INTERACTION THEORY AND EXPERIMENTAL CORRELATION | |
| | 5.1 Approximate Interaction Theory | 5-1 |
| | 5.2 Derivation of Correlation Parameters for Cone Drag | 5-9 |
| | 5.3 Correlation of Experimental Data | 5-18 |
| 6 | FLOW OVER CONES AT ANGLE OF ATTACK | |
| | 6.1 General. | 6-1 |
| | 6.2 Laminar Boundary Layer on a Cone at Angle of Attack | 6-2 |
| | 6.3 Shock Shape at Arbitrary Angle of Attack | 6-6 |

CONTENTS (Continued)

| CHAPTER | | PAGE |
|---------|---|------|
| 7 | THEORETICAL ESTIMATES OF AERODYNAMIC FORCE COEFFICIENTS AT ANGLE OF ATTACK | |
| | 7.1 Axial Forces at Small Angle of Attack. | 7-1 |
| | 7.2 Normal and Moment Forces at Small Angle of Attack | 7-4 |
| | 7.3 Small Angle of Attack, $\alpha > \sigma$ | 7-7 |
| | 7.4 Center of Pressure | 7-9 |
| | 7.5 Aerodynamic Forces at Large Angle of Attack. | 7-9 |
| | 7.6 Comparison of Experiment and Theory. | 7-14 |
| 8 | NOMENCLATURE. | 8-1 |
| 9 | REFERENCES. | 9-1 |
| | APPENDIX. | A-1 |

ILLUSTRATIONS (Continued)

| FIGURE | PAGE |
|--------|--|
| 3-7 | Comparison of Pressure Distributions on a Cone. 3-18 |
| 3-8 | Induced Pressure Increment on a Cone (Data of Reference 17) 3-19 |
| 3-9 | Deviation of Empirical Body Radius from Exact Solution. . 3-22 |
| 3-10 | Approximate Solution for Hypersonic Flow Over Power Law Bodies (NASA TR R-15) 3-24 |
| 4-1 | Comparison of Enthalpy Distributions for Effect of Pressure Gradient 4-3 |
| 4-2 | Boundary Layer Thickness. 4-4 |
| 4-2.A | Shock Layer Thickness 4-4 |
| 4-3 | Shock Layer Densities 4-5 |
| 4-3.A | Shock Layer Temperatures. 4-5 |
| 4-4 | Temperature Distributions Across Boundary Layer 4-6 |
| 4-5 | Density Distributions Across Boundary Layer 4-7 |
| 4-6 | Temperature Distributions Across Boundary Layer 4-8 |
| 4-7 | Density Distribution Across Boundary Layer. 4-9 |
| 4-8 | Comparison of Theory and Experiment for Axial Force Coefficient 4-13 |
| 4-9 | Comparison Between Experiment and Theory 9° Cone. 4-16 |
| 4-10 | Comparison Between Experiment and Theory 6.3° Cone. 4-17 |
| 5-1 | Comparison Between Experiment and Approximate Theory. . . 5-10 |
| 5-2 | Correlation of Theoretically Calculated Drag Curves . . . 5-16 |

ILLUSTRATIONS (Continued)

| FIGURE | | PAGE |
|--------|---|------|
| 5-3 | Correlation of Experimental Data. | 5-22 |
| 6-1 | Interaction Parameter, $\bar{\chi}_c$, at Stagnation Line on Cone . . | 6-5 |
| 6-2 | Comparison of Methods for Computing Conical Shock Angles. | 6-8 |
| 6-3 | Comparison of Theory and Experiment for Shock Angle on Slender Cones | 6-11 |
| 6-4 | Shock Angle on Cone at Angle of Attack. | 6-12 |
| 7-1 | Variation of g_w' with Angle of Attack | 7-13 |
| 7-2 | Variation of \bar{f}_w' with Angle of Attack. | 7-15 |
| 7-3 | Comparison of Theory and Experiment (Normal Coefficient). . | 7-16 |
| 7-4 | Comparison of Theory and Experiment Axial Coefficients. . | 7-17 |
| 7-5 | Comparison of Theory and Experiment (Moment Coefficients) | 7-17 |
| 7-6 | Comparison of Theory and Experiment (Axial Force Coefficient). | 7-18 |
| 7-7 | Comparison of Theory and Experiment (Normal Force Coefficient). | 7-19 |
| 7-8 | Comparison of Theory and Experiment (Normal Force Coefficient). | 7-19 |
| 7-9 | Comparison of Theory and Experiment (Moment Force Coefficient). | 7-20 |
| 7-10 | Comparison of Theory and Experiment (Moment Force Coefficient). | 7-20 |
| 7-11 | Axial Force Coefficient Versus Angle of Attack. | 7-23 |
| 7-12 | Normal Force Coefficient Versus Angle of Attack | 7-24 |
| 7-13 | Moment Force Coefficient Versus Angle of Attack $M_\infty \approx 14$. | 7-25 |
| 7-14 | Comparison of C_a for Sharp and Blunt Slender Cones at Angle of Attack | 7-28 |

CHAPTER 1

INTRODUCTION

The development of improved heat shields and a desire for increased terminal velocities have led to increased interest in slender body configurations for re-entry vehicles. The investigation of the flow fields and aerodynamic characteristics in the high speed, high altitude regime is complicated by the effects of viscous interaction. The considerable distortion of the flow field over slender bodies in hypersonic, low-density flow due to boundary layer displacement effects has been extensively examined qualitatively¹. Quantitative results have been presented for special cases, but numerical answers directly applicable to the cone under re-entry conditions are scarce. Since it is not generally possible to match wind tunnel Mach number and Reynolds number test conditions to those encountered in flight, there has been a heavy emphasis on the use of theory for predicting flight characteristics. In addition, hypersonic theory has not yet been developed to the point where solutions are available for all density regimes from free molecule to continuum flow.

In order that engineering estimates might be made of flow field and aerodynamic characteristics, without resorting to high speed computing machines, it is common to make certain assumptions to simplify the complex equations of motion. For example, the use of constant density theory in hypersonic flow has provided results for inviscid conical flow² which is highly accurate, yet gives analytical expressions adaptable to hand calculations. The assumption of a constant density should in no way be taken to imply an incompressible flow, but rather to be particularly applicable in hypersonic flows where thin shock layers occur. The general premise underlying the present work is that the local flow field can be sufficiently described for engineering purposes if the boundary layer growth and resultant shock wave can be computed independently of any considerations other than free-stream conditions and body geometry. A considerable amount

Ford Motor Company

AERONAUTRONIC DIVISION

of information about the flow field can be specified from the local slope of the shock wave. This "inverse" method has two major advantages; (1) boundary conditions are provided with the deletion of one independent parameter so as to do away with the usually required simultaneous solution of several equations, and (2) the matching of the inviscid and viscous flow regions is automatically satisfied by the use of the equivalent body in obtaining the shock wave position. The major disadvantage is, of course, the uncertainty in the basic assumption itself. In the present case, existing methods (compressible laminar boundary layer and/or viscous interaction theories) or developments thereof, will be used to estimate the boundary layer growth.

This continuum flow solution, including the effects of viscous interaction, provides a firm basis for the understanding of the behavior and trends exhibited as the density is decreased. In the absence of a solution for the complete flow regimes, a correlation of experimental data appears most promising for engineering designs. This is also accomplished in the present investigation for the zero angle of attack case.

CHAPTER 2

REVIEW OF VISCOUS INTERACTION THEORY

2.1 GENERAL

At low Reynolds numbers and/or high Mach numbers the boundary layer becomes significantly large that it produces an outward deflection of the stream surfaces and perturbs the local inviscid flow field. This perturbation of the inviscid flow field results in an "induced" pressure change on the body which, in turn, affects the growth of the viscous boundary layer and also the local skin friction. This problem of boundary-layer-shock wave interactions has been under intensive investigation for some time and a number of solutions of varying degrees of accuracy are available. Because of the mutual effects of the boundary layer on the shock wave and the shock wave on the boundary layer, it is to be expected that the most accurate interaction solutions are those of the type involving an iterative procedure. These procedures are cumbersome and time consuming, therefore a number of approximate theories have been developed which are applicable over certain ranges. The original theory developed by Lees and Probstein³ is used as the basis for these interaction theories. It has been amply examined (Reference 4-6), and only a brief review of the applicable equations will be given here. An iterative procedure will be discussed subsequently.

2.2 SHARP FLAT PLATE

Before proceeding to the cone, the case of the sharp flat plate will be examined. In the case of the flat plate, it has been found convenient to divide the interaction effects into two asymptotic regions called the weak and strong interaction zones.

For the weak interaction zone the effects produced by the self induced pressure gradient are considered to be essentially perturbations superimposed on an already existing uniform flow. Under these conditions, the boundary layer growth is essentially unaffected by the pressure gradient. For the strong interaction region, on the other hand, the increment in flow deflection caused by the boundary layer is of the same order of magnitude as that caused by the body and the pressure gradient is considered to have a direct influence.

The usual division between the strong and weak interaction regimes is written:

- a) $\bar{\chi} < 1$ weak interaction
b) $\bar{\chi} > 1$ strong interaction

where $\bar{\chi}$ is the hypersonic interaction parameter defined as:

$$\bar{\chi} = \frac{M^3 \sqrt{C}}{\sqrt{Re}}$$

where C is the coefficient in the linear viscosity-temperature relationship. This relationship is used to simplify the boundary layer equations to obtain closed form solutions for the boundary layer parameters. Because temperature affects both the density and viscosity of a fluid, it is apparent that the drag on a body (from interaction and skin friction sources) is a function of the temperature distribution through the boundary layer. This temperature distribution is related to the body wall temperature. While exact numerical solutions for the boundary layer characteristics for various temperature distributions are available⁷, it has been found convenient from an analytic point of view to use a linear variation of viscosity with temperature of the form:

$$\frac{\mu_{ref}}{\mu} = C \frac{T_{ref}}{T}$$

It was originally proposed¹ that the reference conditions be evaluated at the body wall. Now, since the temperature (and viscosity) vary by large amounts across the boundary layer, it is apparent that a considerable variation in C may also occur. It would therefore seem that the most realistic evaluation of C would be at some mean boundary layer temperature, rather than the wall temperature.

Ford Motor Company
AERONUTRONIC DIVISION

A number of authors have submitted various recommendations as to how the reference conditions should be evaluated.

Talbot, Koga and Sherman⁸ use:

$$T_{\text{ref}} = T' \equiv T_w - 0.486 \text{ Pr}^{1/3} (T_w - T_{\text{Aw}}) - 0.273 \text{ Pr} \left(\frac{\gamma - 1}{2} \right) M_c^2 T_c$$

where Pr = Prandtl number

T_{Aw} = Adiabatic wall temperature

Cheng, Hall, Golian, and Hertzberg⁹ recommend simply the average temperature across the hypersonic boundary layer:

$$T_{\text{ref}} = T' \equiv T_0 [1 + 3 (T_w/T_0)] / 6$$

T_0 = Free stream stagnation temperature

Sommer and Short¹⁰ give:

$$T_{\text{ref}} = T'' \equiv T_c + 0.032 T_c M_c^2 + 0.58 (T_w - T_c)$$

Eckert's semi empirical reference enthalpy¹¹ gives:

$$T_{\text{ref}} = T^* \equiv 0.5 (T_w + T_c) + 0.22 \text{ Pr}^{1/2} \left(\frac{\gamma - 1}{2} \right) M_c^2 T_c$$

It appears, on the basis of experimental evidence, that Eckert's reference enthalpy method gives the best results. However, the numerical differences between the various reference temperatures are generally quite small. Table I compares reference temperature calculated by the above four methods for various assumed Mach numbers and Prandtl numbers.

For the remainder of this discussion only Eckert's reference temperature method will be considered. In the case of a dissociated boundary layer flow, a reference enthalpy will be used,

Ford Motor Company,
AERONUTRONIC DIVISION

$$h^* = 0.5 (h_w + h_e) + 0.22 \text{Pr}^{1/2} U_e^2/2$$

where the reference temperature, T^* , is to be obtained from a Mollier diagram at (h^*, P_2) .

Once the reference temperature is established, the viscosity proportionality constant C_c may be evaluated by means of either the power law or the Southerland formulation. The power law leads to a simpler algebraic relation, but its applicability is limited to more restricted temperature range than the Southerland equation.

From the power law ($\omega = 0.76$):
(applicable in the range $170^\circ\text{K} < T < 500^\circ\text{K}$)

$$C_c = \left(\frac{T_c}{T_{\text{ref}}} \right)^{0.24}$$

whereas for the Southerland formula:

$$(100^\circ\text{K} < T < 1900^\circ\text{K})$$

$$C_c = \frac{\left(1 + \frac{110^\circ\text{K}}{T_{\text{ref}}} \frac{T_{\text{ref}}}{T_c} \right)}{\left(1 + \frac{110^\circ\text{K}}{T_{\text{ref}}} \right)} \left(\frac{T_c}{T_{\text{ref}}} \right)^{1/2}, \quad T \propto ^\circ\text{K}$$

or

$$C_c = \left(\frac{T_{\text{ref}}}{T_c} \right)^{1/2} \left(\frac{T_c + 199}{T_{\text{ref}} + 199} \right), \quad T \propto ^\circ\text{R}$$

It can be shown that the use of Eckert's equation to determine the reference temperature together with the Southerland formulation to determine the viscosity coefficient gives boundary layer solutions that are within about 4 percent of the correct values calculated numerically by Van Driest.

TABLE I
REFERENCE TEMPERATURE COMPARISON

| | $M_c = 0$ | | | | $M_c = 10$ | | | | $M_c = 20$ | | | |
|-------------------------------|-----------------------|--------|-------------|--------|------------|--------|-------------|--------|------------|--------|-------------|--------|
| | $Pr = 1$ | | $Pr = 0.72$ | | $Pr = 1$ | | $Pr = 0.72$ | | $Pr = 1$ | | $Pr = 0.72$ | |
| | $\frac{T_w}{T_c} = 1$ | 10 | 1 | 10 | 1 | 10 | 1 | 10 | 1 | 10 | 1 | 10 |
| $\frac{T'}{T_c}$ (Talbot) | 1 | 5.626 | 1 | 6.086 | 5.26 | 9.886 | 2.94 | 8.020 | 18.040 | 22.667 | 8.73 | 13.817 |
| $\frac{T'/T_c}{T^*/T_c}$ | 1 | 1.0229 | 1 | 1.1065 | 0.9741 | 9.986 | 0.6216 | 0.8686 | 0.9699 | 0.9813 | 0.5476 | 0.6759 |
| $\frac{T^*}{T_c}$ (Cheng) | 0.667 | 5.167 | 0.667 | 5.167 | 4.007 | 8.507 | 4.007 | 8.507 | 14.027 | 18.527 | 14.027 | 18.527 |
| $\frac{T^*/T_c}{T^*/T_c}$ | 0.667 | 0.9395 | 0.667 | 0.9395 | 0.742 | 0.8593 | 0.8471 | 0.9214 | 0.7541 | 0.8020 | 0.8799 | 0.9063 |
| $\frac{T''}{T_c}$ (Sommer) | 1 | 5.626 | 1 | 6.086 | 5.26 | 9.886 | 4.450 | 9.544 | 18.040 | 22.667 | 14.851 | 19.932 |
| $\frac{T''/T_c}{T^*/T_c}$ | 1 | 1.0229 | 1 | 1.1065 | 0.9741 | 0.9986 | 0.9408 | 1.0337 | 0.9699 | 0.9813 | 0.9316 | 0.9751 |
| $\frac{T^*}{T_c}$ (Eckert) | 1 | 5.5 | 1 | 5.5 | 5.4 | 9.9 | 4.73 | 9.233 | 18.6 | 23.1 | 15.942 | 20.442 |

The induced pressures produced on a flat plate or wedge by the phenomenon of viscous interaction has received extensive examination. For completeness, the results presented by Hayes and Probstein will be reproduced here. The subscript, 0, refers to the original inviscid value. The induced pressure on a wedge in the weak interaction region, including heat transfer, is (to second order):

$$\frac{P}{P_0} = 1 + \gamma J_1 d_0 \frac{M_\infty}{M_0} \bar{\chi}_0 + \frac{\gamma(\gamma+1)}{4} J_2 d_0^2 \frac{M_\infty^2}{M_0^2} \bar{\chi}_0^2 \quad 2.1$$

where,

$$\bar{\chi}_0 = M_0^3 \sqrt{C} / \sqrt{Re}$$

$$d_0 = \frac{A}{M_0^2} \frac{T_w}{T_0} + (\gamma-1) B \equiv \frac{\gamma-1}{2} A \frac{T_w}{T_t} + (\gamma-1) B \quad 2.2$$

$$J_1 = \left\{ 1 + \gamma K_b^2 \left[\sqrt{\left(\frac{\gamma+1}{4}\right)^2 + \frac{1}{K_b^2}} + \frac{\gamma+1}{4} \right] \right\}^{-1} \quad 2.3$$

$$\left[\frac{\gamma+1}{2} K_b + \frac{1 + 2 \left(\frac{\gamma+1}{4}\right)^2 K_b^2}{\sqrt{1 + \left(\frac{\gamma+1}{4}\right)^2 K_b^2}} \right]$$

$$J_2 = \left\{ 1 + \gamma K_b^2 \left[\sqrt{\left(\frac{\gamma+1}{4}\right)^2 + \frac{1}{K_b^2}} + \frac{\gamma+1}{4} \right] \right\}^{-1} \quad 2.4$$

$$\left[1 + \frac{\frac{\gamma+1}{4} K_b \left\{ \left(\frac{\gamma+1}{4}\right)^2 K_b^2 - \frac{3}{2} \right\}}{\left\{ 1 + \left(\frac{\gamma+1}{4}\right)^2 K_b^2 \right\}^{3/2}} \right]$$

$$K_b = M_\infty \theta_b \quad 2.5$$

For the flat plate at zero angle of attack, $K_b = 0$, then $J_1 = J_2 = 1$ and Equation 2.1 reduces to:

$$\frac{P}{P_0} = 1 + G \bar{\chi}_0 + \frac{\gamma+1}{4\gamma} G^2 \bar{\chi}_0^2 \quad 2.6$$

where,

$$G = 0.166 \gamma(\gamma - 1) \left(2.605 \frac{T_w}{T_t} + 1 \right), \text{ Pr} = 1 \quad 2.7$$

The constants A and B in Equation 2.2 are given in the following table:

| Pr | A | B |
|-------|-------|-------|
| 1.0 | 0.865 | 0.166 |
| 0.725 | 0.968 | 0.145 |

For Pr = 0.725,

$$G = 0.145 \gamma(\gamma - 1) \left(3.24 \frac{T_w}{T_t} + 1 \right) \quad 2.7a$$

For a wedge with $K_b^2 \gg 1$ (say $M_\infty \theta_b > 5$), $J_1 \approx 2/\gamma K_b$, $J_2 \approx 4/\gamma(\gamma + 1) K_b^2$, and $M_\infty \theta_b \approx \sqrt{2/\gamma(\gamma - 1)}$. The functions J_1 and J_2 are plotted versus K_b in Figure 2-1.

In the region of strong interaction (to first order) and at zero angle of attack,

$$\frac{P}{P_0} = f_p \left(\frac{T_w}{T_t} \right) \bar{\chi}_0 + 0.76 \quad 2.8$$

The constant, 0.76, was derived for the case of an insulated plate, and is assumed to hold approximately for all values of T_w/T_t .

The function $\left(\frac{T_w}{T_t} \right)$ is given in the following table for Pr = 1:

| $\frac{T_w}{T_t}$ | f_p | |
|-------------------|----------------|-------|
| | $\gamma = 1.4$ | 1.67 |
| 0 | 0.149 | 0.261 |
| 0.2 | 0.232 | 0.403 |
| 0.6 | 0.377 | 0.696 |
| 1.0 | 0.514 | 0.921 |

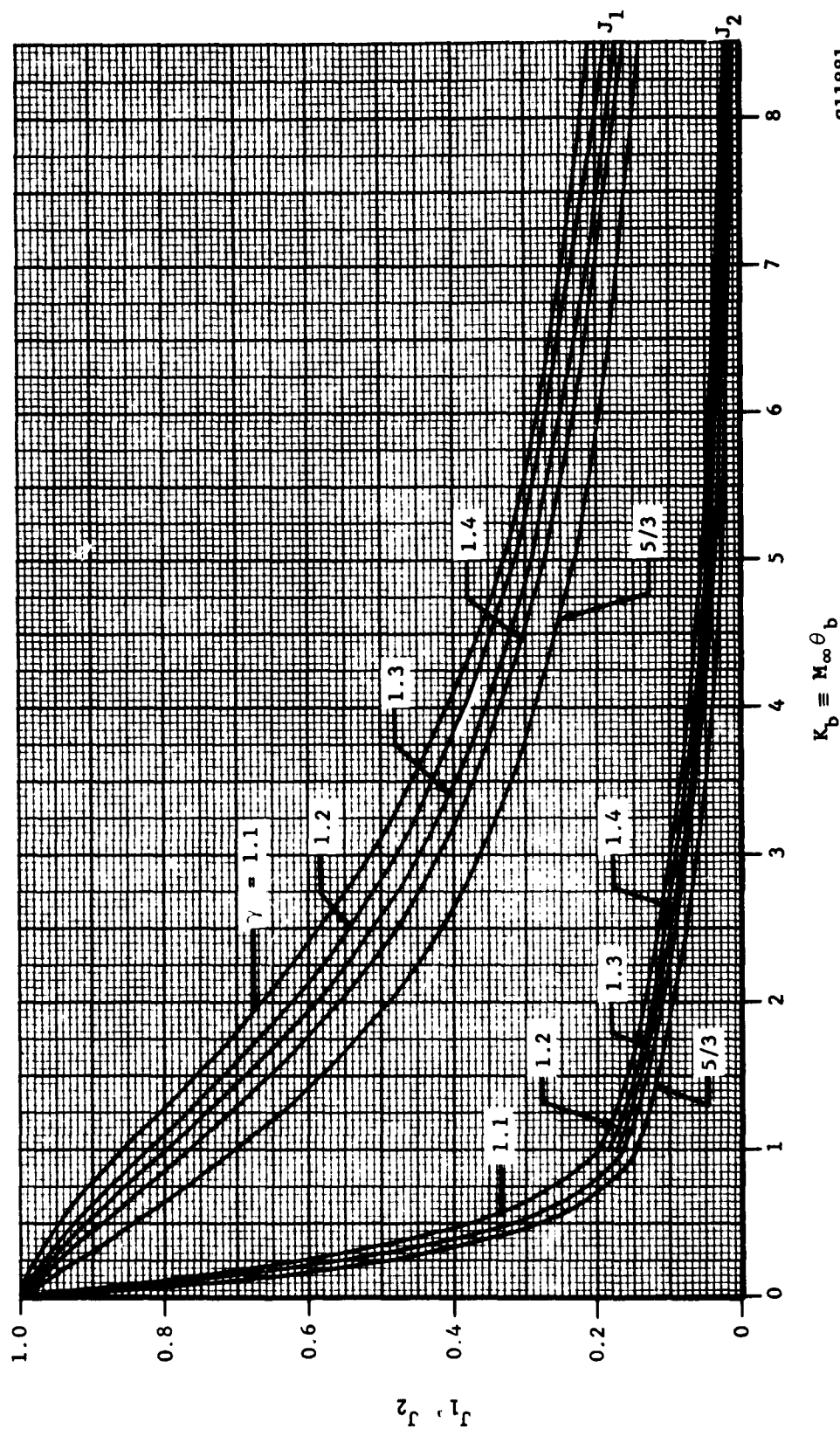


FIGURE 2-1 COEFFICIENTS J_1 & J_2 FOR INDUCED PRESSURES IN WEAK INTERACTION REGION
(SHARP FLAT PLATE)

S11881

For $Pr = 0.7$, calculations have been made⁶ which give

$$f_p\left(\frac{T_w}{T_t}\right) = \frac{3}{8} \sqrt{2} \sqrt{\gamma(\gamma+1)} (\gamma-1) I_1 \quad 2.9$$

The integral, I_1 , is presented in Figure 2-2 as a function of T_w/T_t .

The induced pressures for the two regions of interaction are presented in Figure 2-3 to various orders. The closest matching solutions is the second order weak interaction and first order strong interaction. This is given in Figure 2-4. It is noted, however, that at the largest values of $\bar{\chi}$, the effects of slip are ignored, which would reduce the induced pressures.

The viscous interaction theory for the boundary layer displacement thickness is presented in Reference 1 as

$$\left. \begin{aligned} \frac{\delta^*}{x} \sqrt{\frac{Re}{C}} \Big|_{orig} &= 1.730 \frac{T_w}{T_{orig}} + 0.664 \frac{\gamma-1}{2} M_{orig}^2, Pr = 1 \\ &= 1.937 \frac{T_w}{T_{orig}} + 0.578 \frac{\gamma-1}{2} M_{orig}^2 - 0.207, \\ &Pr = 0.725 \end{aligned} \right\} \quad 2.10$$

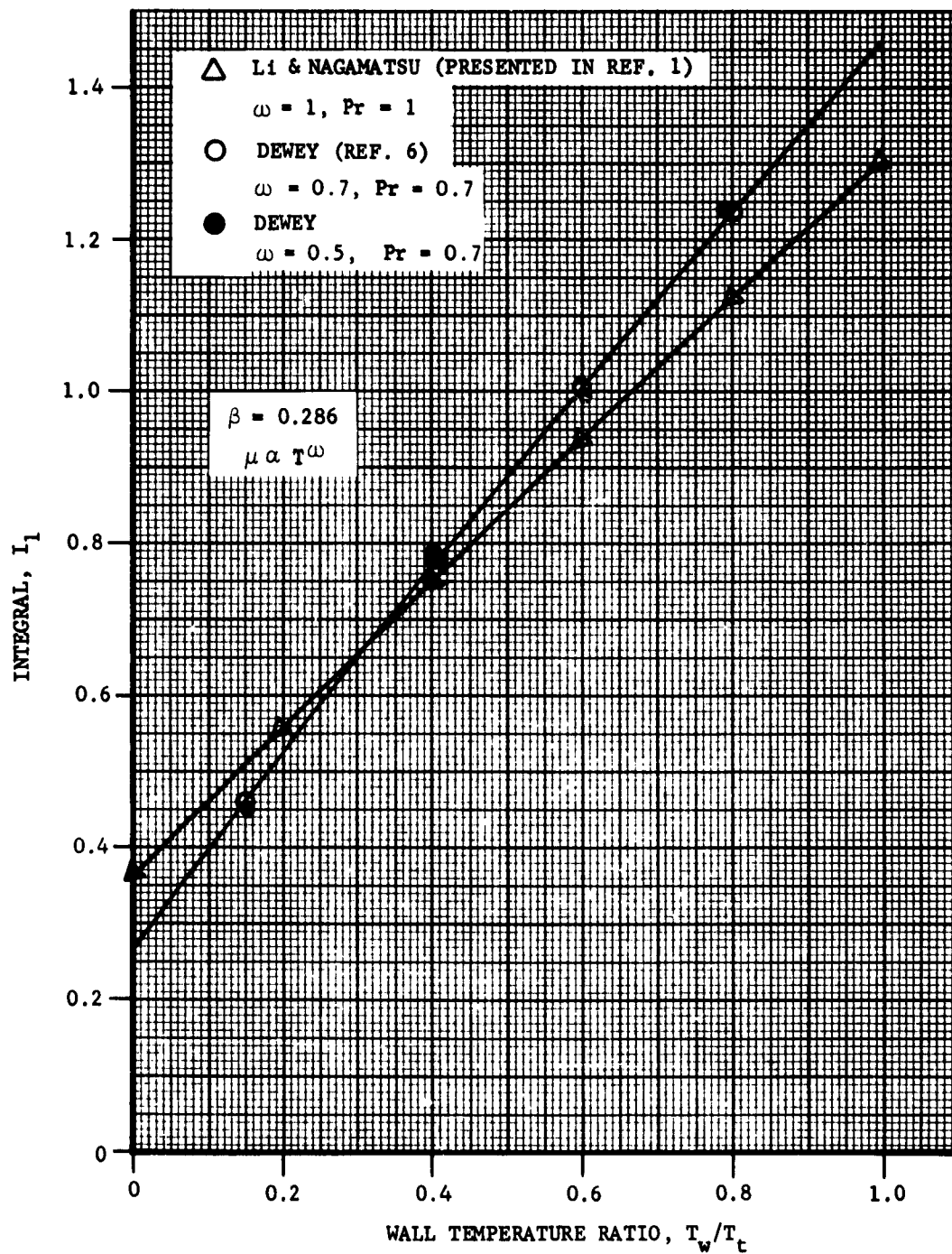
where

$$\bar{\chi} \ll 1$$

$$\frac{\delta^*}{x} = f_{\delta}(H_w/H_t) \bar{\chi}^{1/2} / M_{orig}, \quad Pr = 1; \bar{\chi} \gg 1 \quad 2.11$$

where $f_{\delta}(H_w/H_t)$ is a function of the wall temperature and is given in the following table for the zero order theory:

| $\frac{H_w}{H_t}$ | (H_w/H_t) | |
|-------------------|----------------|-----------------|
| | $\gamma = 1.4$ | $\gamma = 1.67$ |
| 0 | 0.397 | 0.457 |
| 0.2 | 0.495 | 0.568 |
| 0.6 | 0.632 | 0.726 |
| 1.0 | 0.738 | 0.858 |



S11882

FIGURE 2-2. INTEGRAL I_1 FOR SIMILAR SOLUTION

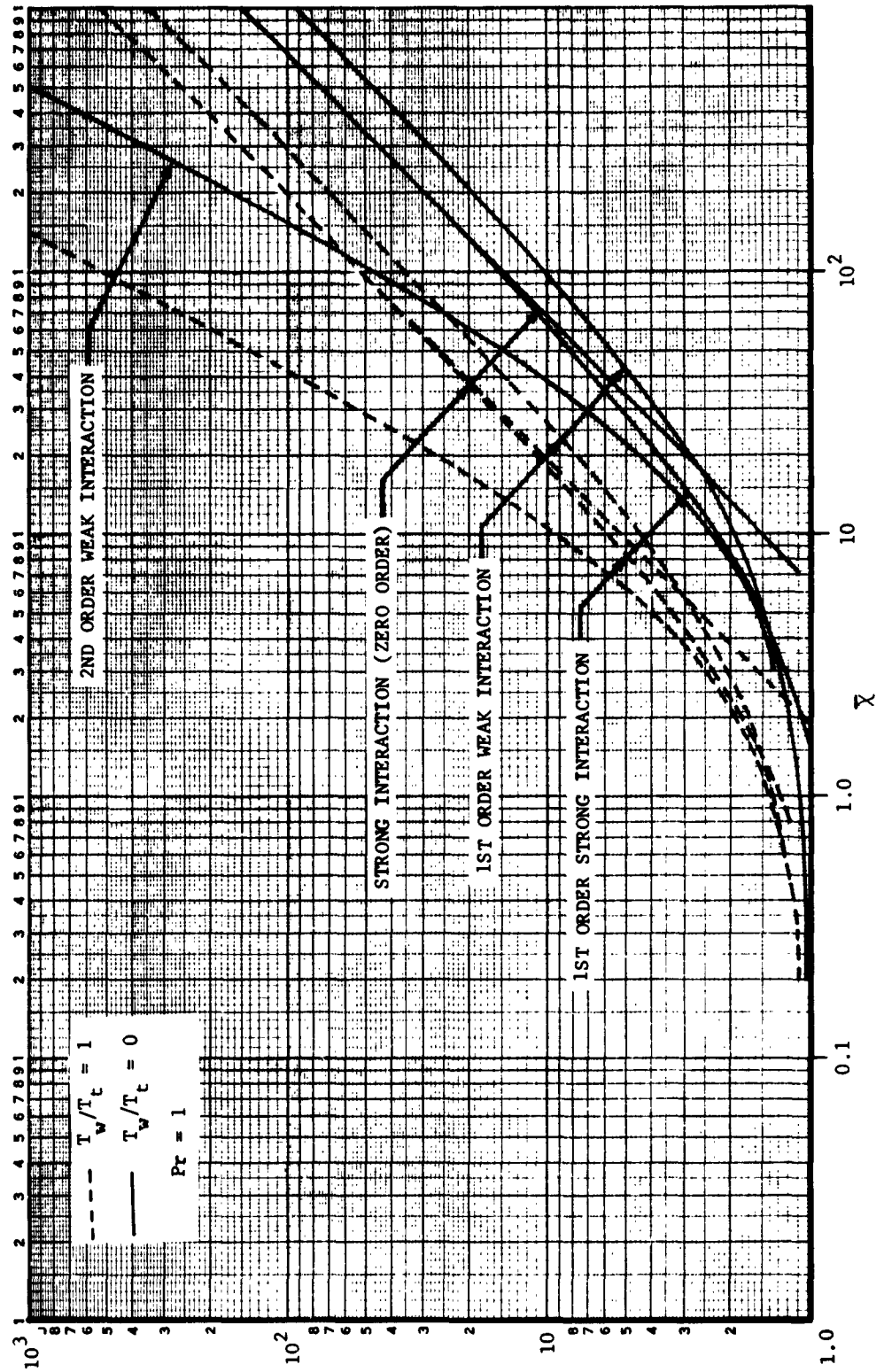


FIGURE 2-3. COMPARISON OF INTERACTION SOLUTIONS FOR INDUCED PRESSURES ON A SHARP FLAT PLATE

S11883

For $Pr = 0.7$, Reference 6 replaces Equation 2.11 for the strong interaction region

$$\frac{\delta^*}{x} = f_{\delta}(T_w/T_t) \bar{\chi}^{1/2}/M_{orig} \quad 2.12$$

where

$$f_{\delta}(T_w/T_t) = \frac{4}{3} \frac{(\gamma - 1)}{\sqrt{\gamma(\gamma + 1)}} \sqrt{2} I_1$$

Equation 2.10 is not an interaction solution in the sense that the weak induced pressures are accounted for; but it is derived from the zero pressure gradient solutions of Crocco, with a linear viscosity-temperature law and constant Prandtl number. Hayes and Probstein have shown that the induced pressure has no first-order effect on the slope of the boundary layer, but produces only a uniform reduction in thickness. This reduction can be calculated from results presented by Lees and Probstein, providing the first-order solutions (in the assumed velocity and temperature series expansions) to the energy and momentum equations are known. These solutions, as obtained by Lees and Probstein, have been utilized to estimate a correction to the boundary layer thickness, $\delta^*(0)$, as expressed by Equation 2.10. To the accuracy of the hand calculations (including several graphical integrations), the corrections for $Pr = 1$ may be expressed as follows:

$$T_w/T_e = 0 \quad (\text{highly cooled body}):$$

$$\delta^*(1) \approx \delta^*(0) (1 - 0.01 \bar{\chi}_0)$$

$$T_w/T_e = T_{Aw}/T_e \quad (\text{insulated wall}): \quad 2.13$$

$$\delta^*(1) \approx \delta^*(0) (1 - 0.10 \bar{\chi}_0)$$

For the weak interaction assumptions ($\bar{\chi}_0 < 1$), it is seen that the correction amounts to less than one percent at $T_w/T_e = 0$, and less than ten percent for the insulated plate case.

The displacement thickness is presented, rather than the boundary layer thickness; but, in hypersonic flow where the densities in the boundary layer are very low, δ and δ^* may be taken to be approximately equal. This is a considerable increase in δ^* over the incompressible flow case where $\delta^* \approx \delta/3$. An estimate of the deviation of δ^*/δ from a value of one may be made as a function of M_e and T_w/T_e . For a perfect gas and constant pressure across the boundary layer, the results of the Crocco integral give the density distribution in the boundary layer as:

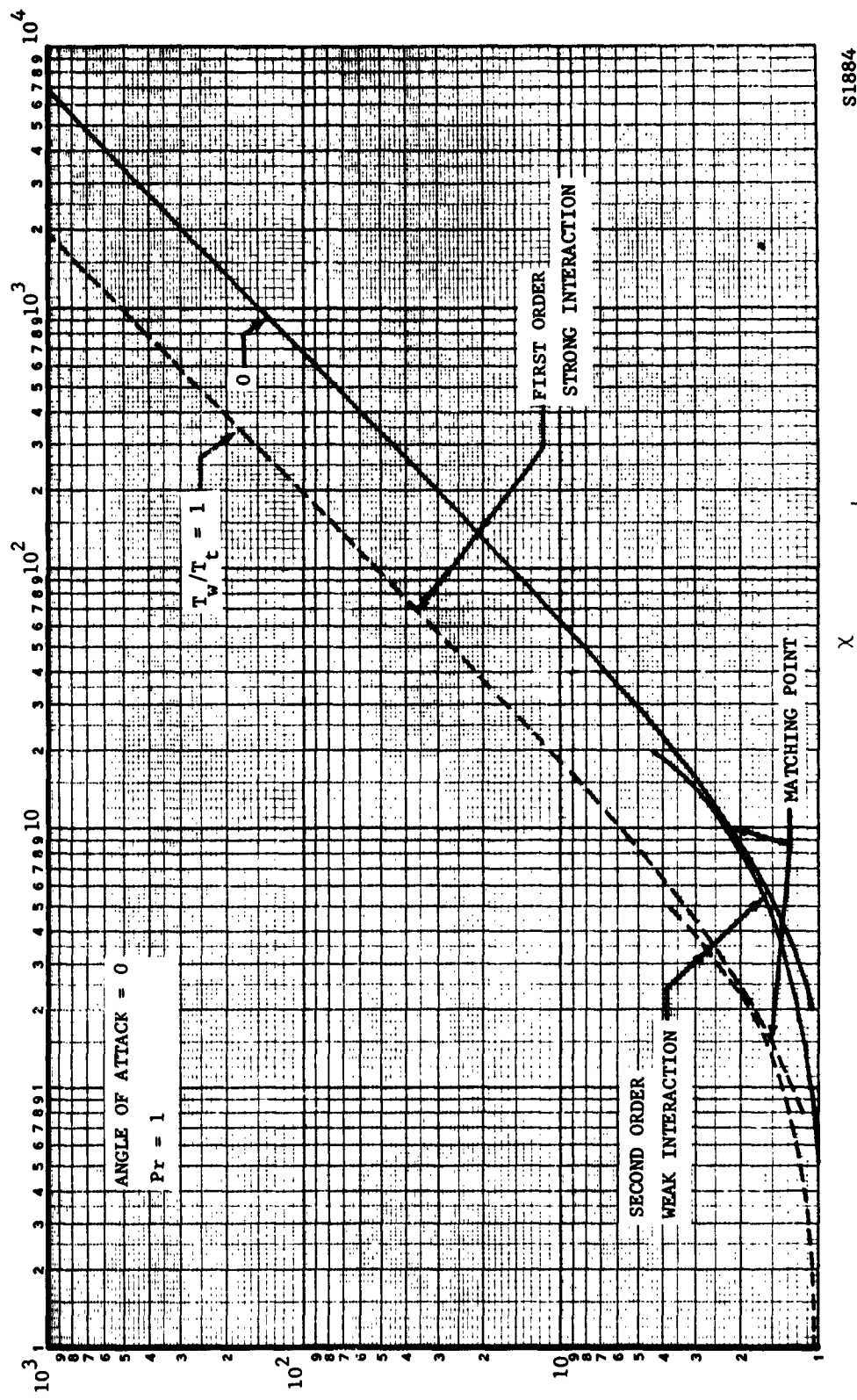


FIGURE 2-4. INDUCED PRESSURES ON A SHARP FLAT PLATE DUE TO VISCOUS INTERACTION

S1884

$$\frac{\rho_e}{\rho} = \frac{T_w}{T_e} + \left(\frac{T_{Aw}}{T_e} - \frac{T_w}{T_e} \right) \frac{u}{u_e} - \left(\frac{T_{Aw}}{T_e} - 1 \right) \left(\frac{u}{u_e} \right)^2 \quad 2.14$$

From the definition of displacement thickness,

$$\delta^* = \int_0^\delta \left[1 - \frac{\rho u}{(\rho u)_e} \right] dy \quad 2.15$$

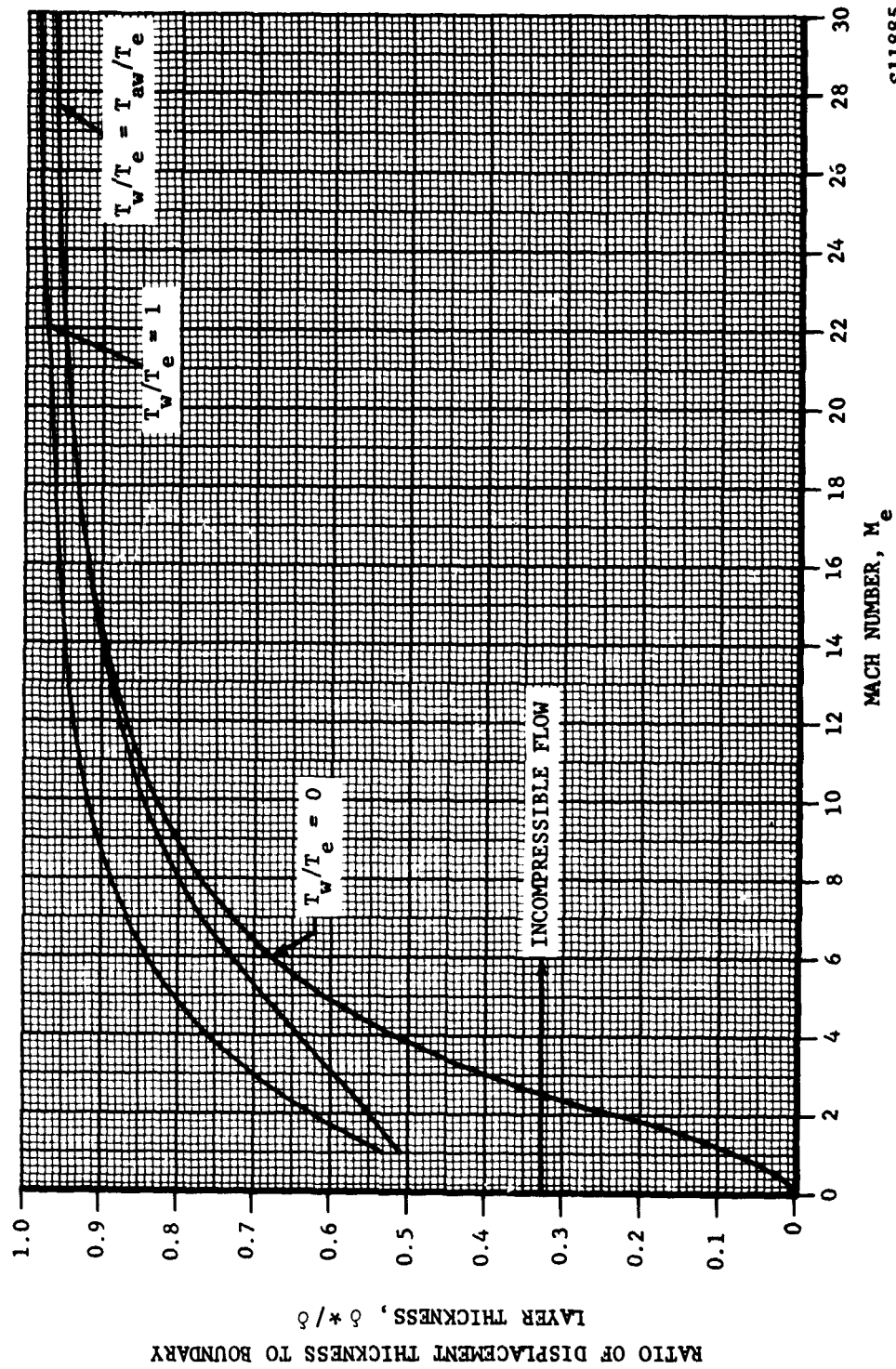
Then, for $T_{Aw}/T_e \gg 1$ (local hypersonic flow),

$$\frac{\delta^*}{\delta} \approx \frac{1}{\delta} \int_0^\delta \left[1 - \frac{u/u_e}{\frac{T_w}{T_e} + \left(\frac{T_{Aw}}{T_e} - \frac{T_w}{T_e} \right) \frac{u}{u_e} - \frac{T_{Aw}}{T_e} \frac{u^2}{u_e^2}} \right] dy \approx 1 \quad 2.16$$

The variation of δ^*/δ with local Mach number for a linear velocity profile and various values of T_w/T_e is given in Figure 2-5. This implies that in the very strong interaction regime where the local Mach number may drop considerably, due to the highly curved and very thick boundary layer, the assumption of $\delta^*/\delta \approx 1$ could be in appreciable error. The hypersonic flow criteria must be considered to be local hypersonic flow for $\delta^* \approx \delta$. The two thickness will be used interchangeably in the remainder of this report.

Various procedures have been devised to provide a smooth transition from the weak to strong interaction region. Approximate solutions, such as integral and inverse methods, can be constructed which inherently include a continuous transition. The solutions given by Equations 2.10 to 2.12 consider the limiting regimes of weak and strong interactions. A simple transition can be achieved by matching the individual solutions at their common intersection or point of closest approach. This has been done by Bertram.⁵ His results are as follows:

| T_w/T_{Aw} | $\bar{\chi}_0$ | |
|--------------|----------------|------|
| | 1.4 | 1.67 |
| 0 | 10.17 | 5.36 |
| 0.2 | 5.65 | 2.83 |
| 0.6 | 2.60 | 1.22 |
| 1.0 | 1.46 | 0.66 |
| 2.0 | 0.56 | 0.24 |



S11885

FIGURE 2-5. RATIO OF DISPLACEMENT TO BOUNDARY LAYER THICKNESS IN HYPERSONIC FLOW

2.3 SHARP CONE

For the case of a flat plate, a number of noniterative interaction solutions exist both for the weak and strong interaction regimes. For the case of a cone, however, only the weak interaction solution is presently available. It might be supposed that this would lead to some difficulty at the lower Reynolds numbers, since under these conditions hypersonic theory would predict a flow field of the strong interaction type. However, it will be shown later that at these lower Reynolds numbers, other effects such as slip flow already predominate to a degree that interaction theory alone is no longer valid.

The conical flow weak interaction theory to be reviewed here is that due to Lees and Probstein and subsequently amplified in Reference 4. Probstein's approach is based on an asymptotic series expansion of the boundary layer flow quantities in terms of ascending powers of the hypersonic interaction parameter χ . The zero order equations and boundary conditions for this series, (after applying the Mangler transformation), are identical to the flat plate case, and each higher order equation is expressible in terms of coefficients which are functions only of lower-order solutions in the expansion.

From these equations, a first-order solution to the interaction effects on the cone drag are obtained using the assumptions of Prandtl number unity and a perfect gas of constant specific heat.

According to Probstein's theory, the interaction pressure is assumed to be a unique function of the local total flow deflection (θ) and may be expressed as a Taylor series expansion in powers of $d\delta^*/dx$.

For both the wedge and the cone, the expansion is in the following form:

$$\frac{P}{P_c} = 1 + \frac{1}{P_c/P_\infty} \left(\frac{d(P/P_\infty)}{d\theta} \right)_{\theta=\theta_b} \left(\frac{d\delta^*}{dx} \right) + \frac{1}{2 P_c/P_\infty} \left(\frac{d^2 P/P_\infty}{d\theta^2} \right)_{\theta=\theta_b} \left(\frac{d\delta^*}{dx} \right)^2 + \dots \quad 2.17$$

where θ_b is the equivalent body angle and the subscript c refers to the original conditions associated with uniform inviscid conical flow (Taylor - Maccoll values).

While the coefficients of $d\delta^*/dx$ can always be evaluated numerically from the Taylor - Maccoll theory it is inconvenient from the point

of view of obtaining an analytic interaction theory. Lees,¹² using hyper-sonic similarity theory, has obtained an algebraic relation for the inviscid surface pressure on an unyawed cone that is quite accurate within the limitations that $K = M_\infty \theta_c \geq 1$ and $\theta_c < 24^\circ$. This relation is

$$\frac{P_c}{P_\infty} = \frac{2\gamma}{\gamma + 1} (K_s^2 - 1) + \gamma (K_s - K)^2 \left[\frac{\gamma + 1}{\gamma - 1 + 2/K_s^2} \right] + 1 \quad 2.18$$

where $K_s = M_\infty \theta_s$, θ_s is the shock angle, and θ_c is the cone angle. The relationship between K_s and K is given by:

$$K_s = \frac{\gamma + 1}{\gamma + 3} K + \sqrt{\left(\frac{\gamma + 1}{\gamma + 3} \right)^2 K^2 + \frac{2}{\gamma + 3}} \quad 2.19$$

The results given for the wedge were based on a solution for the coefficients, $d(P/P_\infty)/d\theta$, $d^2(P/P_\infty)/d\theta^2$, etc., from the tangent wedge approximation. One approach for obtaining the cone pressures is to utilize the Mangler transformation,

$$d\delta^*/dx = \frac{d}{3} \frac{M^2 \sqrt{C}}{\sqrt{Re_c}} \quad 2.20$$

and apply this to the equations given for the flat plate. An alternate procedure is to evaluate the coefficients, $d(P/P_\infty)/d\theta$, etc., from the tangent cone approximation and provide a solution directly applicable to the cone. This has been done for $K \geq 1$ so that the first coefficient of $d\delta^*/dx$ in Equation 2.17 is:

$$\left[\frac{d(P/P_\infty)}{d\theta} \right]_{\theta=\theta_b} = \frac{2\gamma M_\infty}{\gamma+3} \left\{ 2 K_s \left[1 + \frac{K}{\frac{\gamma+3}{\gamma+1} K_s - K} \right] \right. \\ \left. + \frac{(\gamma+1)(K_s - K)}{\gamma - 1 + \frac{2}{K_s^2}} \left[\frac{K - \frac{2}{\gamma+1} K_s}{\frac{K_s}{\gamma+1} - \frac{K}{\gamma+3}} \right] \right. \\ \left. + \frac{2(\gamma+1)^2(K_s - K)^2}{K_s^3 \left\{ \gamma - 1 + \frac{2}{K_s^2} \right\}^2} \left[1 + \frac{K}{\frac{\gamma+3}{\gamma+1} K_s - K} \right] \right\} \quad 2.21$$

and a considerably longer term for the coefficient of the second-order term.

At this point, an analytic iteration procedure is begun by taking

$$\frac{d\delta^*}{dx}$$

equal to the value given by the zero pressure gradient boundary layer solution for the flow over a cone. This is equivalent to using the flat plate solution with the application of the Mangler transformation as the zero order approximation to

$$\frac{d\delta^*}{dx}$$

It is well known that the Mangler transformation is applicable only when the boundary thickness is small compared to the body radius. Since this restriction is violated near the tip of the cone, even in absence of interaction effects, the validity of the Mangler transformation under these conditions must be re-examined in the future.

Following Lees and Probstein, Equations 2.17 to 2.21 may be used to give,

$$\frac{P}{P_c} = 1 + F_c \bar{\chi}_c + O(\bar{\chi}_0^2) \quad 2.22$$

where,

$$F_c = \frac{d_c}{\sqrt{3}} \frac{1}{M_c} \frac{P_\infty}{P_c} \left[\frac{d(P/P_\infty)}{d\theta} \right]_{\theta = \theta_c} \quad 2.23$$

The subscript, 0, previously used, has been changed here to c. The value, d, is still given by 2.2. The value, F_c , is plotted in Figure 2-6 as a coefficient, $F_c M_c / \gamma d_c M_\infty$, versus K. The coefficient, $J_1 / \sqrt{3}$, is also presented for comparison.

A comparison of the theoretical methods is presented in Figure 2-7. The ratio, $\frac{M_\infty}{M_c}$, has been evaluated from the compressible flow equations as:

$$\frac{M_\infty^2}{M_c^2} = \frac{[2 \gamma K_s^2 - (\gamma - 1)] [(\gamma - 1) K_s^2 + 2]}{[(\gamma + 1)^2 K_s^2 - 4 \frac{(K_s^2 - 1)}{M_\infty^2} (\gamma K_s^2 + 1)]} \quad 2.24$$

Since a strong interaction solution is not available (other than modifying the results for the wedge by the Mangler transformation), the liberty has been taken to extend the first-order weak interaction solution to large values of $\bar{\chi}_c$. By analogy to the case of the wedge, it is expected that the first-order weak interaction solution follows the strong interaction solution with a reasonably constant numerical difference of percentage, since both solutions are linear in $\bar{\chi}$. Assuming that the cone solution is correct, the errors in the flat plate solution with Mangler's transformation (for the weak interaction case) are as follows:

| $\bar{\chi}_c$ | $K_c = 1$ | $K_c = 4$ | $K_c = 8$ |
|----------------|-----------|-----------|-----------|
| 1 | -0.3% | -0.0% | +0.1% |
| 10 | -3.1% | -0.3% | +2.3% |
| 10^2 | -7.9% | -0.5% | +7.3% |
| 10^3 | -9.7% | -0.8% | +9.7% |

The strong interaction solution superimposed on Figure 2-8 (by applying Mangler's transformation to the flat plate, i.e., P/P_c varying linearly with $\bar{\chi}_c / \sqrt{3}$), is higher than the cone solution, except for $K < 1$. The effects of slip at large $\bar{\chi}$ values have been ignored also, which would tend to reduce the induced pressures at the larger values of $\bar{\chi}$.

Accordingly, the solution as given by Equation 2.22 will be assumed valid over the whole range of $\bar{\chi}_c$.

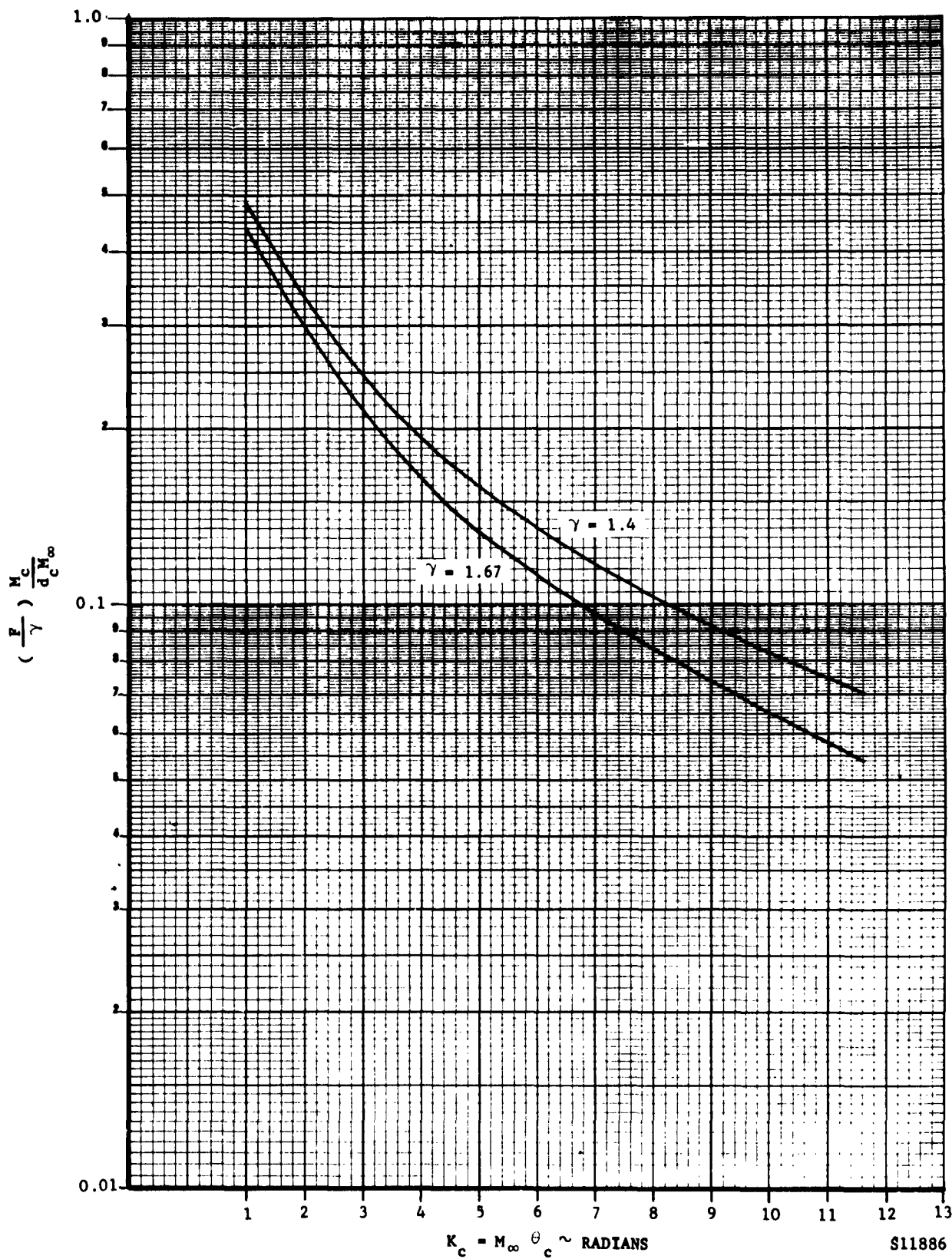


FIGURE 2-6. THE FUNCTION F FOR $\gamma = 1.4$ AND 1.67

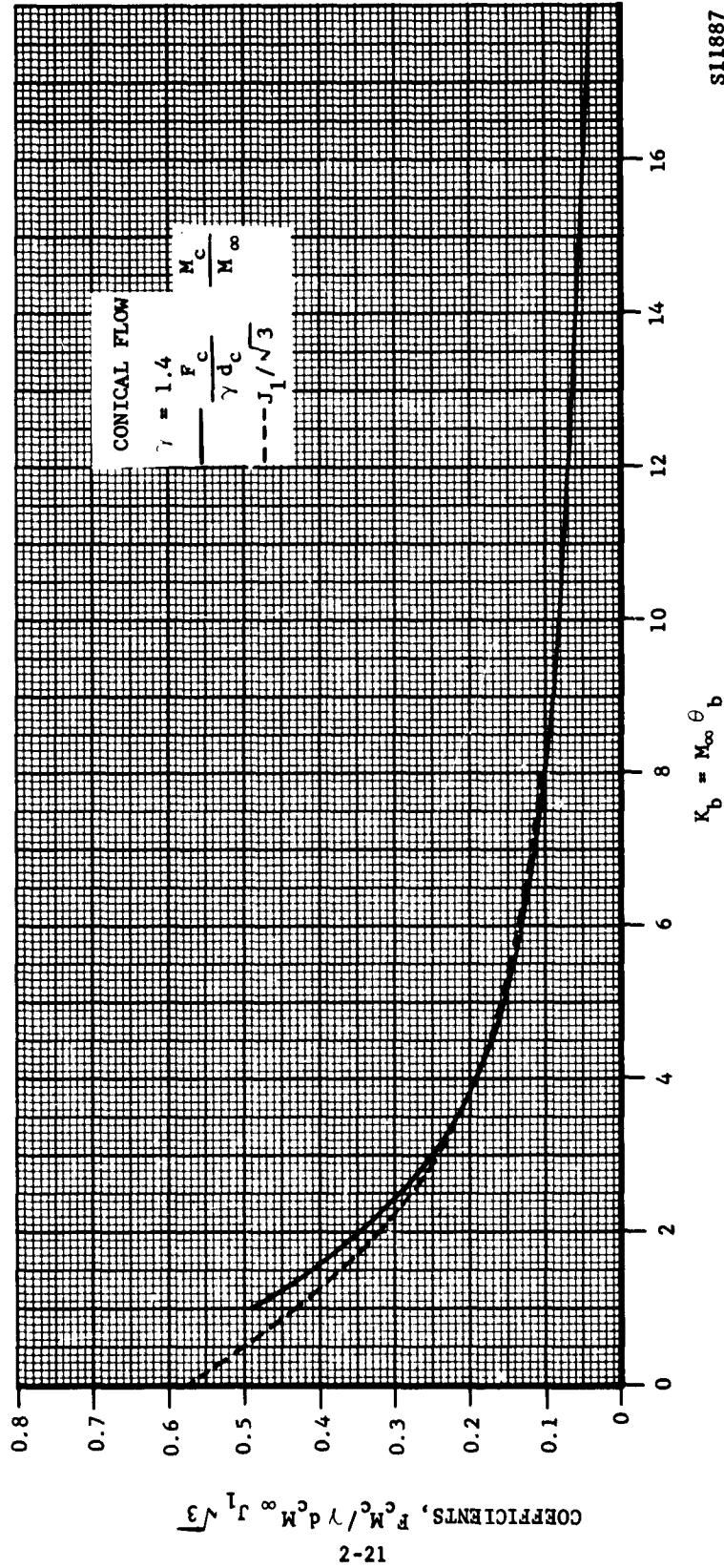


FIGURE 2-7. COEFFICIENTS $(F_c/\gamma d_c (M_c/M_\infty))$ & $J_1/\sqrt{3}$ FOR INDUCED PRESSURES IN WEAK INTERACTION REGION

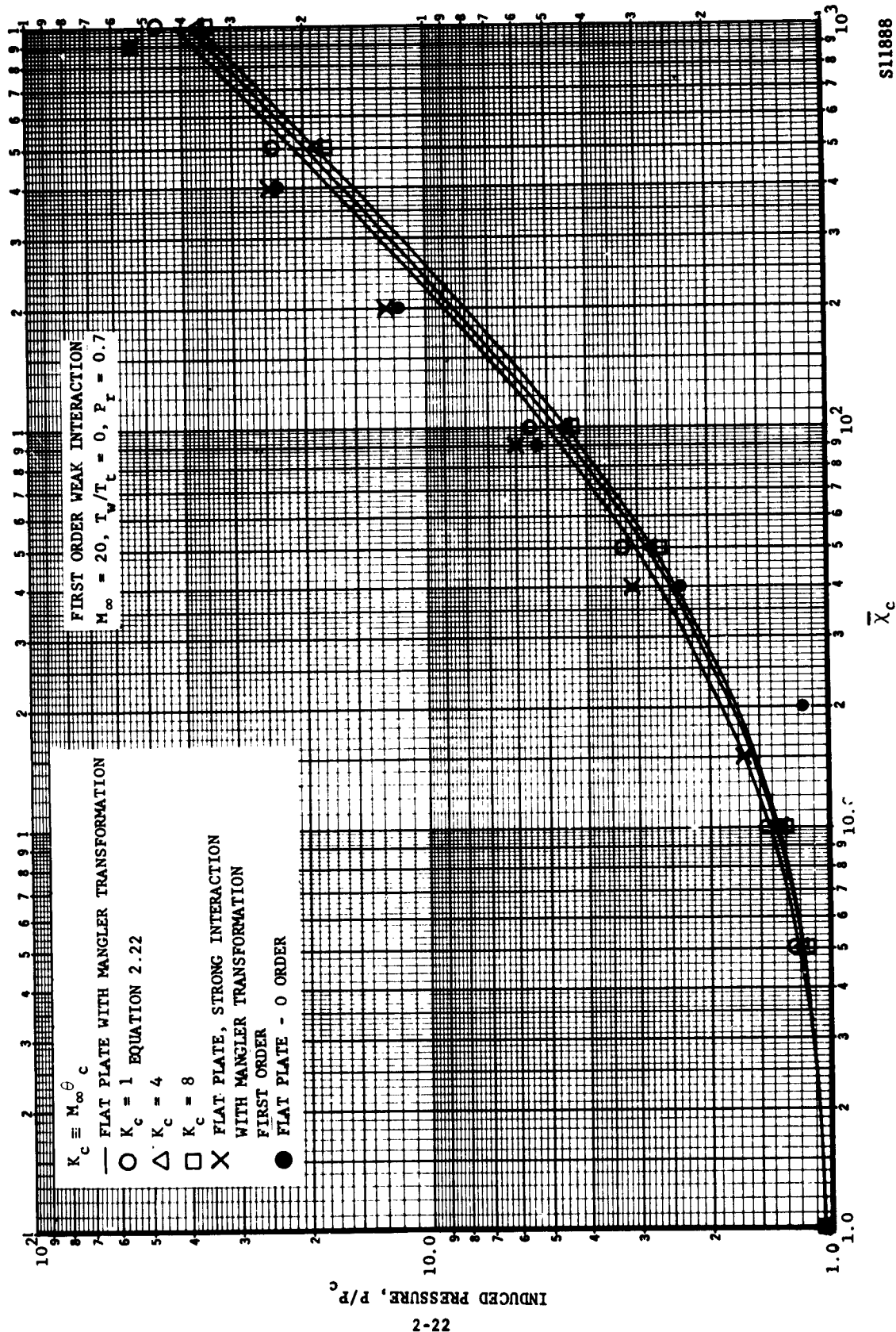


FIGURE 2-8. COMPARISON OF INDUCED PRESSURES ON A CONE

CHAPTER 3

BOUNDARY LAYER GROWTH AND SHOCK SHAPE ON SHARP CONES AT ZERO ANGLE OF ATTACK

3.1 COMPARISON OF ANALYTICAL METHODS FOR BOUNDARY LAYER GROWTH

Before proceeding to the cone, the case of the sharp flat plate will be examined. The methods to be compared for calculating the laminar boundary layer are twofold in number:

1. Compressible laminar boundary layer theory, and
2. Viscous interaction theory.

Both have been extensively examined. Van Driest has numerically solved the laminar boundary layer equations using the Crocco variables. This solution is also applicable to the case of a wedge, if the independent parameters are interpreted in terms of the local values at the edge of the boundary layer.

The interaction solution should give better results than that of the compressible laminar boundary layer theory since it includes the effect of the pressure gradient and pressure level with the interaction solution (within the limits already discussed for $\bar{x}_0 < 1$). Intuitively, the compressible laminar boundary layer theory could be used to generate answers identical to the interaction solution by considering the classical concept of the displacement thickness. This gives a new equivalent body from which to calculate a new shock wave and resultant property changes across the shock. An interaction procedure can be devised to match the boundary layer growth (as a function of local flow properties) to the change in flow properties across the shock wave. The interaction theory offers the advantage of being able to obtain the boundary layer thickness from the original inviscid flow values without any iteration procedure

being needed. When the boundary layer thickness is still relatively small, however, the required iterations will also be small, since the shock displacement is small. The principle deviation of the results of item 1 from item 2 of Section 3.1, would then be expected to be the increase in local Reynolds number due to the induced pressures and any pressure gradient effects (Reference 5). The boundary layer thickness may then be obtained approximately from Reference 7 by replacing Re with $Re \sqrt{P/P_0}$, where P/P_0 is the induced pressure caused by viscous interaction.

A case of practical interest for comparing methods is a hypersonic re-entry condition; accordingly, a comparison of these methods for estimating the boundary layer growth is given in Figure 3-1 at $M_\infty = 20$. In this and all subsequent altitude calculations, the 1959 ARDC standard atmosphere is used. It is seen that the agreement between the interaction theory and the results of Van Driest with a pressure correction is very good. The difference between the two solutions in the weak interaction region is due to the use of different viscosity temperature relationships. The effect of Prandtl number is also noted in Figure 3-1. Reference 6 presents solutions for a continuous variation of boundary layer thickness, pressure, skin friction, and heat transfer from the weak interaction region to the strong interaction region. The broken line of Figure 3-1 represents the limiting case of strong interaction as obtained from Reference 6.

Figure 3-1 indicates that the effect of the pressure gradient on boundary layer growth is small since the Van Driest solution is for zero pressure gradient, and the strong interaction solution is based on a value of the pressure gradient parameter, $\beta = 0.286$. This observation has been previously noticed for a highly cooled body¹³, when the gas near the body surface is much cooler and more dense than that in the rest of the boundary layer. The streamwise pressure gradients are then not very effective in perturbing the velocity and enthalpy profiles from the no pressure gradient case. The conventional compressible laminar boundary layer solution should then be adequate, taking into account only local pressure effects on local Reynolds number; and in agreement with previously stated expectations. The close agreement at the high altitudes where the boundary layer becomes very thick also indicates that the range of application of the boundary layer equations, which were derived for a thin boundary layer, is much wider than usually supposed. The close agreement must otherwise be held to be fortuitous or else a cancellation of the various effects must occur.

The study of the flat plate provides a foundation for studying more general bodies, such as the sharp cone. The general conclusions regarding the interacting laminar boundary layer on the flat plate are also expected to apply to the case of the cone. The actual use of flat plate

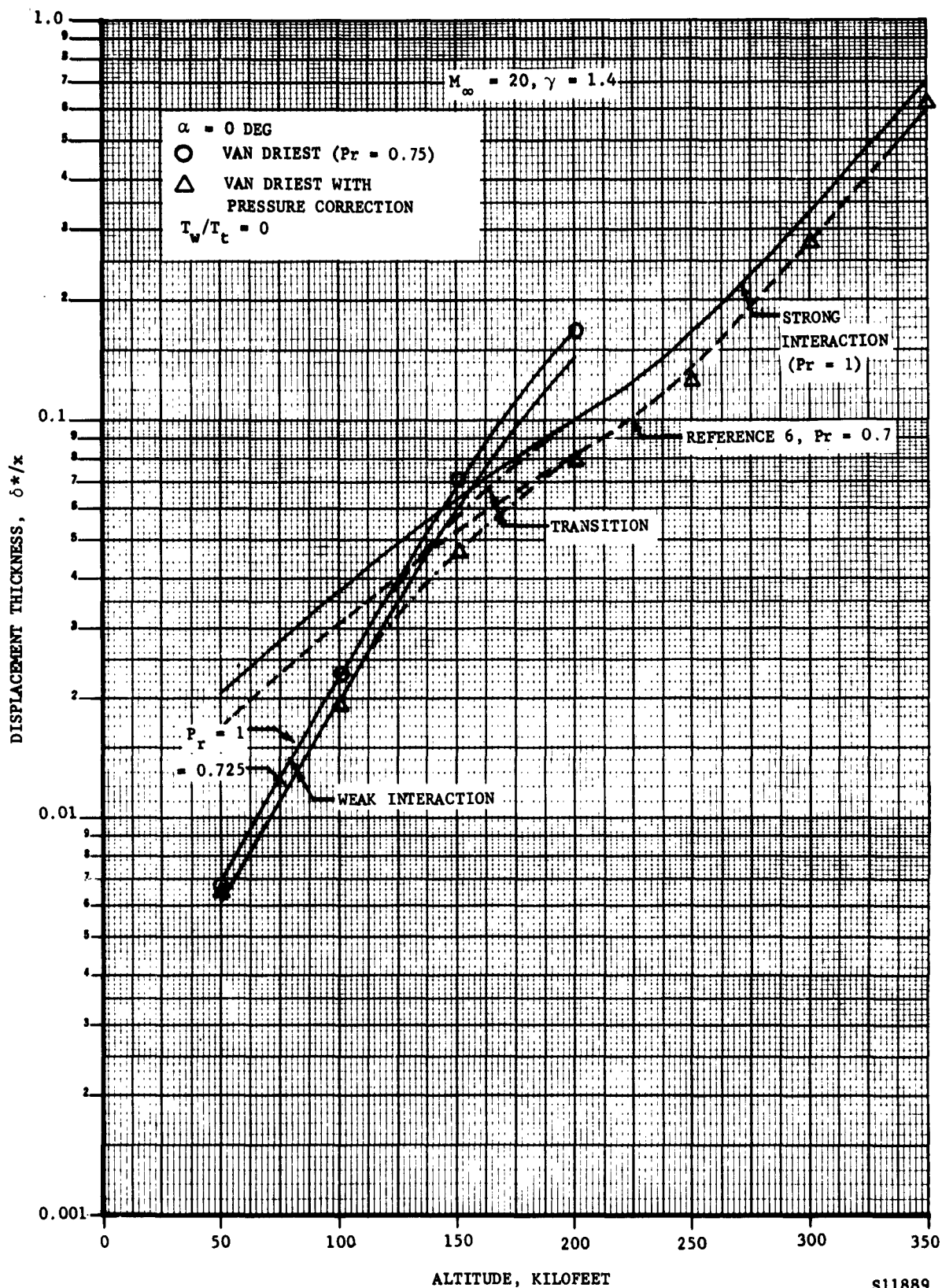


FIGURE 3-1. DISPLACEMENT THICKNESS ON A SHARP FLAT PLATE

Ford Motor Company,
AERONAUTRONIC DIVISION

calculations modified by a constant such as obtained from Mangler's transformation must be made with caution. The Mangler transformation is one that reduces the boundary layer equation for axisymmetric flow to those for two-dimensional flow. An example is the conversion of the integral momentum boundary layer equation over a cone, to that of the flow over a wedge. If the coordinate system for both the two-dimensional and axisymmetric cases is taken so that the direction of one dimension is parallel to the surface of the body (e.g., along the generator of a cone), and the other perpendicular to the surface, then the forms of the momentum and energy equations for the axisymmetric flow are identical to those for the two-dimensional case. Therefore, the Mangler transformation must be able to change the form of the continuity equation from the axisymmetric to the two-dimensional form without affecting the form of either the momentum or energy equation. This has previously been demonstrated¹⁴.

The transformation equations are:

$$\bar{x} = \frac{1}{L^2} \int_0^x r^2 dx \quad 3.1$$

$$\bar{y} = \frac{r}{L} y \quad 3.2$$

Where L = constant reference length

r = local radius of revolution

The barred variables refer to the two-dimensional flow case and the unbarred variables refer to the axisymmetric case. The boundary layer growth over a flat plate in compressible laminar flow without viscous interaction is given by,

$$\delta \propto \frac{\bar{x}}{\sqrt{\frac{\rho v_{\infty} \bar{x}}{\mu}}} \int_0^{\delta} \left(1 - \frac{\rho u}{\rho_e u_e}\right) d\bar{y} \quad 3.3$$

For a cone, Equation 3.1 gives,

$$\bar{x} = r^2 x / 3L^2 \quad 3.4$$

If 3.2 and 3.4 are substituted in 3.3,

$$\delta \propto \frac{x}{\sqrt{3} \sqrt{\frac{\rho v_{\infty} x}{\mu}}} \alpha \int_0^{\delta} \left(1 - \frac{\rho u}{\rho_e u_e} \right) dy \quad 3.5$$

Equation 3.5 is identical in form to 3.3 with all barred variables eliminated. Equation 3.5 means that the flat plate equation may be applied to the case of the cone, providing the same local properties are used and the results are multiplied by a factor $1/\sqrt{3}$.

The boundary layer equations assume a priori, however, that the boundary layer thickness is thin. This means that the Mangler transformation (in the sense of correcting flat plate results by a constant) is not valid in the case of a thick boundary layer, since the additional terms (in the boundary layer equations) required to describe the flow will not allow the form of the axisymmetric equations to be reduced to those of the form of the two-dimensional flow. In more general terms, the purpose of the Mangler transformation is to transform one set of differential equations to another set for which solutions are known, which is true of any transformation. It is thus seen that Mangler's transformation would not invalidate equations of motion for a thick boundary layer, but rather that a different set of differential equations must be solved.

If the effects of viscous interaction are considered, it is concluded that Mangler's transformation gives results identical to equation 3.5 for the case of weak interaction, since $\delta \propto x^{1/2}$ and is still relatively thin. In the strong interaction region, however $\delta \propto x^{3/4}$, and the use of Equations 3.1 and 3.2 does not reduce the expression for δ to a form identical to Equation 3.3. This is expected, since the strong interaction region is associated with a thick boundary layer. It is thus apparent that in the case of an axisymmetric flow over a cone with a thick boundary layer, and, in particular, in the strong interaction region, the Mangler transformation does not reduce the form of the axisymmetric equations to the two-dimensional form. Furthermore, it can be shown that any similar

transformation of the type $\bar{x} = \frac{1}{L^n} \int r^n dx$, $n \neq 2$, does not transform

the axisymmetric continuity equation into two-dimensional form (e.g., Reference 14). It remains to be shown, however, what the error is in assuming a correction factor of the type, $1/\sqrt{3}$, to the flat plate calculation of the boundary layer thickness in the strong interaction region.

In order to gain insight as to what an appropriate engineering method would be for computing the thick boundary layer on a cone, three different methods will now be examined and compared. These methods are

1. Extrapolation of solution derived for thin boundary layer to the case of thick boundary layer (e.g., Reference 7 with Mangler's transformation, or Reference 15 at $\alpha = 0$).
2. Viscous interaction theory (Equations 2.10 - 2.12) corrected by factor, $3 Re_c - Re_{FP}$.
3. Solution of boundary layer equations including terms of transverse curvature (Reference 16).

Solution 1:

The flat plate results of Van Driest may be used by replacing $\frac{\delta}{x} \sqrt{Re}$ by $\frac{\delta}{x} \sqrt{3 Re}$ and integrating to find the local properties. As in the case of the flat plate, an approximation may be made to eliminate the required iteration procedure by taking $\frac{\delta}{x} \sqrt{Re}$ as $\frac{\delta}{x} \sqrt{3 Re P/P_c}$, and taking the local flow properties as the original inviscid values, assuming that an independent determination of the induced pressures can be made. Interaction theory for the induced pressures with the Mangler transformation or the first-order weak interaction on a cone should be applicable since the transverse curvature effect has only a weak effect on the induced pressures (p. 364, Reference 1). An alternate solution is given in Reference 15, where the results at $\alpha = 0$ may be used. These results for the compressible laminar boundary layer growth over a cone are similar to those of Van Driest except that Mangler's transformation was utilized in the derivation, and a linear viscosity-temperature relationship was used. The boundary layer thickness may be presented as :

$$\frac{\delta}{x} \sqrt{\frac{3 Re}{C}} = \int_0^\lambda \left[1 + \frac{\gamma-1}{2} M_e^2 \left(1 - \frac{u^2}{u_e^2} \right) + \left(\frac{T_w}{T_c} - 1 \right) \left(1 + \frac{\gamma-1}{2} M_e^2 \right) \left(1 - \frac{u}{u_e} \right) \right] d\lambda \quad 3.6$$

The right hand side of Equation 3.6 integrates to the identical value of the right side of Equation 2.10, with T_{orig} replaced by the local value T_e . This result is to be expected since the assumptions are the same for both derivations. These involve the flow being described by the Blasius equation, with the Mangler transformation utilized in the case of the cone. This solution also represents the zero order term for the case where transverse curvature is included, and will be examined further under Solution 3.

The problem of what procedure to follow in the iterated solution will be examined under Solution 3. The procedure for Solution 1, however, is arbitrarily taken as the tangent cone method using NACA Report Number 1135 to obtain the shock angle (or local shock slope).

Solution 2:

For the viscous interaction solution, modification of Equations 2.10-2.12 gives ($Pr = 1$):

a) Weak Interaction

$$\frac{\delta^*}{x} \sqrt{\frac{3Re}{C}} = 1.730 \frac{T_w}{T_c} + 0.664 \frac{\gamma-1}{2} M_c^2 \quad 3.7$$

which is identical to Equation 3.6.

b) Strong Interaction

$$\frac{\delta^*}{x} = f_{\delta} (H_w/H_t) \bar{x}^{1/2} / 3^{1/4} M_c \quad 3.8$$

Solution 3:

This solution is taken to be the reference solution, since it contains all the aspects of the actual three-dimensional flow, within the applicability of the boundary layer approximations. The nature of the problem is such, however, that an iterative procedure must again be devised to match the boundary layer growth with the inviscid flow properties occurring across the actual shock wave. The examination of the compressible laminar boundary layer then gives a solution applicable throughout all regions of viscous interaction (i.e., weak and strong), including a smooth transition

between the two regions, and accounting for the axially symmetric boundary layer growing not only in thickness with distance along the surface, but also spreading circumferentially as it grows. The applicable axially symmetric boundary layer equations are¹⁶:

Continuity,

$$\frac{\partial(\rho u r)}{\partial x} + \frac{\partial(\rho v r)}{\partial y} = 0 \quad 3.9$$

Momentum,

$$\rho u \frac{\partial u}{\partial x} + \rho v \frac{\partial u}{\partial y} = - \frac{dP}{dx} + \frac{\partial}{\partial y} \left(\mu \frac{\partial u}{\partial y} \right) + \frac{\mu}{r} \frac{\partial r}{\partial y} \frac{\partial u}{\partial y} \quad 3.10$$

Energy,

$$\rho u \frac{\partial h}{\partial x} + \rho v \frac{\partial h}{\partial y} = u \frac{dP}{dx} + \frac{1}{Pr} \left[\frac{\partial}{\partial y} \left(\mu \frac{\partial h}{\partial y} \right) + \frac{\mu}{r} \frac{\partial r}{\partial y} \frac{\partial h}{\partial y} \right] + \mu \left(\frac{\partial u}{\partial y} \right)^2 \quad 3.11$$

Equations 3.9 to 3.11 were transformed in Reference 16 to almost two-dimensional form, and an explicit expression for the boundary layer growth derived for $Pr = 1$, neglecting the pressure gradient. The neglect of the pressure gradient in the solution of the boundary layer equations is not considered to be a serious limitation to the solution if the proper pressure level is accounted for (reference flat plate results). This is taken into account in the iteration procedure. In addition, the solution accounting for transverse curvature is presented only to first order, and Probstein and Elliott emphasize that the first-order effect of transverse curvature and a self-induced type of pressure gradient are independent and can be calculated separately.

To first order, the solution is then as follows:

$$\delta^*/\delta_M^* = 1 + \xi(F_1/F_0 - F_0/2) + \dots, \quad 3.12$$

where δ_M^* is the Mangler value representing the zero-order solution as obtained from Equation 3.7, and the quantity $\xi(F_1/F_0 - F_0/2)$ is the first-order correction accounting for the effects of the transverse curvature. This correction is presented in Reference 16 as a series

Ford Motor Company
AERONAUTRONIC DIVISION

of integral expressions, which, in turn, are expressed in terms of the zero-order and first-order boundary layer profile of velocity and temperature. By specifying a specific geometry (viz., a cone) the first-order correction has been evaluated by planimeter using graphical integrations. To the accuracy of this type solution, the results are as follows:

$$F_0 = 1.721 \frac{T_w}{T_e} + 0.664 \frac{\gamma-1}{2} M_e^2 \quad 3.13$$

$$F_1 = (0.330 + 1.277 \frac{T_w}{T_e} + 0.218 \frac{\gamma-1}{2} M_e^2) \frac{T_w}{T_e} \\ + (0.517 + 0.913 \frac{T_w}{T_e} + 0.233 \frac{\gamma-1}{2} M_e^2) \frac{\gamma-1}{2} M_e^2 \quad 3.14$$

$$\xi \equiv \sqrt{\frac{C}{3Re}} \quad \frac{1}{\tan \theta} \quad 3.15$$

The correction has been calculated for $\gamma = 1.4$ ($Pr = 1$) and given in Figure 3-2 and Figure 3-3 as $(\delta^*/\delta_M^* - 1) 1/\xi$ versus M_e for values of $T_w/T_e = 0, 1.0$, and $(1 + \frac{\gamma-1}{2} M_e^2)$. Heat transfer plays a very important role, as well as Mach number, in determining the correction factor. Probstein and Elliott examined the case of the insulated wall at $M_e = 3.16$. They found a value of +0.073 for the ordinate in Figure 3-3 (compared to 0.03 in the present calculations, which is considered fair accuracy for the calculations) in contrast to what might be expected from a favorable pressure gradient analogy. They did observe that when the effect of compressibility is considered, the correction does become negative for a sufficiently large Mach number. This agrees with the present calculations. They apparently failed to observe, however, the important effect of heat transfer. For $T_w/T_{Aw} < 1$, it is possible for the correction to increase with increasing local Mach number. Physically, this may be explained by the very high densities near the wall in the case of the highly cooled body. The cold wall distorts the velocity profile to increase the boundary layer thickness, insofar as the effects of transverse curvature are concerned. The Mangler thickness, δ_M^* , however, still exhibits a characteristic decrease as the wall is cooled.

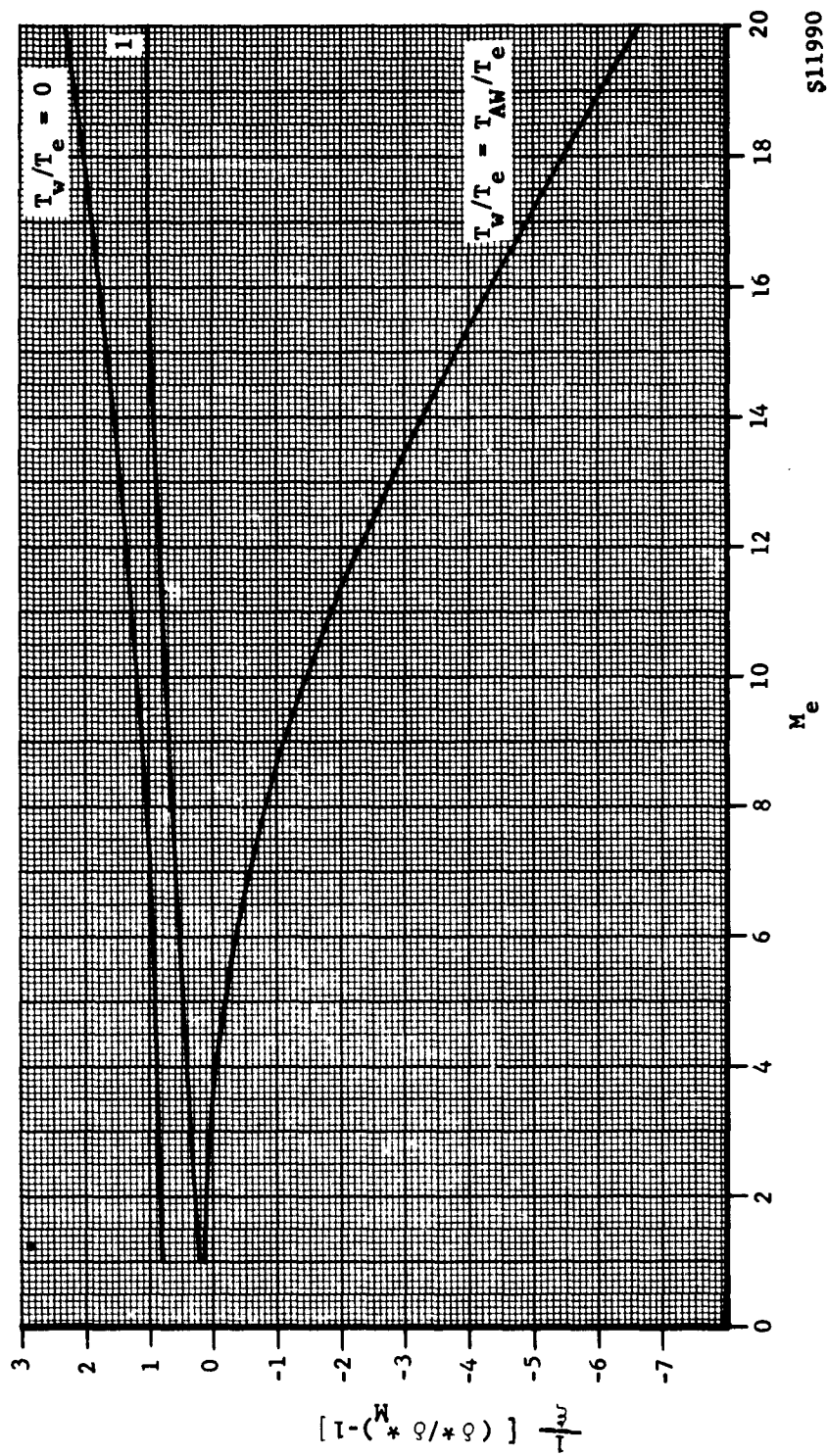


FIGURE 3-2. TRANSVERSE CURVATURE CORRECTION FOR BOUNDARY LAYER THICKNESS

S11990

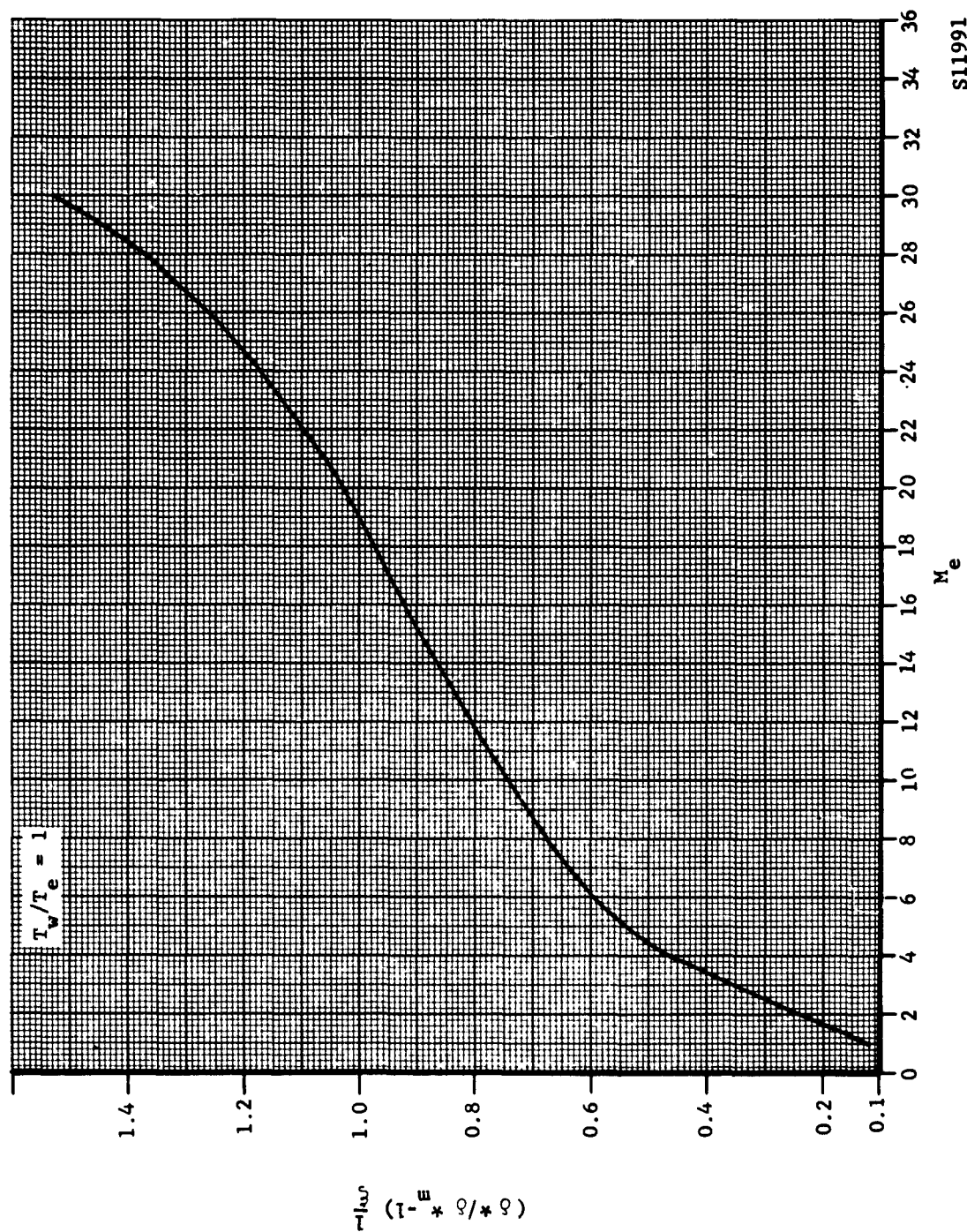


FIGURE 3-3. TRANSVERSE CURVATURE CORRECTION FOR BOUNDARY LAYER THICKNESS

S11991

Ford Motor Company
AERONUTRONIC DIVISION

Concerning the iteration procedure, the question arises as to exactly what value of the equivalent body should be used. The usual procedure is to use the tangent cone method, where an equivalent cone is formed locally at each axial position by increasing the actual cone angle, σ , by the amount, $\tan^{-1}(d\delta^*/dx)$. The slope of the displacement thickness is thus required to find each successive iterated body. The viscous interaction effects are accounted for by using the local flow properties in the calculation of the slope of the displacement thickness. As in Solution 1, the tangent cone method will also be followed here. The local slope of the displacement thickness will be obtained by differentiating the applicable equation for the displacement thickness; then

$$\frac{d\delta^*}{dx} = \frac{1}{2} (\delta^*_M/x) \quad 3.16$$

$$\sigma \text{ equiv. body} = \tan^{-1} \left(\frac{d\delta^*}{dx} \right) + \sigma \quad 3.17$$

The determination of the shock slope and standoff distance, however, will be obtained in this solution by using first-order hypersonic small disturbance theory, instead of NACA Report Number 1135. The geometry of the flow regions can then be described; as well as allowing a comparison of iteration procedures. The comparison will be a direct one, inasmuch as all solutions are essentially the same in the weak iteration region. The equations and procedures for the hypersonic small disturbance theory will be presented later.

For purposes of comparison, a case of practical interest was again chosen: $\sigma = 10$ degrees, $M_\infty = 20$, $T_w/T_e = 1.0$, as a function of altitude. The following designations will be used to identify the results:

Solution 1a - Van Driest with pressure correction (Lees and Probstein first-order weak interaction solution)

1b - iterated Van Driest

2a - weak interaction

2b - strong interaction

3 - iterated reference solution

The results of the calculations for the boundary layer growth are presented in Figures 3-4 and 3-5. Real gas effects were also considered in Solutions 1b and 3 in evaluation of the property changes across the shock wave.

As in the case of the flat plate, the iterated and pressure corrected compressible laminar boundary layer solutions of Van Driest are in close agreement with the weak interaction theory, within the region of its applicability. The reference solution is somewhat lower in this region, being very close at 150 kilofeet, but about 11 and 12 percent lower than solutions 1a and 1b at 200 and 250 kilofeet, respectively. This difference is apparently due, for the most part, to the viscosity value assumed in the boundary layer equations. A slight difference is also accounted for by the method for determining the local shock slope. The difference between the solutions 1a and 1b, and the reference method would have been reduced to 9.4 and 9.3 percent at 200 and 250 kilofeet respectively, if NACA Report Number 1135 had been used instead of hypersonic small disturbance theory. The difference between the reference method and interaction theory is due to the iteration procedure. The boundary layer thickness would be reduced by the iteration if this solution is considered to be a first approximation to the case of a thickened boundary flow due to viscous interaction. This reduction occurs because of the favorable (negative) pressure gradient. Order of magnitude estimates of the reduction based on Equation 2.13, (see p. 348 of Reference 1), are in close agreement with Figure 3-4.

As the viscous interaction effects increase, the weak interaction solution diverges strongly from the other solutions. Solutions 1a, 1b and 3 agree reasonably well in the range studied, but the strong interaction solution (2b) is low. The matching point for the interaction solution occurs between 250 and 300 kilofeet for the 10 degree cone at $x = 1$ foot. The effect of the transverse curvature would be expected to be felt at this point. The results of Figure 3-4 tend to verify this statement. It is noted that the calculations show the effects of transverse curvature to be negligible in the weak interaction region, and vigorously manifested in the strong interaction region solely at 350 kilofeet. Solution 2b is lower than the reference method at 350 kilofeet by about 46 percent. It appears that in the case of slender cones with the thickened boundary layers occurring with large viscous interaction, Solution 2b is not valid. It is also noted that the transverse curvature does not alter the local body slope, but causes only a uniform change in thickness; therefore, it thus produces no change in the induced pressures.

The same general comments also apply to the comparison at values of $x \neq 1$, as seen in Figure 3-5.

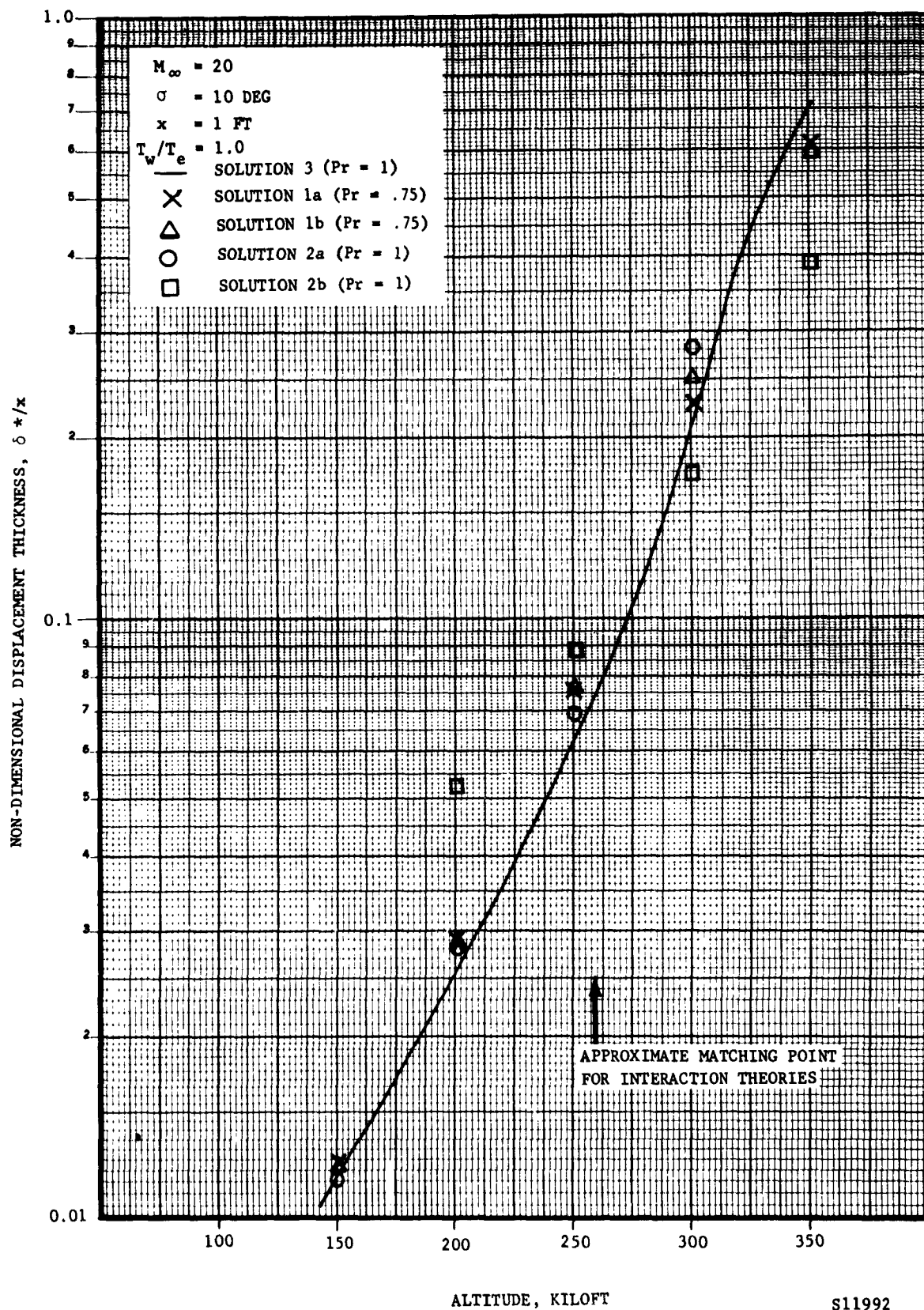


FIGURE 3-4. COMPARISON OF VARIOUS METHODS FOR COMPUTING DISPLACEMENT THICKNESS ON A CONE

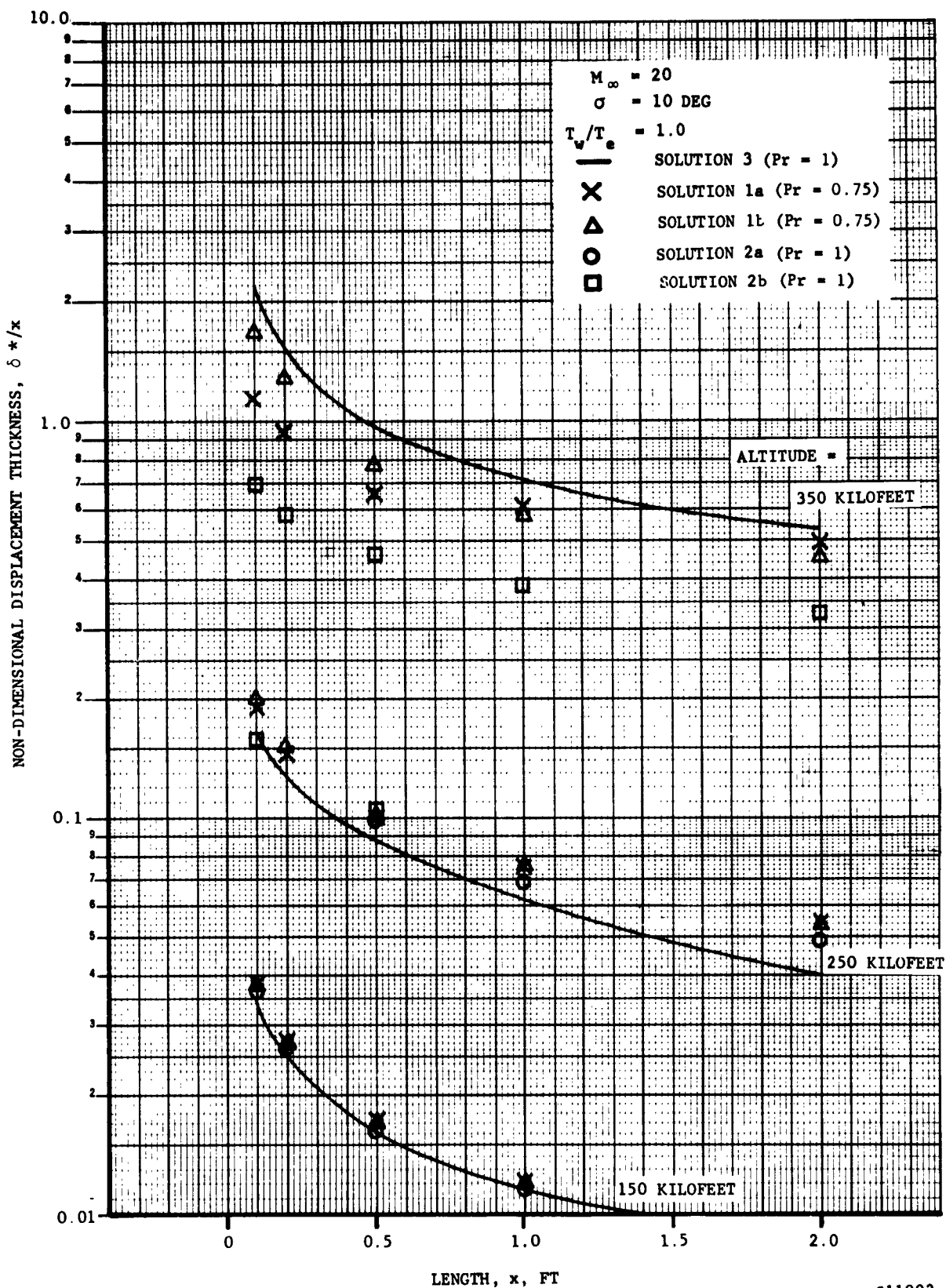


FIGURE 3-5. COMPARISON OF VARIOUS METHODS FOR COMPUTING BOUNDARY LAYER GROWTH ON A CONE

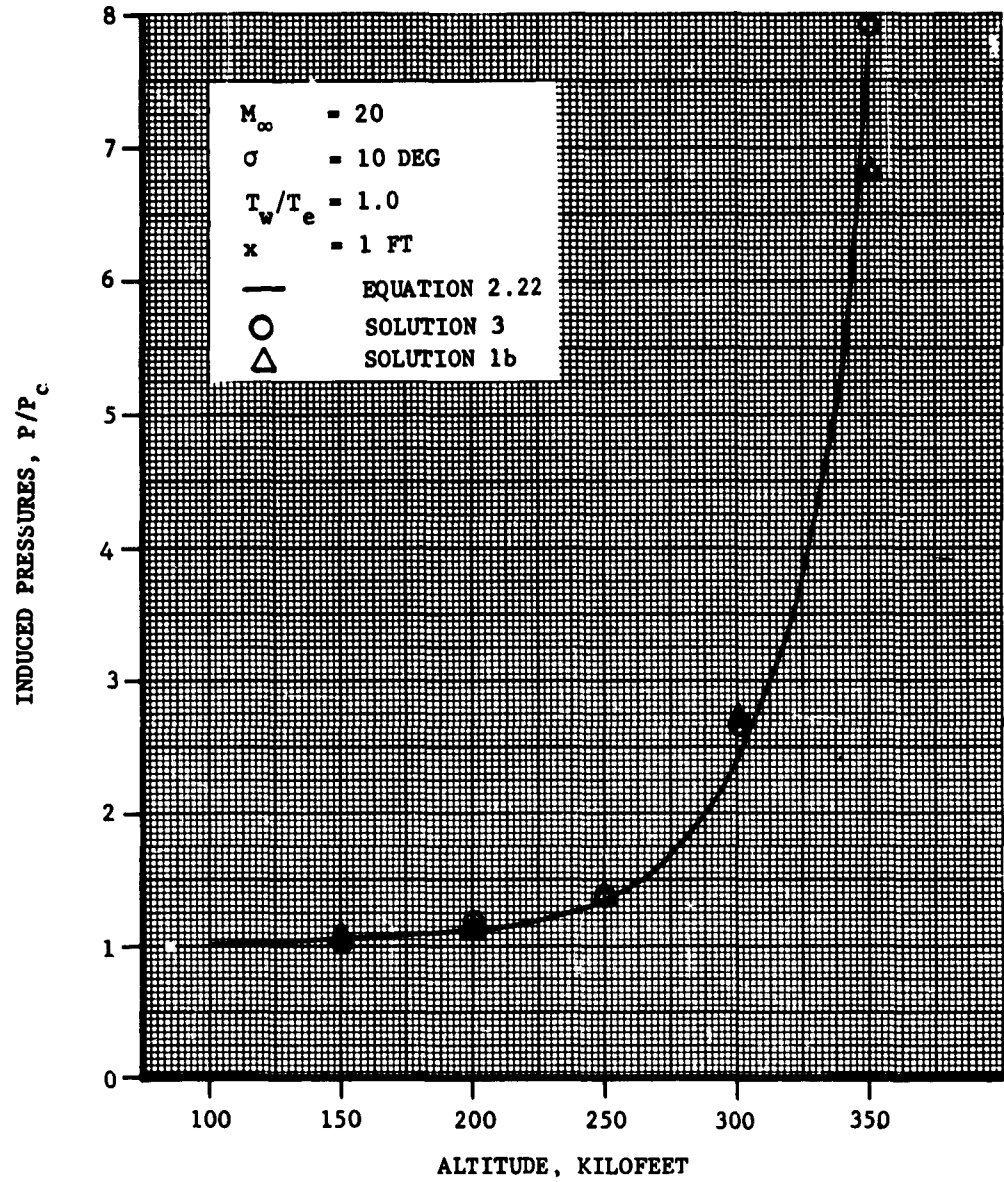
Another indication of the validity of the methods compared for the boundary layer thickness is to compare the induced pressures predicted by the iteration solutions. These results are presented in Figures 3-6 and 3-7. Away from the vertex, all solutions agree with the first-order interaction theory of Lees and Probstein to 300 kilofeet. At 350 kilofeet, solution 1b falls considerably below the other two methods at $x \neq 1$ foot. Near the vertex, the agreement is not as good (Figure 3-7). The main difference between solutions 1b and 3 is due to the equivalent body slope as obtained from the boundary layer thickness calculations. This, then, can be traced back to the assumption made for the viscosity-temperature relationship. The accuracy of any of the methods very near the vertex, however, or at 350 kilofeet, is open to considerable question; due to the neglect of other important considerations, such as slip flow, nonequilibrium flow effects, etc. The calculations at these conditions are primarily of academic interest, and to indicate general trends.

Some experimental results are available in Reference 17 for induced pressures on 3° semi-vertex angle cones. Sample calculations by Solution 3 have been carried out to compare with this data at one condition. These results are given in Figure 3-8. Since $M_\infty \theta_b < 1$, the interaction theory is not valid for these test data. The test models were cooled to thermal equilibrium and then the pressure measurements were taken. The models were therefor, at or, slightly greater than the adiabatic wall temperature. The induced pressure increment $(P_2 - P_c)/P_c$ is very low. It was found that the magnitude of the increment at these low levels was extremely sensitive to the accuracy of the calculations. Since the calculations were carried out by hand, the deviation of prediction and data is within the possible error involved in the calculations.

On the basis of the comparison just made, and from the standpoint of ease of calculation, it is recommended that the boundary layer growth on a cone be computed as follows:

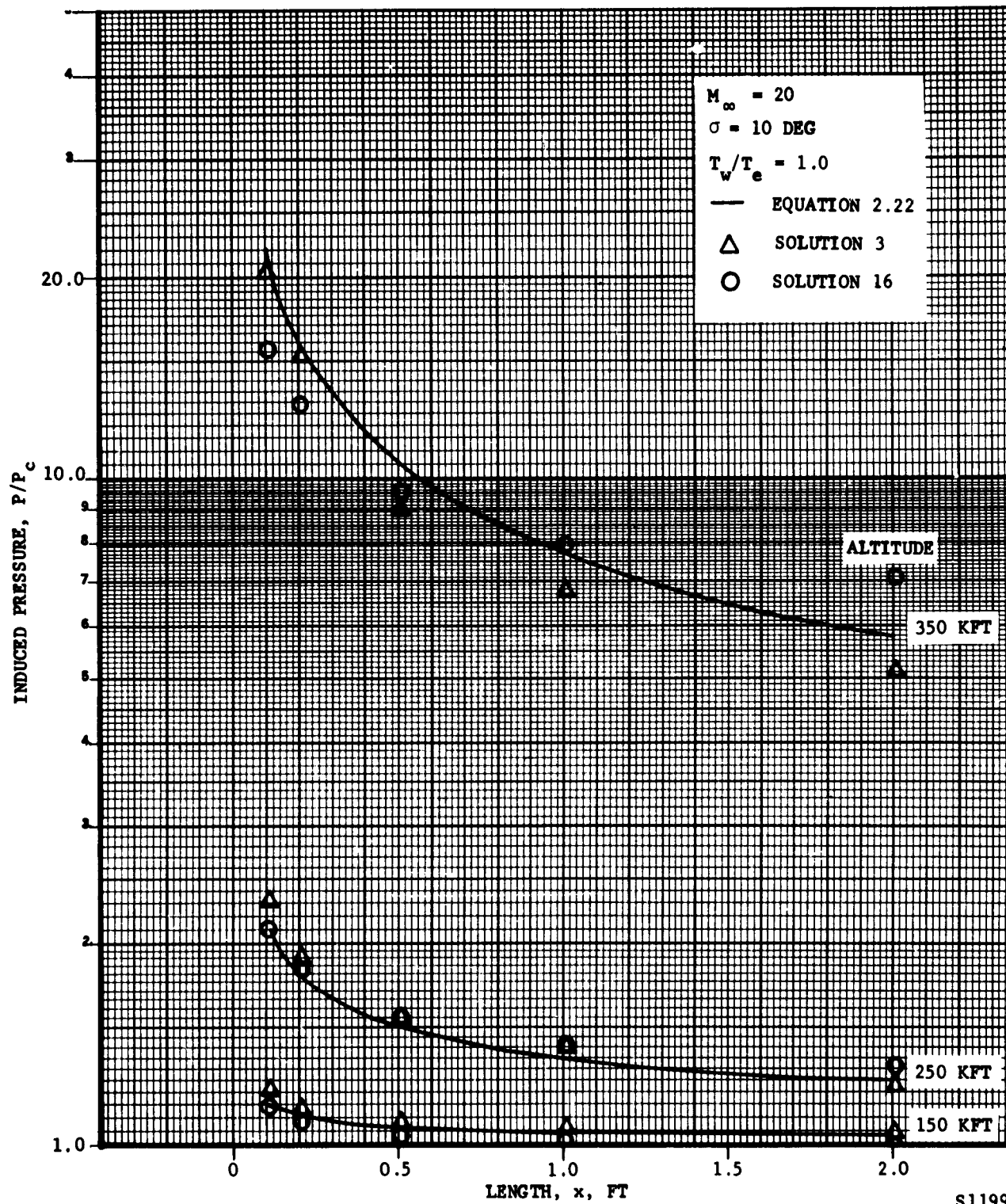
1. Solution 2a (weak interaction) may be used in the weak interaction region.
2. Solution 1a (Van Driest with Lees and Probstein first-order weak interaction pressure correction) may be used to extend solution 2a into the strong interaction region.

The first-order weak interaction solution of Lees and Probstein for predicting the induced pressures should be appropriate. It is felt that these results for the boundary layer growth and induced pressures should be applicable to cones with $\sigma \neq 10$ degrees in the range $5^\circ < \sigma < 20$ degrees.



S11994

FIGURE 3-6. COMPARISON OF INDUCED PRESSURES AS A FUNCTION OF ALTITUDE



S1199

FIGURE 3-7. COMPARISON OF PRESSURE DISTRIBUTIONS ON A CONE

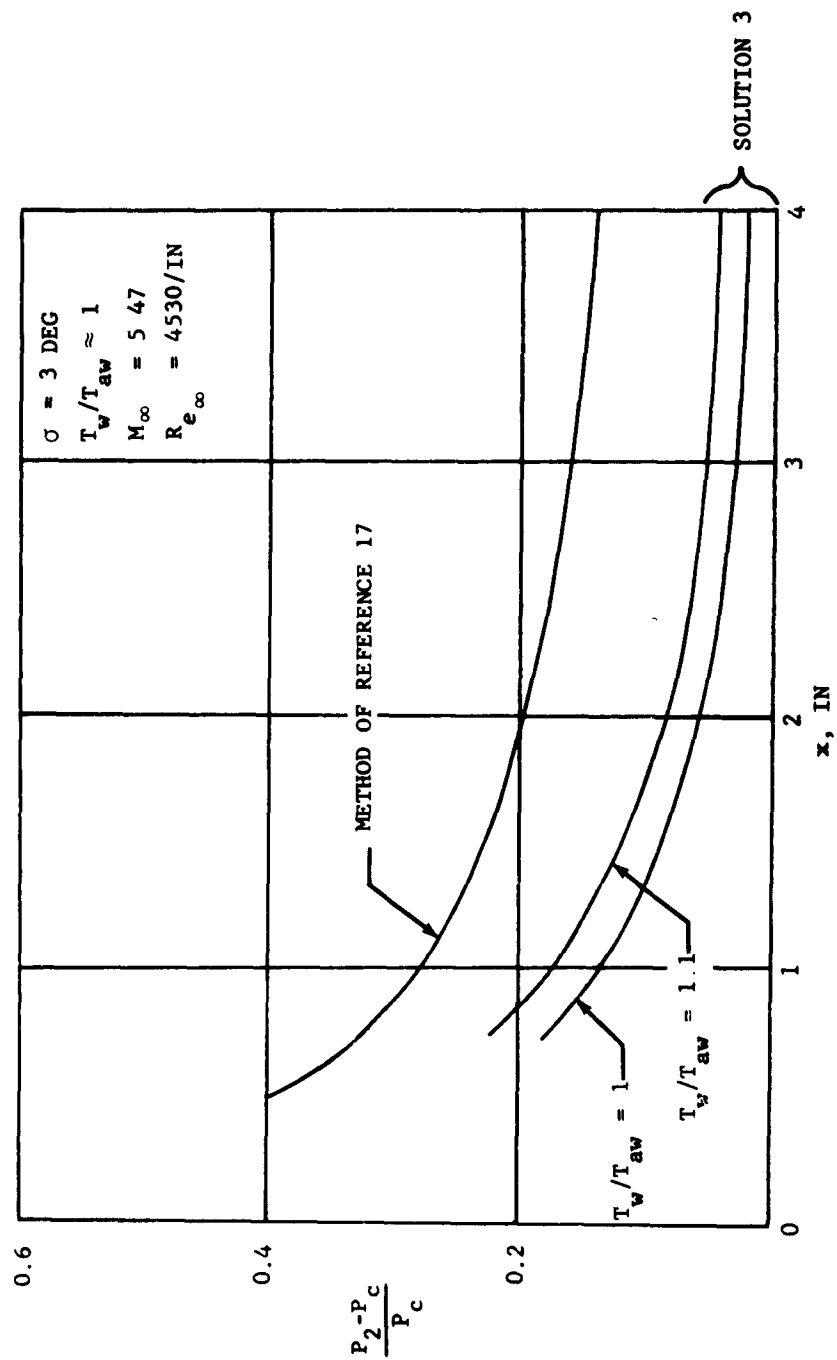
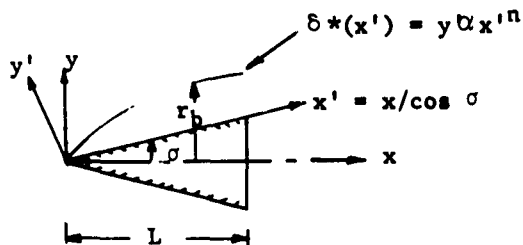


FIGURE 3-8. INDUCED PRESSURE INCREMENT ON A CONE (DATA OF REFERENCE 17)

S11996

3.2 DETERMINATION OF EQUIVALENT POWER LAW BODY AND SHOCK SHAPE.

The growth of the boundary layer on a cone has already been determined as $\delta^*(x')$, where



We may now show that a boundary layer growth of the type described over this sharp, slender cone produces a new equivalent body characterized by:

$$y_{\text{equiv}} = r_b \alpha x^m, \quad 1/2 \leq m \leq 1 \quad 3.18$$

The rotation of the (x', y') coordinates into the (x, y) coordinate system is given by:

$$\left. \begin{aligned} x &= x' \cos \sigma - y' \sin \sigma \\ y &= x' \sin \sigma + y' \cos \sigma \end{aligned} \right\} \quad 3.19$$

In the (x', y') coordinate system, the boundary layer growth is:

$$\delta^* = y' = K x'^n, \quad 1/2 \leq n \leq 3/4 \quad 3.20$$

It can be shown that $0 < K \leq 1$, where $K \rightarrow 0$ as $Re \rightarrow \infty$. In the (x, y) coordinate system, the substitution of Equation 3.18 and 3.19 gives:

$$y_{\text{equiv}} = r_b = \frac{K x^n}{\cos \sigma} \left(1 + \frac{r_b}{x} \tan \sigma \right)^n + \tan \sigma \quad 3.21$$

For slender bodies with $\tan \sigma \ll 1$, $n < 1$,

$$r_b \approx \frac{Kx^n}{\cos \sigma} \left(1 + n \frac{r_b}{x} \tan \sigma \right) + x \tan \sigma \quad 3.22$$

and

$$r_b = \frac{\cos \sigma \tan \sigma x^{1-n} + K x^{2-n}}{\cos \sigma x^{1-n} - Kn \tan \sigma} = \frac{[(x \cos \sigma)^{1-n} \tan \sigma + K] x}{(x \cos \sigma)^{1-n} - K n \tan \sigma} \quad 3.23$$

It is now postulated that:

$$r_b \propto x^m \quad 3.24$$

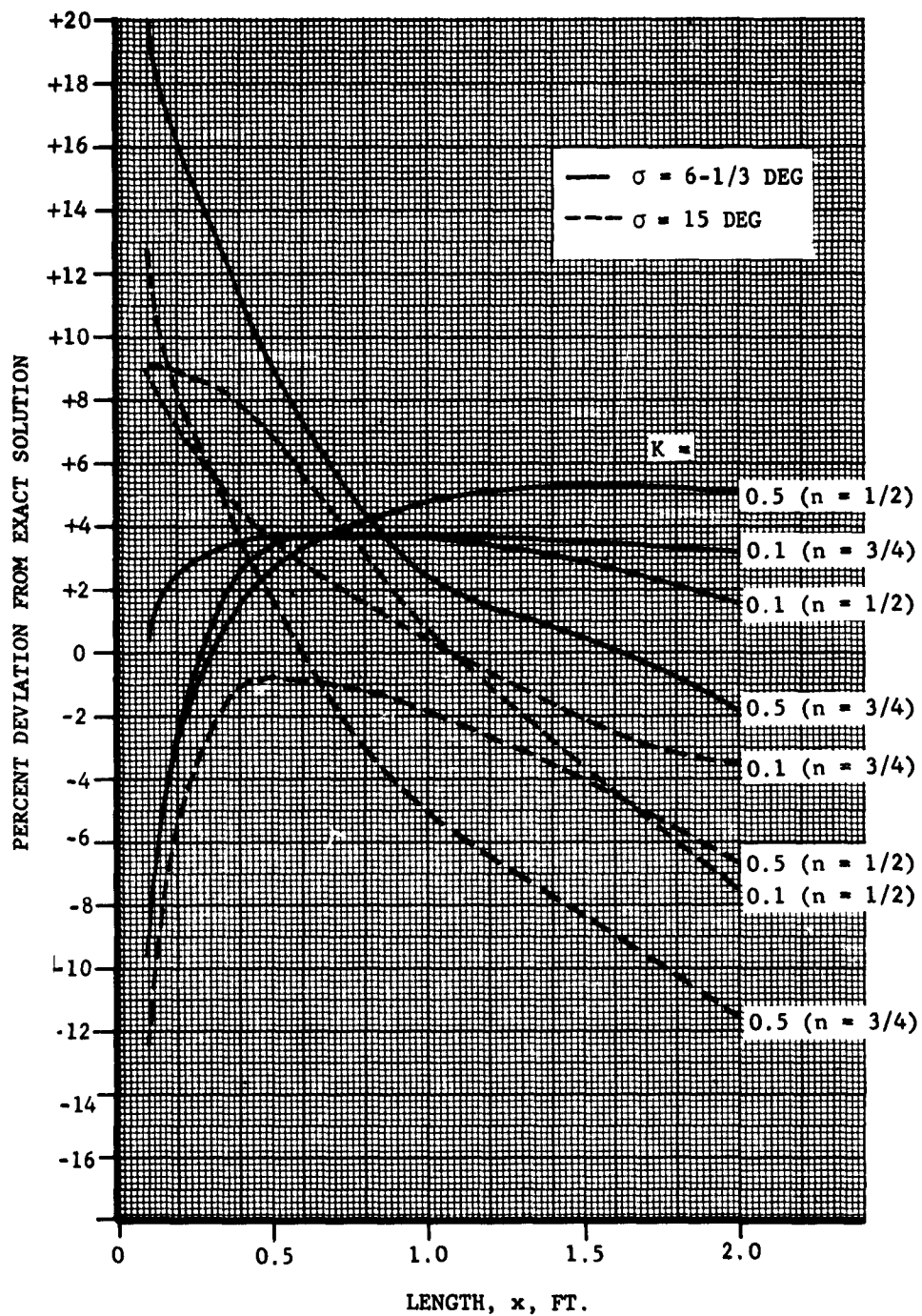
An empirical correlation was made to determine the constant of proportionality in 3.24 by comparison to 3.23. This results in:

$$r_b = (\tan \sigma + 1.10 K) x^{0.30 - (1-n)K} \quad 3.25$$

The percent deviation of the empirical value of r_b from that of the exact value of r_b is given in Figure 3-9 for several values of the determining parameters. The deviation ranges from -13 to +20% at $x = 0.1$.

The accuracy of a point so near the leading edge is somewhat questionable. The region of primary interest is considered to be $0.5 \leq x \leq 2$, where the agreement is approximately ± 5 percent.

The equations of motion for inviscid hypersonic flow over slender bodies can be reduced to simpler form by incorporating the hypersonic-slender-body-approximations. This use of small disturbance theory in hypersonic flow has been summarized by Van Dyke¹⁸. The reduced equations are valid provided $\delta \ll 1$ and $1/M_\infty \delta \leq O(1)$, where δ is a characteristic body or streamline slope, and M_∞ is the freestream Mach number. Approximate analytical solutions for the inviscid hypersonic flow over power law bodies of the type $r_b \propto x^m$ has been given by Mirels¹⁹. The resulting equations give the zero-order and first-order hypersonic flow over those blunt-nosed configurations whose zero-order shock shape follows a power law variation. If the classical concept of the Prandtl displacement thickness is considered, it is seen that in the high altitude high Mach number region of interest, the thickened boundary



S11997

FIGURE 3-9. DEVIATION OF EMPIRICAL BODY RADIUS FROM EXACT SOLUTION

layer growth on a sharp cone produces an equivalent body which is effectively blunted. Since the boundary layer growth can be expressed as a power law variation of the cone's slant length, it is to be expected that the equivalent body can be represented as a power law body. This has just been verified by an empirical correlation. Within the accuracy of the hypersonic small disturbance theory, a method is available to estimate the entire inviscid flow field downstream of the vertex, assuming of course, that the equivalent body is known, a priori. This has been determined to be the case. In the following discussion, only the applicable equations and instructions for their use will be presented, since a complete description is adequately given in References 18 and 19.

The shock shape is given by:

$$\frac{R}{r_b} = \frac{1}{\eta_b} \left[1 + \frac{a_1 \eta_b^2}{(M_\infty \delta_b)^2} \left(\frac{x}{L} \right)^{2(1-m)} \right] \quad 3.26$$

The shock slope is:

$$\frac{dR}{dx} = \frac{1}{\eta_b} \frac{dr_b}{dx} \left[1 + \frac{2-m}{m} \frac{a_1 \eta_b^2}{(M_\infty \delta_b)^2} \left(\frac{x}{L} \right)^{2(1-m)} \right] \quad 3.27$$

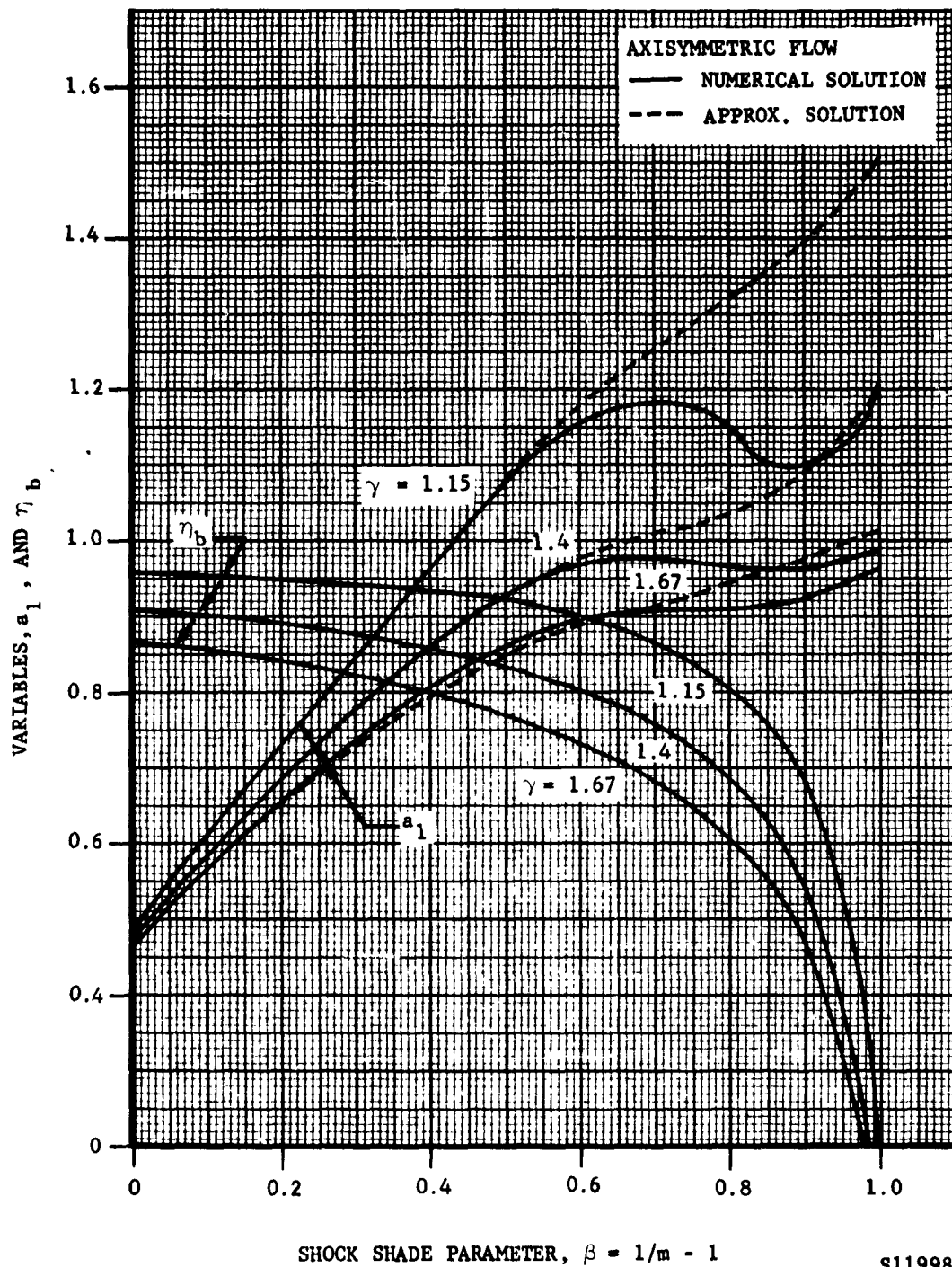
or

$$\left. \frac{dR_s}{dx} \right|_x \approx \frac{1}{\eta_b} \frac{dr_b}{dx} = \frac{1}{2} \frac{1}{\eta_b} \frac{\delta^*}{x} \quad 3.28$$

The quantities η_b and a_1 are given in Figure 3-10 as functions of γ and the pressure gradient parameter, β . The characteristic slope, δ_b , is for the slender bodies under consideration:

$$\delta_b = \left(\frac{r_b}{L} \right)_{x=L} = \frac{x}{L} \tan \sigma + \frac{\delta^*}{L} / \cos \sigma \Big|_{x=L} \quad 3.29$$

$$\approx \tan \sigma + (\delta^*/x)_{x=L}$$



S11998

FIGURE 3-10. APPROXIMATE SOLUTION FOR HYPERSONIC FLOW OVER POWER LAW BODIES (NASA TR R-15)

Ford Motor Company,
AERONUTRONIC DIVISION

The analysis of References 1, 2 and 19, indicates that for many considerations the variation of properties normal to the surface may be negligible within the accuracy of the engineering approximations employed. As an example, the constant density approximation used in Reference 2 proved highly successful, and the variation of pressure as obtained from Reference 19 was found to be negligible within approximately 5 percent for the cases of interest where a relatively thin shock layer (or inviscid region) exists. Accordingly, the present analysis will assume no variation in pressure or density (consequently, temperature as well) normal to the surface and utilize the values immediately aft of the shock wave in the inviscid flow.

CHAPTER 4

FLOW FIELD DETERMINATION OVER 6.33 AND 10 DEGREE SEMI-VERTEX ANGLE CONES

4.1 BOUNDARY LAYER AND SHOCK LAYER PROFILES

With the previous results available, we are now in a position to estimate the geometry of arbitrary conical flow fields. The temperature and density profiles therein can be obtained directly in the shock layer, but have not been ascertained for the boundary layer. A simple estimate of the boundary layer profiles may be made by using the Crocco integral expressed in terms of enthalpy^{1,2,4}:

$$\frac{h}{h_e} = \frac{h_w}{h_e} + \frac{h_{aw} - h_w}{h_e} \frac{u}{u_e} - \frac{h_{aw} - h_e}{h_e} \left(\frac{u}{u_e} \right)^2 \quad 4.1$$

where velocity is considered to be the independent variable. This result follows directly from a simultaneous solution of the momentum and energy equations for $Pr = Le = 1$, $dP/dx = 0$, and irrespective of the body shape. With a constant pressure across the boundary layer the temperature and density profiles may be determined from Equation 4.1 if the boundary conditions are known. These have been determined above. In those cases where dissociation become important, the temperatures may be obtained from Reference 20 as $T = f(h, P_2)$.

In hypersonic flow without blowing the velocity profile becomes nearly linear¹. With this approximation and Equation 4.1, a simple solution is available to estimate the entire flow field. The assumptions of zero pressure gradient and linear velocity profile are not considered to be serious limitations to the accuracy of the predicted results. As a check on the possible error involved in the zero pressure gradient assumption, a comparison of the enthalpy distributions through the boundary layer was made at $\beta = 0$ and $\beta = 0.286$. The latter condition corresponds

to a locally hypersonic flow¹ with the boundary layer growing as $x^{-1/2}$. This comparison is given in Figure 4-1. The distribution for $\beta = 0.286$ were obtained from the calculations of Li and Nagamatsu presented in Reference 21¹ for a similar solution of the boundary layer equations.

Calculations have been made for the flow fields over two cones with 6.33 and 10 degree semi-vertex angles. The computations were carried out for a typical re-entry condition of $M_\infty = 25$, at an altitude of 250 kilofeet. These results are presented in Figure 4-2 to 4-7.

4.2 HEAT TRANSFER AND SKIN FRICTION ON CONES

In a manner similar to that followed for boundary layer thickness, the skin friction and heat transfer on sharp slender cones may be evaluated. It was shown that a smooth transition from the weak to strong interaction region may be obtained by neglecting pressure gradient effects and considering only the local properties. This may be approximately accounted for by considering the change in local properties due to the induced pressures. In the case of skin friction and heat transfer however, the transverse curvature effects may not be negligible^{1,16} and should also be included in a general analysis.

Following this procedure and neglecting slip effects, the local skin friction coefficient on a sharp slender cone is given by:

$$C_f = 0.664 \sqrt{\frac{3C P/P_c}{Re_L}} \left[1 + \xi (0.517 + 0.913 \frac{T_w}{T_c} + 0.121 (\gamma-1) M_c^2) \right] \quad 4.2$$

With P/P_c given by Equation 2.22 the mean skin friction coefficient is:

$$C_F = 2 \frac{q_c}{q_\infty} \times \left\{ 0.443 \sqrt{\frac{3C}{Re_L}} (1 + F_c \bar{\chi}_c)^{3/2} + \left[2 \left(\frac{1.328C}{Re_L \tan \theta} (0.517 + 0.913 \frac{T_w}{T_c} + 0.121 (\gamma-1) M_c^2) - 1.328/F_c \bar{\chi}_c \sqrt{\frac{3C}{Re_2}} \right] \right\}$$

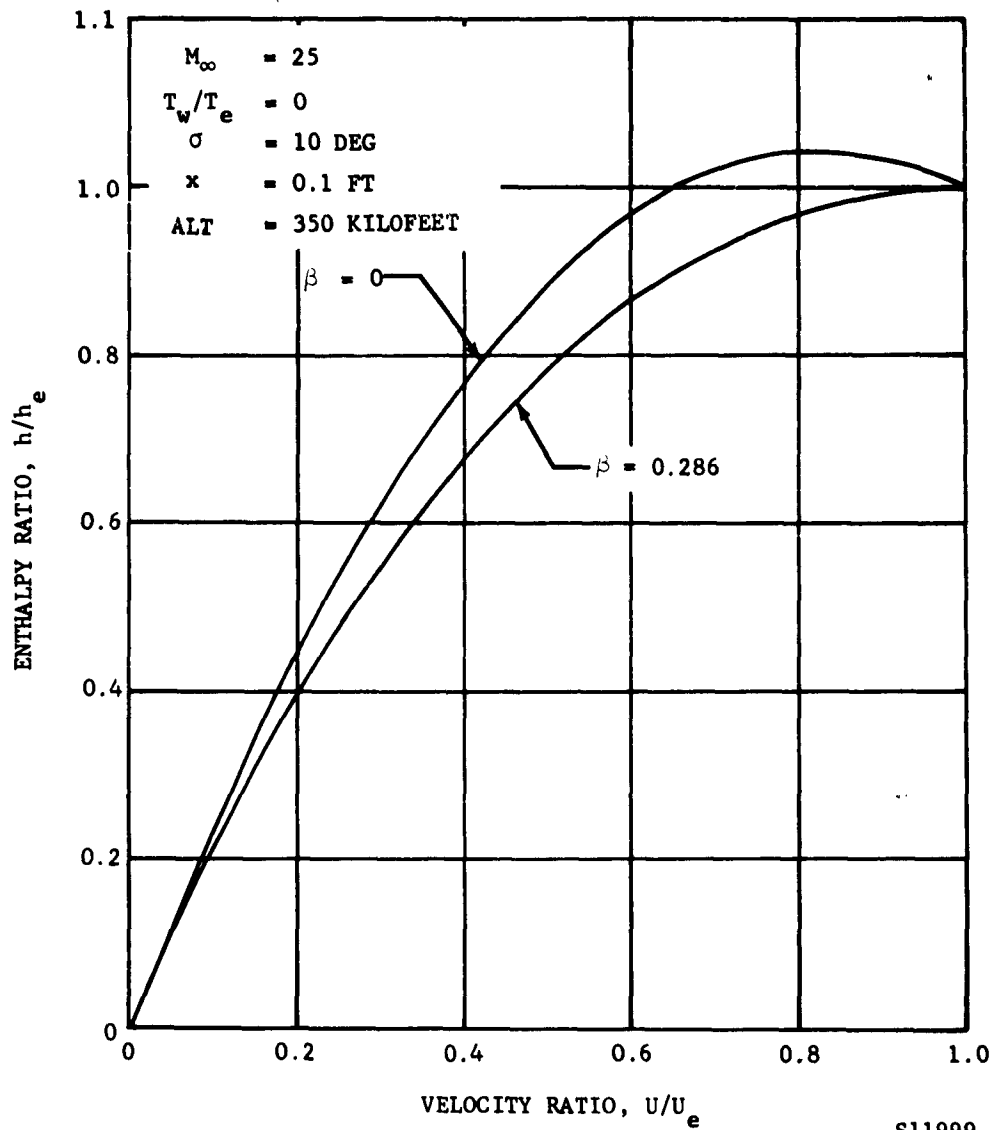


FIGURE 4-1. COMPARISON OF ENTHALPY DISTRIBUTIONS FOR EFFECT OF PRESSURE GRADIENT

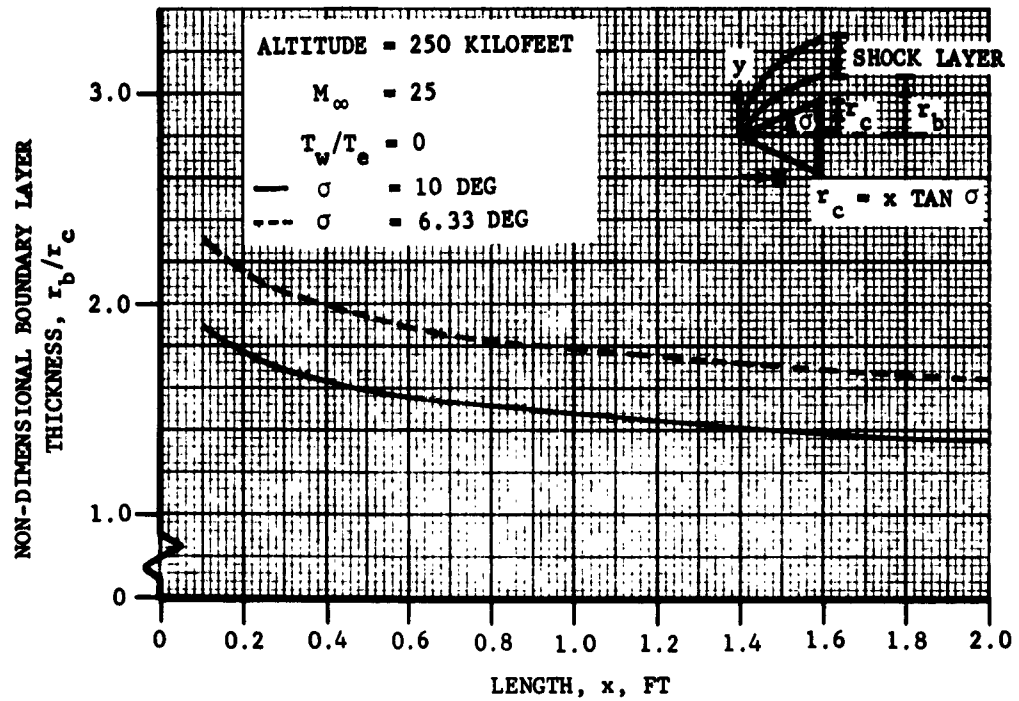


FIGURE 4-2. BOUNDARY LAYER THICKNESS

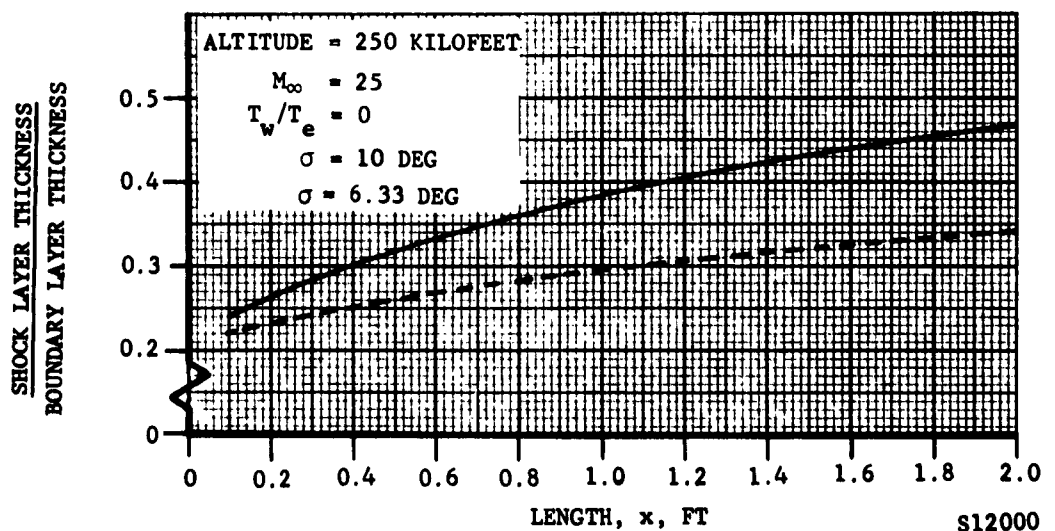


FIGURE 4 2.A. SHOCK LAYER THICKNESS

S12000

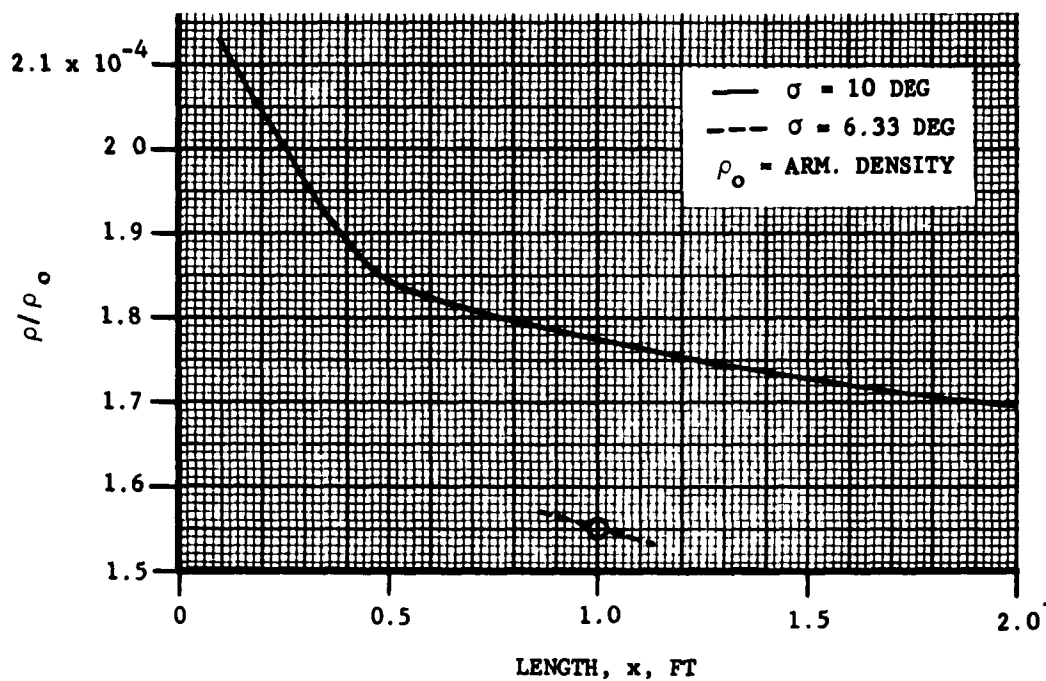


FIGURE 4-3. SHOCK LAYER DENSITIES

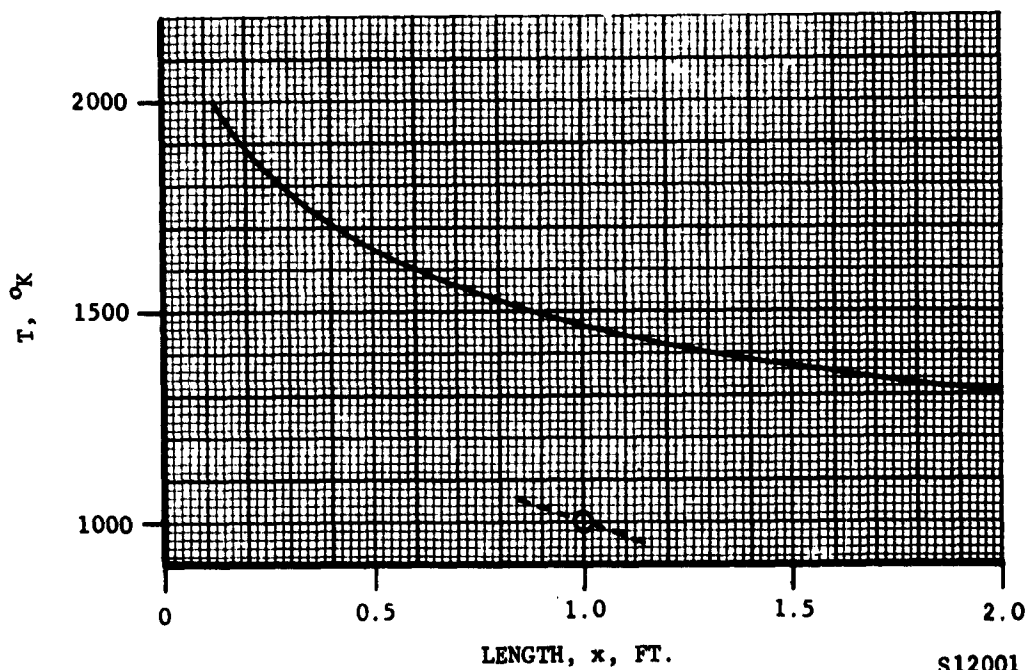
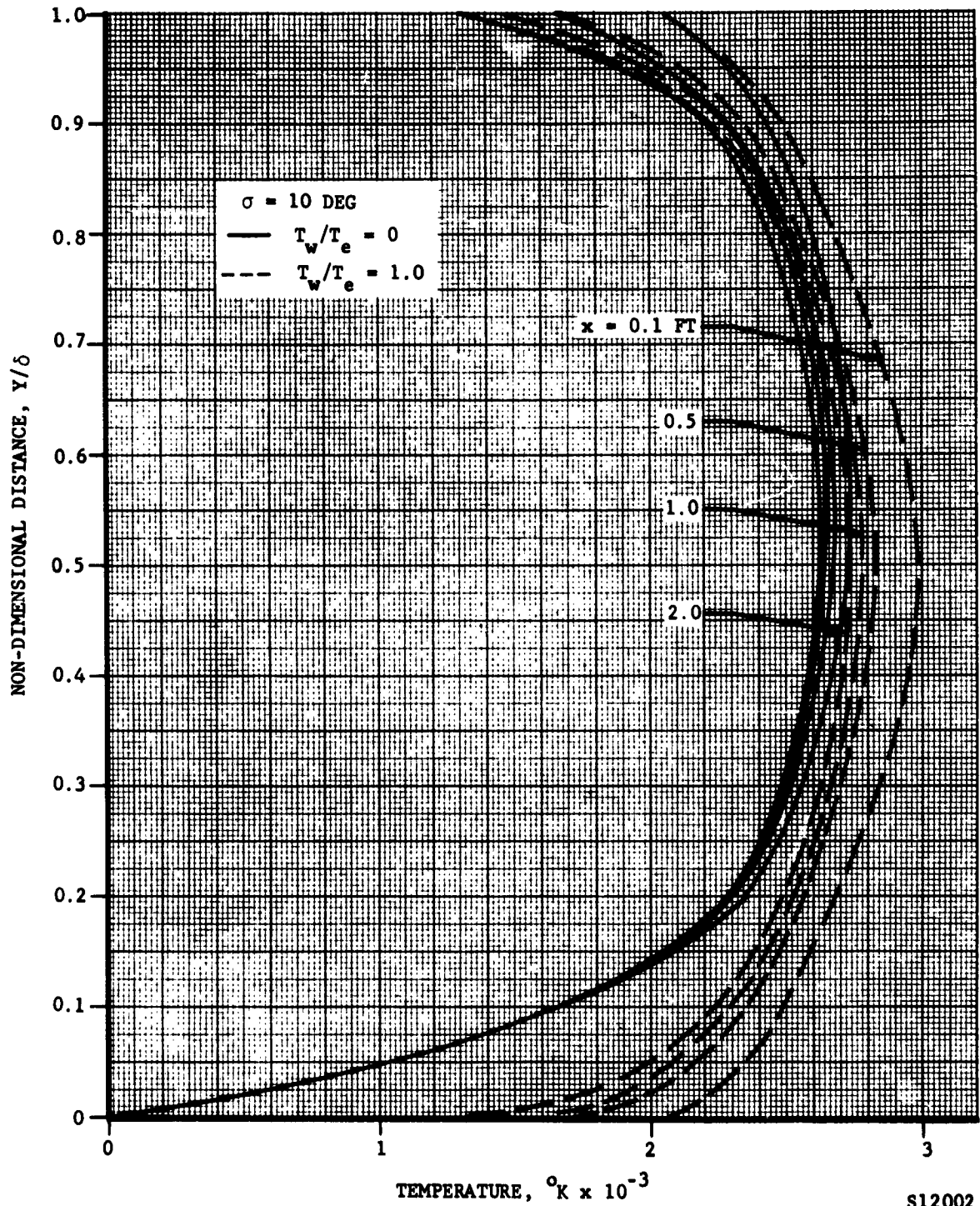


FIGURE 4-3.A. SHOCK LAYER TEMPERATURES

S12001

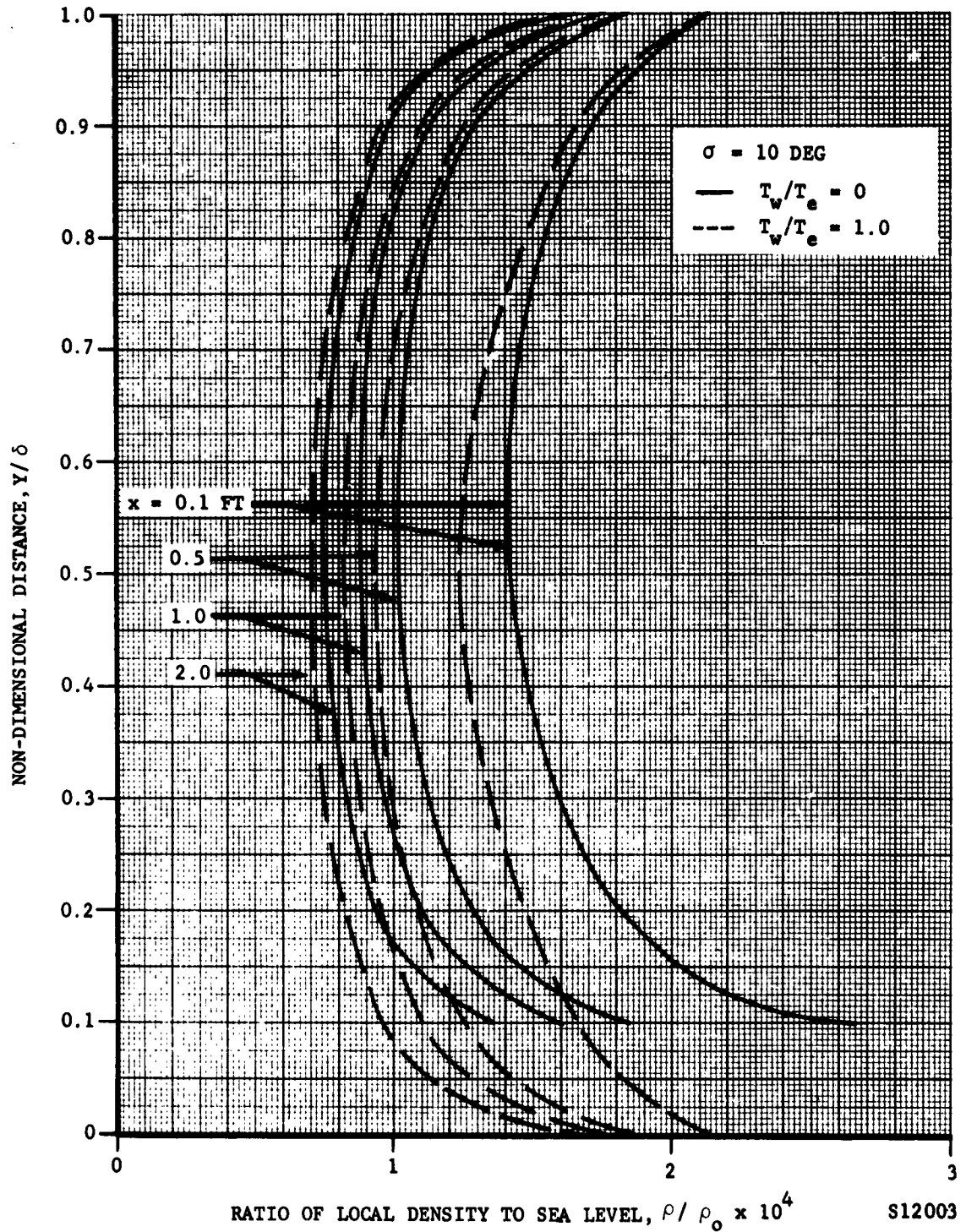
ALTITUDE = 250 KILOFEET



S12002

FIGURE 4-4 TEMPERATURE DISTRIBUTIONS ACROSS BOUNDARY LAYER

ALTITUDE = 250 KILOFEET



S12003

FIGURE 4-5. DENSITY DISTRIBUTIONS ACROSS BOUNDARY LAYER

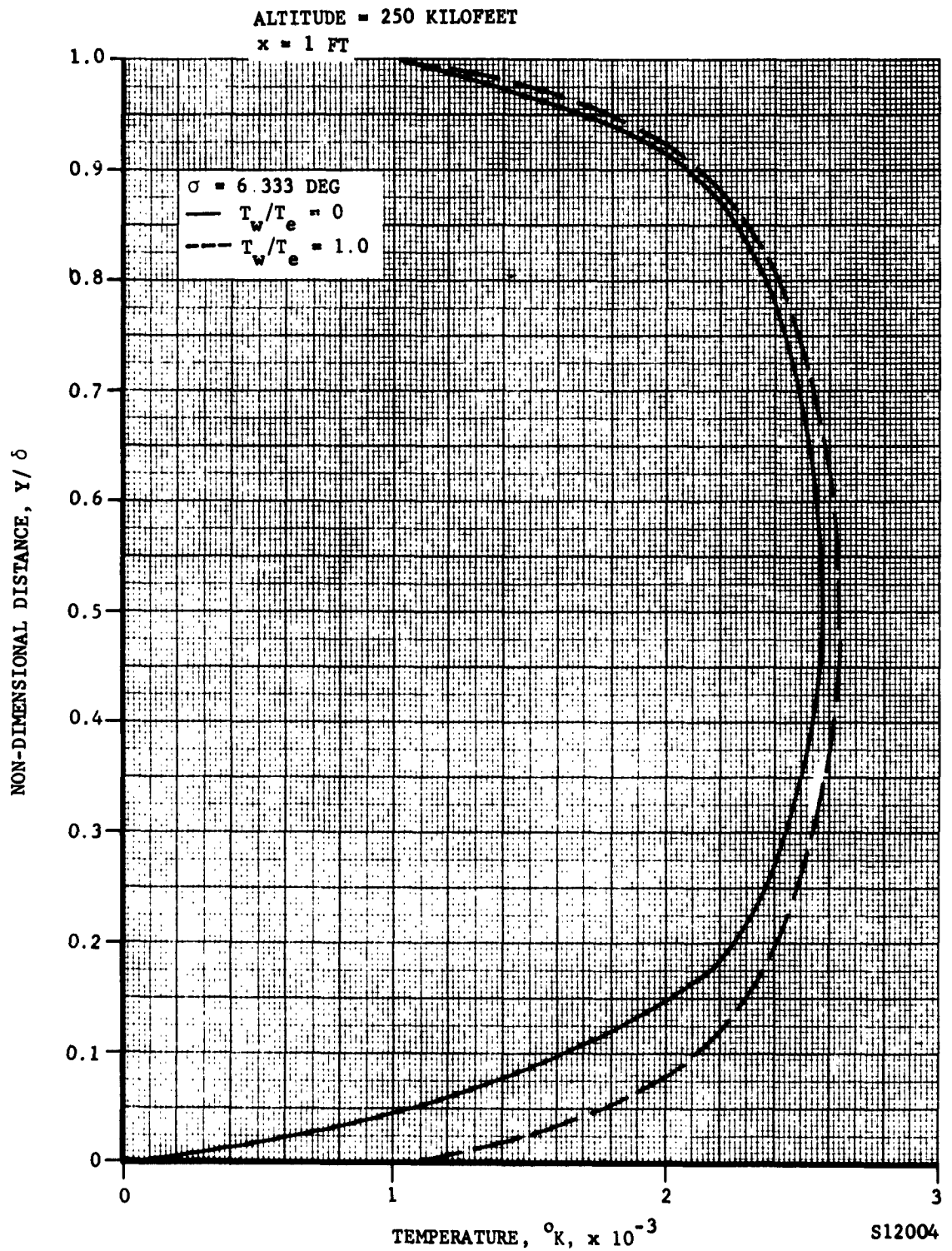
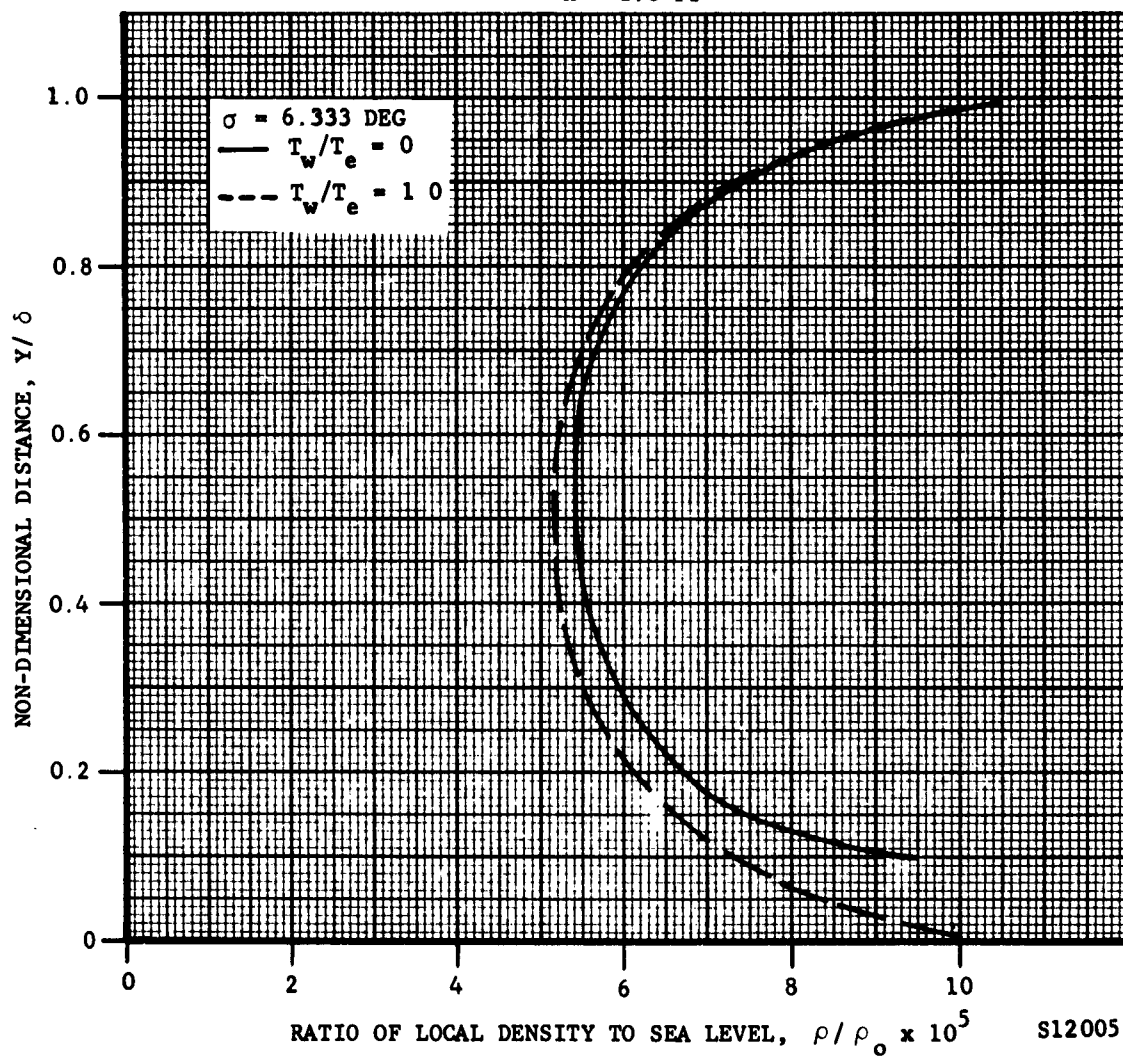


FIGURE 4-6. TEMPERATURE DISTRIBUTIONS ACROSS BOUNDARY LAYER

ALTITUDE = 250 KILOFEET
 $x = 1.0$ FT



S12005

FIGURE 4-7. DENSITY DISTRIBUTION ACROSS BOUNDARY LAYER

Ford Motor Company
AERONUTRONIC DIVISION

$$\left[\frac{(1 + F_c \bar{\chi}_c)^{3/2}}{4} - \frac{F_c \bar{\chi}_c}{8} (1 + F_c \bar{\chi}_c)^{1/2} - \frac{(F_c \bar{\chi}_c)^{1/2}}{8} \right. \\ \left. \ln \frac{1 + (1 + F_c \bar{\chi}_c)^{1/2}}{(F_c \bar{\chi}_c)^{1/2}} \right] \quad 4.3$$

Equations 4.2 and 4.3 now include both the viscous interaction and transverse curvature effects, without considering them separately. An alternate procedure for estimating the skin friction forces is to obtain a value by summation of the individual effects. With the substitution of the appropriate boundary conditions the local skin friction is obtained as:

$$\frac{C_f - (C_f)_{Mang}}{(C_f)_{Mang}} = \left[-1.152 + 0.733 \frac{T_w}{T_c} + (0.528\gamma - 0.126)M_c^2 \frac{F_c \bar{\chi}_c}{\gamma M_c^2} \right] \quad 4.4$$

As mentioned previously, transverse curvature might have a significant effect on the local skin friction. The first-order transverse curvature correction to the local skin friction is given by Probstein and Elliot in Reference 16 as:

$$\frac{C_f - (C_f)_{Mang}}{(C_f)_{Mang}} = \left[0.517 + 0.913 \frac{T_w}{T_c} + 0.121(\gamma - 1)M_c^2 \right] \frac{1}{\sqrt{3} \tan \theta_c} \sqrt{\frac{C_c}{(R_x)_c}} \quad 4.5$$

The total local skin friction including interaction and transverse curvature is now:

$$C_f = 0.664 \sqrt{\frac{3C_c}{(R_x)_c}} \left[1 + \frac{C_{ot} \theta}{\sqrt{3} M_c^3} (0.517 + 0.913 \frac{T_w}{T_c} + 0.121(\gamma - 1)M_c^2 \bar{\chi}_c \right. \\ \left. + \frac{F}{\gamma} \left\{ 0.528 \gamma - 0.126 + \frac{0.733}{M_c^2} \frac{T_w}{T_c} - \frac{1.152}{M_c^2} \right\} \bar{\chi}_c \right] \quad 4.6$$

We may express the local heat transfer rate (by utilizing Reynold's analogy) in terms of a Stanton number:

$$St_l = \frac{C_f}{2} \frac{1}{Pr^*} \equiv P_r^{*\frac{2}{3}} \quad 4.7$$

where,

$$St_l \equiv \frac{h_l}{\rho^* u_e C_p} \quad 4.8$$

and the local heat transfer rate is given by:

$$\left(\frac{Q}{A} \right)_l = St_l \rho^* u_e (H_{Aw} - H_w) \quad 4.9$$

4.3 AXIAL FORCE COEFFICIENT AT ZERO ANGLE OF ATTACK

In order to check the above results, a comparison with experimental data for axial force coefficients measured in a hot shot tunnel²² at $M_\infty = 20$ has been made. The axial force coefficient is obtained by adding the individual contributions for the axial force:

$$C_{A_{\alpha=0}} = C_A^F + C_A^B + C_A^N + C_A^P \quad 4.10$$

The force components, C_A^n , are estimated by:

$$C_A^F = C_F \frac{A_c}{A_{ref}} \cos \sigma \text{ (integrated skin friction drag)}$$

$$C_A^B = - \left(\frac{P_B}{P_\infty} - 1 \right) \frac{A_B}{A_{ref}} / \frac{\gamma}{2} M_\infty^2 \text{ (base drag)}$$

$$C_A^N = \left(\frac{P_{t2}}{P_\infty} - 1 \right) \frac{A_n}{A_{ref}} / \frac{\gamma}{2} M_\infty^2 \text{ (flat nose drag)}$$

Ford Motor Company

AERONAUTRONIC DIVISION

$$C_A^P = \frac{1}{\frac{\gamma}{2} M_\infty^2} \left[\frac{P_c}{P_\infty} \left(1 + \frac{4}{3} \gamma F_c \bar{\chi}_c \right) - 1 \right] \quad \text{(pressure drag from Equation 2.22)}$$

Results for this comparison is presented in Figure 4-8. The base pressure, P_B , has been estimated from Reference 23. The contributions, C_A^B and C_A^N are negligible at the lower Reynolds numbers. The maximum deviation is about ± 10 percent. It is felt that the analytical estimates are adequate within the accuracy of the assumptions involved. The principal assumptions to be considered are the neglect of slip effects and the approach employed in using Equation 4.10. It is also noted that C_A is very sensitive to the accuracy of the calculations and the methods employed for computing the inviscid flow values. As an example, the use of $\frac{Re_c}{Re_\infty} = 1.20$ (instead of the value used, e.g., 1.50) increases C_A by about 14.3 percent at $Re_{0\infty} = 1 \times 10^4$. For this wind tunnel data, the calculations are especially sensitive to the viscosity. At the low temperatures involved, Sutherland's law is inadequate, and data was used from NAVORD Report 1488 (Vol. 5).

Comparison with experimental data has also been made by using the summation method for obtaining the skin friction forces:

$$C_{D_F} = 1.53 \cot \theta_c \frac{q_c}{q_\infty} \sqrt{\frac{C_c}{(R_L)_c}} \left[1 + \frac{\cot \theta_c}{M_c^3} \left\{ 0.446 + 0.788 \frac{T_w}{T_c} + 0.105 (\gamma - 1) M_c^2 \right\} (\bar{\chi}_L)_c + \frac{3}{2} \frac{F}{\gamma} (0.528 \gamma - 0.126 + \frac{0.733}{M_c^2} \frac{T_w}{T_c} - \frac{1.152}{M_c^2}) (\bar{\chi}_L)_c \right] \quad 4.11$$

At the lower Mach numbers ($M < 10$) the base drag contribution can be significant and it is necessary to know the value of the ratio P_B/P_∞ . This is a rather complex calculation since it appears to be a function of the local flow conditions at the base of the vehicle as well as the local boundary layer characteristics²⁵.

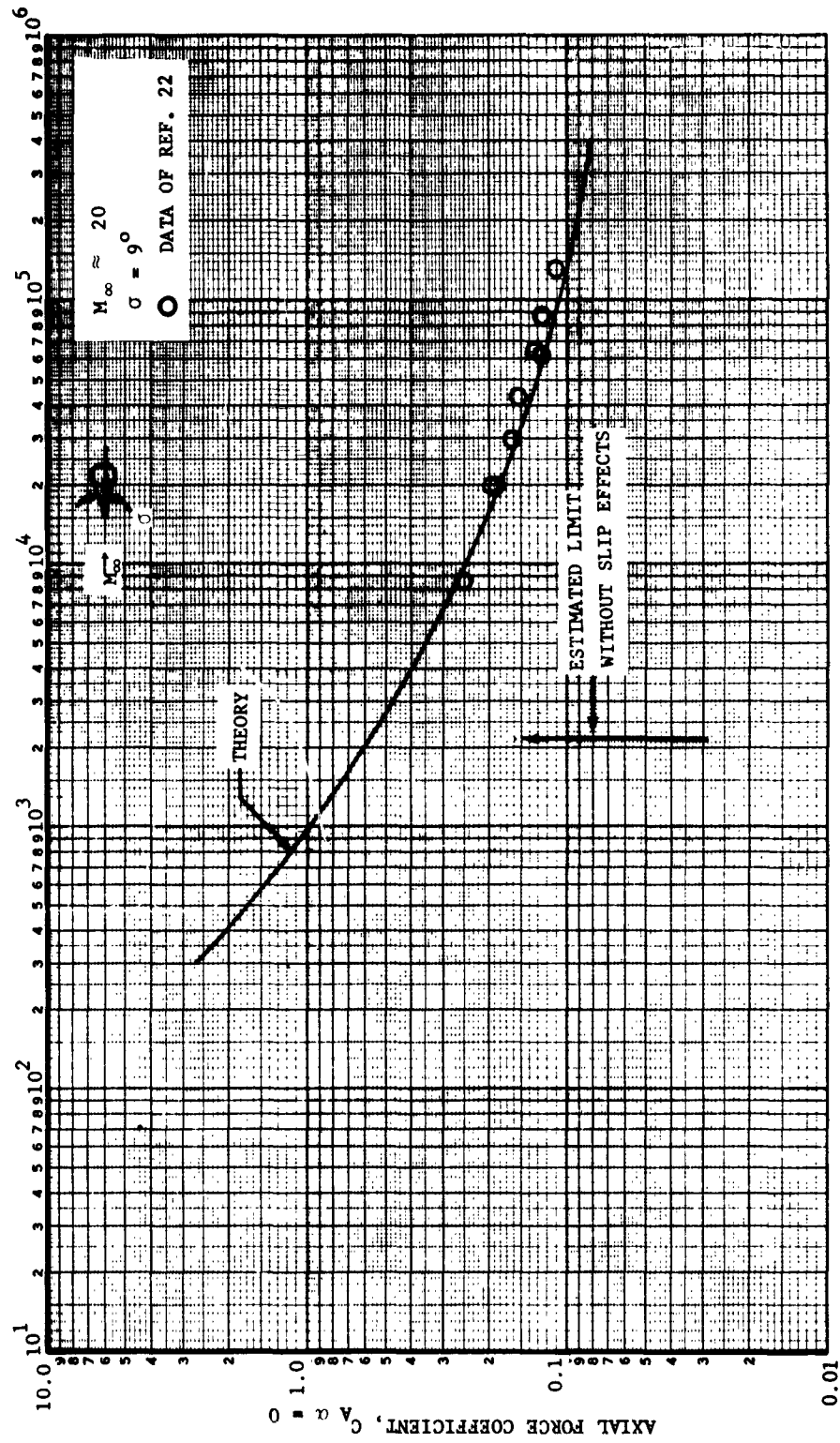


FIGURE 4-8. COMPARISON OF THEORY AND EXPERIMENT FOR AXIAL FORCE COEFFICIENT

REYNOLDS NUMBER, Re_D

S120C6

Before concluding this discussion of interaction theory, one final point of interest remains. In the case of using the square root of the ratio of the interaction pressure to the inviscid pressure to obtain the total skin friction in the presence of boundary-layer-shock-wave-interaction:

$$\frac{C_{f_i}}{C_c} = \sqrt{\frac{P_i}{P}} ,$$

where the subscript i refers to the case with interaction.

Bertram has shown that this approach gives very good results in the case of a flat plate.

Applying this procedure to the case of a cold wall cone at high Mach numbers, and letting Equation 2.22 represent the pressure ratio:

$$\frac{C_{f_i}}{C_f} = \sqrt{1 + F_c \bar{\chi}_c} \quad 4.12$$

which for small values of $\bar{\chi}_c$ is approximately

$$\frac{C_{f_i}}{C_f} = 1 + \frac{1}{2} F_c \bar{\chi}_c \quad 4.13$$

For these same conditions Probstein's theory gives:

$$\frac{C_{f_i}}{C_f} = 1 + \left(0.528 - \frac{0.126}{\gamma}\right) F_c \bar{\chi}_c \quad 4.14$$

Assuming a $\gamma = 1.4$ there is approximately a 12 percent difference in the $\bar{\chi}$ term between Equations 4.13 and 4.14.

Ford Motor Company.
AERONAUTRONIC DIVISION

Experimental drag data for a 9° cone obtained under various test conditions are shown in Figure 4-9. Also shown in this figure are appropriate drag curve segments calculated by means of the interaction theory. It is apparent that reasonable agreement exists between the calculated curves and the test points at the higher Reynolds numbers. However, at the lowest Reynolds numbers tested, the disagreement is substantial. With the limited test data available, presented in this form, it is not possible to establish precisely where the theory and the test data begin to diverge.

Trends similar to those previously stated are observed for a 6.33° cone, as shown in Figure 4-10.

Interpretation of the various trends shown in Figures 4-9 and 4-10 will be left to a later section. The principal point to be made here is that within the region of applicability, the interaction theory gives reliable results.

It should be noted that the NOL data presented in Figure 4-10 are of a reduced order of accuracy. These data were obtained in a ballistic range facility where, due to the low density conditions under which the test was run, it was not possible to prevent the model from undergoing a sustained pitching oscillation as it traversed the range. Therefore, the actual measured drag of the model included some angle of attack effects. The data presented in Figure 4-10 represent the measured data reduced to zero angle of attack conditions by means of an extrapolation technique. Because of the inherent uncertainties of this procedure, the disagreement between the NOL data and the theory shown in Figure 4-9 is not considered significant.

A substantial part of the experimental data shown in Figures 4-9 and 4-10 have been obtained from unpublished sources. Since this information is not generally available, a brief summary of the principal conditions and results for these tests is given in Table II.

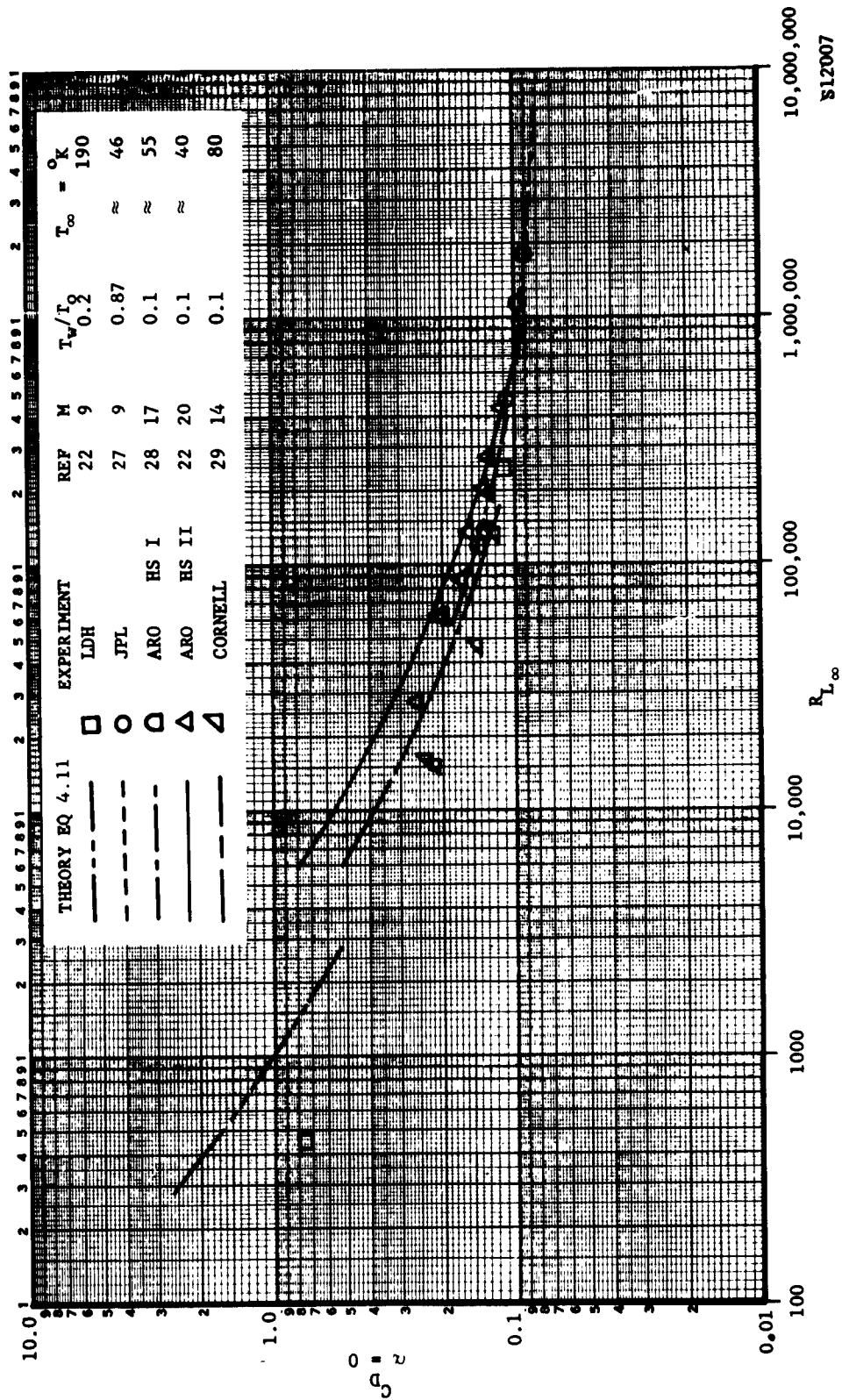


FIGURE 4-9. COMPARISON BETWEEN EXPERIMENT AND THEORY 9° CONE

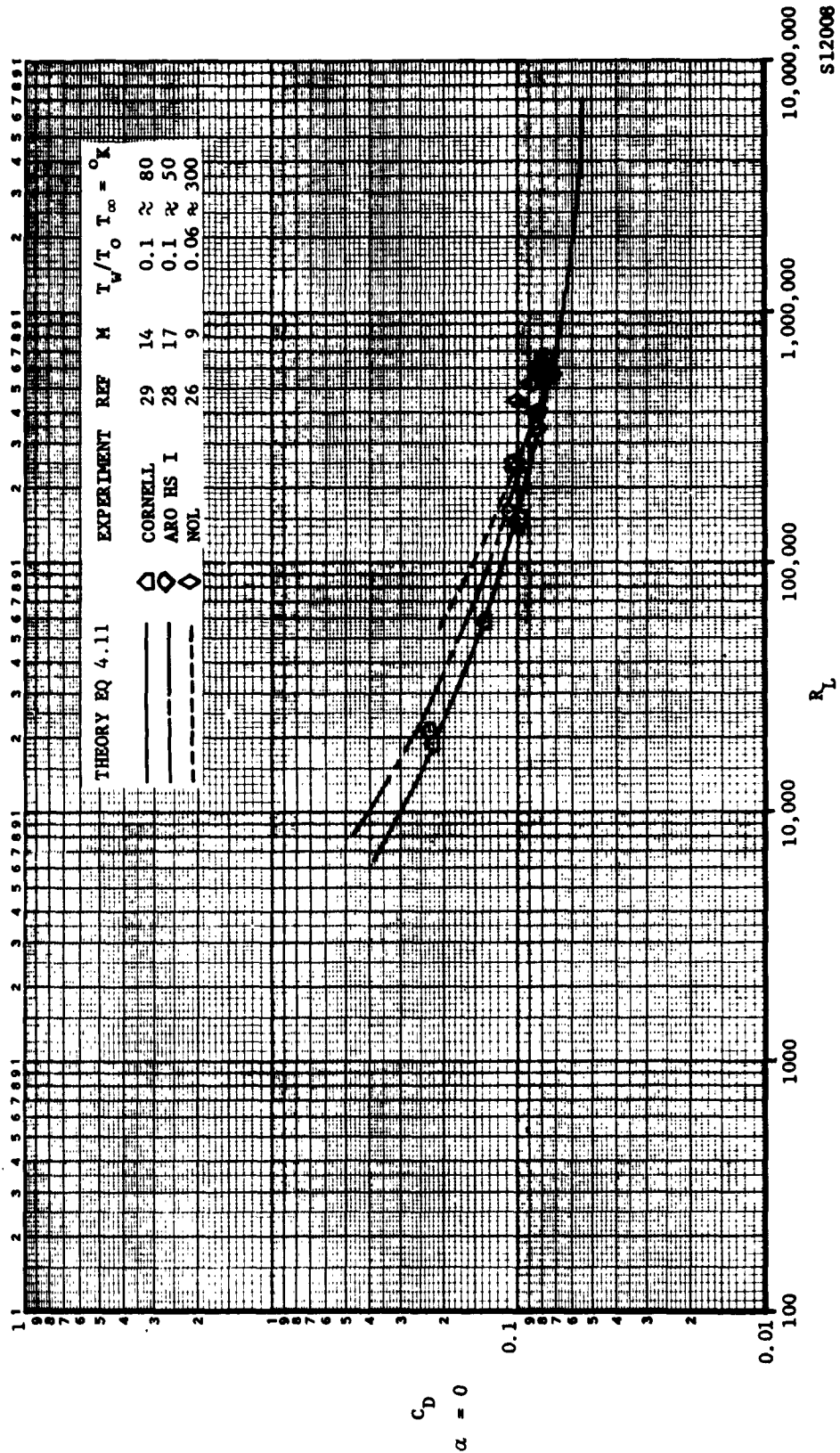


FIGURE 4-10. COMPARISON BETWEEN EXPERIMENT AND THEORY 6.3° CONE

TABLE II
UNPUBLISHED TEST RESULTS

| Test | Refer- ence | Config cone Semi-apex angle | T_w/T_o | $T_\infty(^{\circ}\text{K})$ | M_∞ | R_{L_∞} | C_D |
|---|----------------|-----------------------------------|-----------|--|------------|----------------|--------|
| Aeronutronic Test PA-1 NOL Ballistic Range | 26 | 6.3° | 0.06 | 300° | 9.001 | 667,000 | 0.079 |
| | | | | | 8.2 | 605,000 | 0.0815 |
| | | | | | 9.16 | 527,000 | 0.089 |
| | | | | | 9.037 | 579,000 | 0.0817 |
| | | | | | 9.336 | 439,000 | 0.100 |
| | | | | | 9.038 | 413,000 | 0.0862 |
| | | | | | 9.198 | 255,000 | 0.103 |
| Aeronutronic Test PA-4 Arnold Center Hotshot I | 28 | 9° | 0.1 | 65.8° 53.1° 51.4° 59.8° 54.3° 53.5° 54.2° 48.9° | 17.36 | 247,000 | 0.112 |
| | | | | | 16.12 | 395,400 | 0.110 |
| | | | | | 17.38 | 122,400 | 0.143 |
| | | | | | 17.22 | 143,800 | 0.134 |
| | | | | | 17.20 | 161,000 | 0.109 |
| | | | | | 16.18 | 572,000 | 0.072 |
| | | | | | 17.42 | 338,700 | 0.084 |
| Aeronutronic Test PA-7 Cornell | 29 | 9° | 0.1 | 72.3 90.5 90.0 78.0 80.2 81.0 83.0 77.3 88.8 | 14.86 | 137,000 | 0.1228 |
| | | | | | 13.63 | 15,600 | 0.2196 |
| | | | | | 13.64 | 16,300 | 0.2360 |
| | | | | | 14.36 | 48,400 | 0.1482 |
| | | | | | 14.66 | 153,000 | 0.098 |
| | | | | | 14.64 | 150,000 | 0.103 |
| | | | | | 13.79 | 21,400 | 0.232 |
| | | 6.3° | 0.1 | | 14.36 | 59,600 | 0.141 |
| | | | | | 13.65 | 19,600 | 0.222 |

CHAPTER 5

APPROXIMATE INTERACTION THEORY AND EXPERIMENTAL CORRELATION

5.1 APPROXIMATE INTERACTION THEORY

While the complete interaction theory discussed in the Section's II, III, and IV indicates agreement with experimental data it is somewhat cumbersome in practice. The present section develops an approximate form of the interaction theory which permits the rapid calculation of cone drag characteristics at hypersonic speeds. This simplified form of the interaction equation also provides the basis for a correlating procedure which unifies the experimental drag data into a single curve.

In the derivation which follows, it has been found convenient to express the flow properties in terms of the free stream Mach number and Reynolds number rather than the conditions behind the shock. This procedure introduces certain restrictions to be noted subsequently. However, it does facilitate the direct comparison of the drag of various cone configurations.

The leading assumption is that the free stream Mach number is hypersonic, i.e., $M_\infty \gg 1$.

From the definition of \bar{X} it follows immediately that:

$$\frac{\bar{X}_\infty}{\bar{X}_c} = \left(\frac{M_\infty}{M_c} \right)^3 \left[\frac{C_\infty}{C_c} \frac{(R_x)_c}{(R_x)_\infty} \right]^{1/2} \quad 5.1$$

For convenience, we also define, $F_c \equiv F' \frac{M_\infty}{M_c}$ dc.

Ford Motor Company

AERONAUTRONIC DIVISION

Assuming the linear viscosity temperature law and a slender body, the following relations apply:

$$\frac{C_{\infty}}{C_c} \approx \left(\frac{T_{\infty}}{T_c} \right)^{1/4} \approx \left(\frac{M_c}{M_{\infty}} \right)^{1/2}$$

$$\frac{\left(\frac{R_x}{R_x} \right)_c}{\left(\frac{R_x}{R_x} \right)_{\infty}} \approx \frac{P_c}{P_{\infty}} \left(\frac{M_c}{M_{\infty}} \right)^{7/2}$$

Substituting these relations into equation 5.1 we obtain:

$$\bar{\chi}_c = \frac{M_c}{M_{\infty}} \left(\frac{P_{\infty}}{P_c} \right)^{1/2} \bar{\chi}_{\infty} \quad 5.2$$

With this expression for $\bar{\chi}_c$, the cone pressure drag (including vacuum base drag) becomes:

$$C_{D_P} = \frac{2}{\gamma M_{\infty}^2} \frac{P_c}{P_{\infty}} \left[1 + \frac{4}{3} F' \left(\frac{P_{\infty}}{P_c} \right)^{1/2} d_c \bar{\chi}_{\infty} \right] \quad 5.3$$

For large Mach numbers $K \gg 1$ and

$$K_S \approx \frac{2(\gamma+1)K}{\gamma+3}$$

$$\text{Hence } \frac{P_c}{P_{\infty}} \approx 8 \gamma \frac{(\gamma+1)}{(\gamma+3)^2} K^2 \quad 5.4$$

The coefficient F' is:

$$F' = \frac{1}{\sqrt{3}} \frac{1}{P/P_{\infty}} \left[\frac{1}{M_{\infty}} \frac{d(P/P_{\infty})}{d\theta} \right]_{\theta = \theta_c}$$

For $K \gg 1$, it can be shown that:

$$\left[\frac{1}{M_{\infty}} \frac{d(P/P_{\infty})}{d\theta} \right]_{\theta = \theta_c} \approx \frac{16 \gamma (\gamma+1) K}{(\gamma+3)^2}$$

Ford Motor Company,
AERONUTRONIC DIVISION

Therefore F' may be approximated as:

$$F' \approx \frac{2}{\sqrt{3}} \frac{1}{K} \quad 5.5$$

Expressing the cone angle θ in terms of the body length to diameter ratio ($\cot \theta = 2 \ell/D$) and assuming a slender body, Equations 5.4 and 5.5 can be rewritten:

$$\frac{P_c}{P_\infty} = 2 \gamma \frac{\gamma+1}{(\gamma+3)^2} \frac{M_\infty^2}{(\ell/D)^2} \quad 5.6$$

$$F' = \frac{4}{\sqrt{3}} \frac{\ell/D}{M_\infty} \quad 5.7$$

Substituting these relations into Equation 5.3 for the cone pressure drag, we obtain:

$$C_{DP} = \frac{\gamma+1}{(\gamma+3)^2} \frac{4}{(\ell/D)^2} + \frac{32}{3} \sqrt{\frac{2}{3}} \sqrt{\frac{\gamma+1}{\gamma}} \frac{d_c}{\gamma+3} \sqrt{C_\infty} \frac{M_\infty}{\sqrt{(R_L)_\infty}} \quad 5.8$$

The above equation contains the viscosity proportionality constant C_∞ based on the free stream conditions. From the power law:

$$C_\infty = \left(\frac{T_\infty}{T_{ref}} \right)^{1/4}$$

The ratio T_{ref}/T_∞ may be evaluated by Eckert's reference enthalpy method.

Approximating:

$$\left(\frac{T_w}{T_\infty} + 1 \right) \text{ by } \frac{T_w}{T_\infty}, \quad \left(1 + \frac{\gamma-1}{2} M_\infty^2 \right) \text{ by } \frac{\gamma-1}{2} M_\infty^2$$

and expressing the body wall temperature in terms of the stagnation temperature, Eckert's reference enthalpy method gives:

$$\frac{T_{ref}}{T_\infty} \approx (Pr)^{1/2} \left(\frac{\gamma-1}{2} \right) M_\infty^2 \left(\frac{0.5}{(Pr)^{1/2}} \frac{T_w}{T_0} + 0.22 \right)$$

Ford Motor Company

AERONAUTRONIC DIVISION

For convenience we define:

$$E \equiv (P_r)^{1/2} \left(\frac{\gamma-1}{2}\right) \left(\frac{0.5}{(Pr)^{1/2}} \frac{T_w}{T_0} + 0.22\right) \quad 5.9$$

Thus:

$$C_\infty = \frac{1}{M_\infty^{1/2} (E)^{1/4}} \quad 5.10$$

and the cone pressure drag equation becomes:

$$C_{DP} = \frac{\gamma+1}{(\gamma+3)^2} \frac{4}{(L/D)^2} + \frac{32}{3} \sqrt{\frac{2}{3}} \sqrt{\frac{\gamma+1}{\gamma}} \frac{d_c}{\gamma+3} \left(\frac{1}{E}\right)^{1/8} \frac{M_\infty^{3/4}}{\sqrt{(R_L)_\infty}} \quad 5.11$$

We shall leave the pressure drag term in this form for the time being and proceed with the skin friction drag. It is worth noting, however, that the first term in the above equation is the inviscid pressure contribution, while the second term contains the interaction pressure contribution.

The skin friction drag consists of three terms, considered separately; the Mangler, interaction, and transverse curvature terms. The first term is the Mangler skin friction, the second represents the effect of transverse curvature, while the third represents the effect of the boundary-layer-shock-wave interaction.

Since,

$$\frac{q_c}{q_\infty} = \frac{P_c}{P_\infty} \left(\frac{M_c}{M_\infty} \right)^2$$

the skin friction equation may be written in the form:

$$\begin{aligned} C_{DF} = & 4.33 \sqrt{\gamma} \sqrt{\frac{\gamma+1}{\gamma+3}} \frac{1}{(E)^{1/8}} \frac{M_\infty^{3/4}}{\sqrt{(R_L)_\infty}} \\ & + 6.12 (L/D)^2 \left[\frac{\textcircled{A}}{M_c^2} \right] \left[\frac{1}{(E)^{1/8}} \frac{M_\infty^{3/4}}{\sqrt{(R_L)_\infty}} \right]^2 \\ & + 10.59 (L/D)^2 \left[\frac{\textcircled{B}}{\gamma} d_c \right] \left[\frac{1}{(E)^{1/8}} \frac{M_\infty^{3/4}}{\sqrt{(R_L)_\infty}} \right]^2 \end{aligned} \quad 5.12$$

Ford Motor Company
AERONAUTRONIC DIVISION

where $\textcircled{A} = (0.446 + 0.788 \frac{T_w}{T_c} + 0.105 (\gamma - 1) M_c^2)$

$\textcircled{B} = (0.528 \gamma - 0.126 + \frac{0.733}{M_c^2} \frac{T_w}{T_c} - \frac{1.152}{M_c^2})$

Combining Equation 5.12 for the skin friction with Equation 5.11 for the pressure drag the total drag is

$$C_D = \frac{\gamma+1}{(\gamma+3)^2} \frac{4}{(\ell/D)^2} + \frac{\sqrt{\gamma+1}}{\gamma+3} \left\{ \frac{8.71}{\sqrt{\gamma}} d_c + 4.33\sqrt{\gamma} \right\} \frac{1}{(E)^{1/8}} \frac{M_\infty^{3/4}}{\sqrt{(R_L)_\infty}}$$

$$+ (\ell/D)^2 \left\{ 6.12 \left[\frac{\textcircled{A}}{M_c^2} \right] + 10.59 \left[\frac{\textcircled{B}}{\gamma} d_c \right] \right\} \frac{1}{(E)^{1/8}} \frac{M_\infty^{3/4}}{\sqrt{(R_L)_\infty}} \quad 5.13$$

We now proceed to simplify the terms in the brackets. The term d_c may be rewritten, under the assumption of large Mach number:

$$d_c \approx A(\text{Pr}) \frac{\gamma-1}{2} \frac{T_w}{T_0} + B(\text{Pr}) (\gamma-1)$$

Taking $A(\text{Pr}) = 0.968$ and $B(\text{Pr}) = 0.145$:

$$d_c \approx (\gamma-1) (0.145 + 0.484 \frac{T_w}{T_0})$$

Thus:

$$\left\{ \frac{8.71}{\sqrt{\gamma}} d_c + 4.33\sqrt{\gamma} \right\} = 5.61\sqrt{\gamma} \left[1 + 0.754 \frac{T_w}{T_0} - \frac{0.226}{\gamma} - \frac{0.754}{\gamma} \frac{T_w}{T_0} \right]$$

It is now proposed that the last two terms in the above brackets be numerically evaluated using a value of $\gamma = 1.4$. This gives:

$$\left\{ \frac{8.71}{\sqrt{\gamma}} d_c - 4.33\sqrt{\gamma} \right\} \approx 4.7\sqrt{\gamma} \left[1 + 0.258 \frac{T_w}{T_0} \right] \quad 5.14$$

The above expression is correct for $\gamma = 1.4$, but is somewhat in error for other values of γ . For a $\gamma = 1.67$, and

$$\frac{T_w}{T_0} = 0$$

Ford Motor Company,
AERONUTRONIC DIVISION

there is approximately a 3 percent error in the above expression, while for the conditions $\gamma = 1.67$ and

$$\frac{T_w}{T_0} = 1$$

the error is approximately 10 percent.

The other term to be simplified in Equation 5.13 is:

$$\left\{ 6.12 \left[\frac{\textcircled{A}}{M_c^2} \right] + 10.59 \left[\frac{\textcircled{B}}{\gamma} d_c \right] \right\}$$

Expressing the body wall temperature in terms of the stagnation temperature:

$$\frac{\textcircled{A}}{M_c^2} \approx \frac{0.446}{M_c^2} + 0.394 (\gamma - 1) \frac{T_w}{T_0} + 0.105 (\gamma - 1)$$

At large Mach numbers the first term is negligible,

$$\text{Thus: } \frac{\textcircled{A}}{M_c^2} \approx (\gamma - 1) \left(0.105 + 0.394 \frac{T_w}{T_0} \right) \quad 5.15$$

Following a similar approach for $\frac{\textcircled{B}}{\gamma} d_c$:

$$\frac{\textcircled{B}}{\gamma} d_c \approx (\gamma - 1) \left[0.0766 \left(1 - \frac{0.24}{\gamma} \right) + 0.308 \frac{T_w}{T_0} \left(1 - \frac{0.37}{\gamma} \right) + 0.177 \left(\frac{T_w}{T_0} \right)^2 \left(1 - \frac{1}{\gamma} \right) \right]$$

Substituting the value $\gamma = 1.4$ into the terms within the brackets the above reduces to:

$$\frac{\textcircled{B}}{\gamma} d_c \approx (\gamma - 1) \left[0.0635 + 0.227 \frac{T_w}{T_0} + 0.0505 \left(\frac{T_w}{T_0} \right)^2 \right] \quad 5.16$$

Ford Motor Company
AERONUTRONIC DIVISION

For a $\gamma = 1.67$ and $\frac{T_w}{T_0} = 0$ the error in the above expression is ≈ 3.5 percent. If $\gamma = 1.67$,

$$\frac{T_w}{T_0} = 1 \text{ the error is approximately 12 percent.}$$

Making use of the approximate relations of Equations 5.15 and 5.16, the result is obtained:

$$\left\{ 6.12 \frac{\textcircled{A}}{M_c^2} + 10.59 \frac{\textcircled{B}}{\gamma} d_c \right\} \approx (\gamma - 1) \left[1.313 + 4.81 \frac{T_w}{T_0} + 0.534 \left(\frac{T_w}{T_0} \right)^2 \right] \quad 5.17$$

For most cases of practical interest (i.e., atmospheric re-entry of a flight vehicle) the temperature ratio

$$\frac{T_w}{T_0}$$

is quite small. Even for an adiabatic wall

$$\left(\frac{T_w}{T_0} \right)^2 \approx 0.72,$$

and since the last term in the brackets above is only 8 percent of the previous term this last term will be neglected.

The total drag for the cone is now expressed as:

$$C_D = \frac{\gamma+1}{(\gamma+3)^2} \frac{4}{(\ell/D)^2} + 4.7 \frac{\sqrt{\gamma+1}}{\gamma+3} \sqrt{\gamma} \left(1 + 0.258 \frac{T_w}{T_0} \right) \cdot \frac{1}{(E)^{1/8}} \frac{M_\infty^{3/4}}{\sqrt{(R_L)_\infty}} + 1.313 (\ell/D)^2 (\gamma-1) \left(1 + 3.67 \frac{T_w}{T_0} \right) \left(\frac{1}{(E)^{1/8}} \frac{M_\infty^{3/4}}{\sqrt{(R_L)_\infty}} \right)^2 \quad 5.18$$

Substituting the relation for E as given in Equation 5.9 and assuming a Prandtl number of 0.72 the final form of the drag equation is:

$$C_D = \frac{\gamma+1}{(\gamma+3)^2} \frac{4}{(\ell/D)^2} + 6.32 \frac{\sqrt{\gamma+1}}{(\gamma+3)} \sqrt{\gamma} \frac{(1 + 0.258 \frac{T_w}{T_0})}{[(\gamma-1)(1 + 2.64 \frac{T_w}{T_0})]^{1/8}} \cdot \frac{M_\infty^{3/4}}{\sqrt{(R_L)_\infty}} + 2.37 (\ell/D)^2 (\gamma-1) \frac{(1 + 3.67 \frac{T_w}{T_0})}{[(\gamma-1)(1 + 2.64 \frac{T_w}{T_0})]^{1/4}} \left(\frac{M_\infty^{3/4}}{(R_L)_\infty} \right)^2 \quad 5.19$$

which can also be written in the form:

$$C_D = \frac{a_1}{(\ell/D)^2} + a_2 \frac{M_\infty^{3/4}}{\sqrt{(R_L)_\infty}} + a_3 (\ell/D)^2 \left(\frac{M_\infty^{3/4}}{\sqrt{(R_L)_\infty}} \right)^2 \quad 5.20$$

where,

$$a_1 = 4 \frac{(\gamma+1)}{(\gamma+3)^2}$$

$$a_2 = 6.32 \frac{\sqrt{\gamma+1}}{(\gamma+3)} \frac{\sqrt{\gamma}}{(\gamma-1)^{1/8}} \frac{(1 + 0.258 \frac{T_w}{T_0})}{(1 + 2.64 \frac{T_w}{T_0})^{1/8}}$$

$$a_3 = 2.37 (\gamma-1)^{3/4} \frac{(1 + 3.67 \frac{T_w}{T_0})}{(1 + 2.64 \frac{T_w}{T_0})^{1/4}}$$

Equation 5.20 is useful in making quick preliminary drag variation estimates for re-entry trajectory studies. For example, assuming a $\gamma = 1.4$ and

$$\frac{T_w}{T_0} = 0.1,$$

the general formula for all cone drags ($M_\infty \theta_c \gg 1$; $M > 10$; $\theta_c < 24^\circ$) is:

$$C_D = \frac{0.496}{(\ell/D)^2} + 2.88 \frac{M_\infty^{3/4}}{\sqrt{(R_L)_\infty}} + 1.53 (\ell/D)^2 \left(\frac{M_\infty^{3/4}}{\sqrt{(R_L)_\infty}} \right)^2 \quad 5.21$$

Note that the inviscid pressure drag term above (i.e., $\frac{0.496}{(\ell/D)^2}$) is very nearly that given by Newtonian theory (i.e.,

$$\frac{0.5}{(\ell/D)^2}$$

The principal limitation to the general validity of Equation 5.20, aside from the approximations discussed in the text, is associated with the use of the power law variation of viscosity with temperature.

For very high stagnation temperatures or very low free-stream temperatures (such as those obtained in wind tunnel testing at high Mach numbers) the power law variation in the form used in the previous derivation can be considerably in error. The simplified form of the drag equation can still be applied with considerable success if a suitable transformation in the effective Reynolds number is made. This transformation will be discussed further in Section 5.3 on Correlation of Experimental Data and consists of the replacement of the Reynolds number $(R_L)_\infty$ in Equation 5.20 by a pseudo or effective Reynolds number $(R_L)_\infty^{\text{effective}}$ for the purposes of the drag calculation. To anticipate the results of Section 5.3, Equation 5.33 has been utilized to determine the "effective" Reynolds number and a calculation has been made using the simplest form of the approximate drag equation (Equation 5.21) applied to the test conditions of Reference 22.

A comparison between this calculation and the experimental data points is shown in Figure 5-1. It is apparent that the approximate theory gives very good results at this high Mach number. However, since the theory is based on hypersonic approximations, the agreement would be less favorable at lower Mach numbers.

Finally, it must be remembered that interaction theory, whether exact or approximate, is no longer applicable at a very low Reynolds number.

5.2 DERIVATION OF CORRELATION PARAMETERS FOR CONE DRAG

In this section a set of parameters are obtained for correlating the drag of slender cones at supersonic and hypersonic speeds.

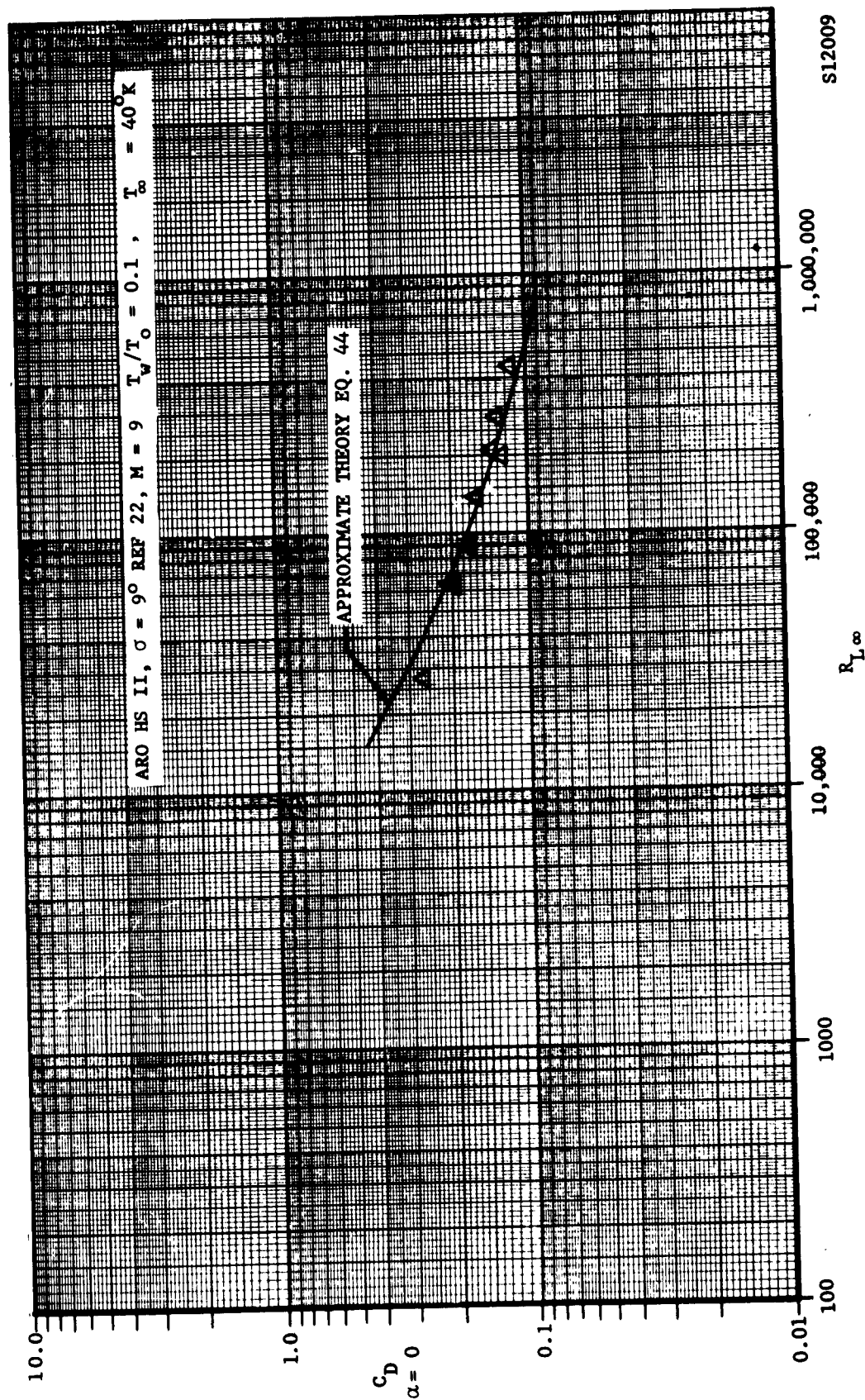


FIGURE 5-1. COMPARISON BETWEEN EXPERIMENT AND APPROXIMATE THEORY

Ford Motor Company

AERONAUTRONIC DIVISION

It will be shown that through the use of these parameters, experimental data for a wide range of Mach and Reynolds numbers can be unified into a single curve. This correlation curve shows agreement with interaction theory at the higher Reynolds numbers. However, at very low Reynolds numbers, significant deviations from interaction theory are observed. This is to be expected since it is well known that as the flow density decreases continuum flow concepts become invalid and must be replaced by those appropriate to free molecule flow. It is also recognized that a transition regime must exist between the continuum and free molecule regimes.

The principal advantage of the present correlation procedure is that it permits the consolidation of the limited available low density test data in such a way as to obtain useful trend information in the transition regime. Such information is particularly useful because, at the present time, there is no well established theory for this transition regime.

The correlation parameters to be discussed here are based on the simplified form of the cone drag equation (e.g. Equation 5-20 of Section 5.1).

It is observed that the cone drag variation indicated in this Equation is characterized by three different regimes. These regimes are related to the numerical magnitude of the ratio $M_{\infty}^{3/4}$.

$$\sqrt{(R_L)_{\infty}}$$

For small values of the above ratio, the second and third terms of the drag equation are negligible compared to the first term, therefore, the cone drag is simply the inviscid pressure drag. For intermediate values of the ratio, the cone drag varies as a function of the parameter $M_{\infty}^{3/4}$, while for large

$$\sqrt{(R_L)_{\infty}}$$

values of the ratio, the drag varies as a function of $\frac{M_{\infty}^{3/2}}{R_{L\infty}}$.

There is no difficulty in obtaining cone inviscid pressure drag by standard methods. Since we are interested principally in the rarified flow regimes where viscous effects are important, it is convenient to eliminate the cone pressure drag from the correlation process. This is done by rewriting Equation 5.20 in the form:

$$C_D - C_{D_P} = a_2 \frac{M_\infty^{3/4}}{\sqrt{(R_L)_\infty}} + a_3 \left(\ell/D \right)^2 \left(\frac{M_\infty^{3/4}}{\sqrt{(R_L)_\infty}} \right)^2 \quad 5.22$$

From the above equation it is obvious that we could plot $C_D - C_{D_P}$ vs $a_2 \frac{M_\infty^{3/4}}{\sqrt{(R_L)_\infty}}$ and obtain a general correlation for small to moderate values of $\frac{M_\infty^{3/4}}{\sqrt{(R_L)_\infty}}$, however, there would remain a divergence at larger

values of this ratio. The problem is to extend the range of correlation. This can be done at the expense of a more complex correlation parameter.

By restricting γ to a value of 1.4 and evaluating the coefficients a_2 and a_3 for various values of T_w/T_0 , it is found that a_2 can be approximated as $a_2 \approx 2.82 \left[1 + .04 \frac{T_w}{T_0} \right]$ and $a_3 \approx 1.12 \left[1 + 2.4 \frac{T_w}{T_0} \right]$.

Substituting these values into Equation 5.22 and neglecting the temperature contribution in a_2 we have:

$$C_D - C_{D_P} = 2.82 \frac{M_\infty^{3/4}}{\sqrt{(R_L)_\infty}} + 1.12 \left[1 + 2.4 \frac{T_w}{T_0} \right] \left(\ell/D \right)^2 \left(\frac{M_\infty^{3/4}}{\sqrt{(R_L)_\infty}} \right)^2 \quad 5.23$$

This suggests a correlation parameter of the form:

$$X = \frac{M_\infty^{3/4}}{\sqrt{(R_L)_\infty}} \left[1 + a (\ell/D)^2 \left(1 + b \frac{T_w}{T_0} \frac{M_\infty^{3/4}}{\sqrt{(R_L)_\infty}} \right) \right] \quad 5.24$$

where $a \approx 0.4$

$b \approx 2.4$

This is equivalent to:

$$\frac{P_c}{P_\infty} \approx c_p \frac{\gamma M_\infty^2}{2} \quad 5.25$$

where c_p , the pressure coefficient, is:

$$c_p = \frac{\gamma+1}{(\gamma+3)^2} \frac{4}{(\ell/D)^2} \approx 2 \sin^2 \theta_c$$

The above representation of the cone pressure is accurate for very high Mach numbers; however, at lower Mach numbers the expression should be:

$$\frac{P_c}{P_\infty} = c_p \frac{\gamma M_\infty^2}{2} + 1 \quad 5.26$$

According to the complete interaction theory, as previously given, the ratio $\frac{P_c}{P_\infty}$ appears directly in the expression for the cone pressure drag (Section 2) and indirectly in the expression for the skin friction (Section 4).

In the correlation procedure being used here, the inviscid pressure drag is subtracted from the total drag at the outset; therefore, assuming this inviscid pressure drag is correctly evaluated from Kopal tables or similar reference, the pressure approximation expressed by Equation 5.25 does not influence this part of the correlation.

Ford Motor Company,

AERONUTRONIC DIVISION

Of the remaining terms associated with viscous effects, the largest contribution is that due to skin friction. From Equation 4.6 it is seen that the principal coefficient of the skin friction equation is:

$$\cot \theta = \frac{q_c}{q_\infty} \sqrt{\frac{C_c}{(R_L)_c}}$$

since

$$\cot \theta = 2 \ell / D$$

$$\frac{q_c}{q_\infty} \approx \frac{p_c}{p_\infty} \left(\frac{M_c}{M_\infty} \right)^2$$

$$\frac{C_c}{C_\infty} \approx \left(\frac{M_c}{M_\infty} \right)^{1/2}$$

Due to the number of approximations involved, it is not expected that anything more than the form of the correlation parameter X is given by the above relation. In particular, the constants a and b are subject to adjustment.

It is interesting to note that for a moderate degree of flow

rarification the appropriate correlating parameter is $\frac{M_\infty^{3/4}}{\sqrt{(R_L)_\infty}}$, rather

than the usually accepted $\frac{M}{\sqrt{(R_L)_\infty}}$. The parameters are very similar,

however, and at the lower Mach numbers the difference between M and $M^{3/4}$ is small; hence $\frac{M}{\sqrt{(R_L)_\infty}}$ will provide a fair correlation.

At this point we return to the complete interaction theory as given in Chapter 2-4. If the parameter X is to correlate experimental data, it should also correlate points calculated by the complete interaction theory. This is certainly true for the intermediate density range

where the theory is known to agree with experimental data. It is also taken to be a requirement in the low density regime for lack of a better criterion.

Figure 5-2 shows the correlation obtained for theoretically calculated drag curves assuming various combinations of free stream Mach number, wall temperature, and cone angle. The correlation parameter X, as shown in this figure, is slightly different in form from that given in Equation 5.24. Aside from the numerical values found to be most suitable for the constants a and b (a = 0.5, b = 2.5) the term

$\left[1 + \frac{(l/D)^2}{\gamma M_\infty^2} \right]$ has been added to the correlation parameter. This term was

found necessary to obtain agreement at the lower Mach numbers ($M < 15$). It is basically a correction to the skin friction contribution to account for certain pressure effects that were over-simplified by the approximations used in the derivation of Equation 5.20. The reasoning behind this correction factor is discussed in the following text.

It will be recalled that in the derivation of Equation 5.20, the free stream Mach number was assumed hypersonic so that the inviscid pressure on the cone could be represented as:

$$\frac{P_c}{P_\infty} \approx 2\gamma \frac{\gamma + 1}{(\gamma + 3)^2} \frac{M_\infty^2}{(l/D)^2}$$

we can write

$$\cot \theta \frac{q_c}{q_\infty} \sqrt{\frac{C_c}{(R_L)_c}} \approx 2 l/D \left(\frac{P_c}{P_\infty} \right)^{1/2} \sqrt{C_\infty}$$

Using the hypersonic approximation for $\frac{P_c}{P_\infty}$, as given by Equation 5.25

we have:

$$\cot \theta \frac{q_c}{q_\infty} \sqrt{\frac{C_c}{(R_L)_c}} \approx 2 l/D \left(c_p \frac{\gamma M_\infty^2}{2} \right)^{1/2} \sqrt{C_\infty} \quad 5.27$$

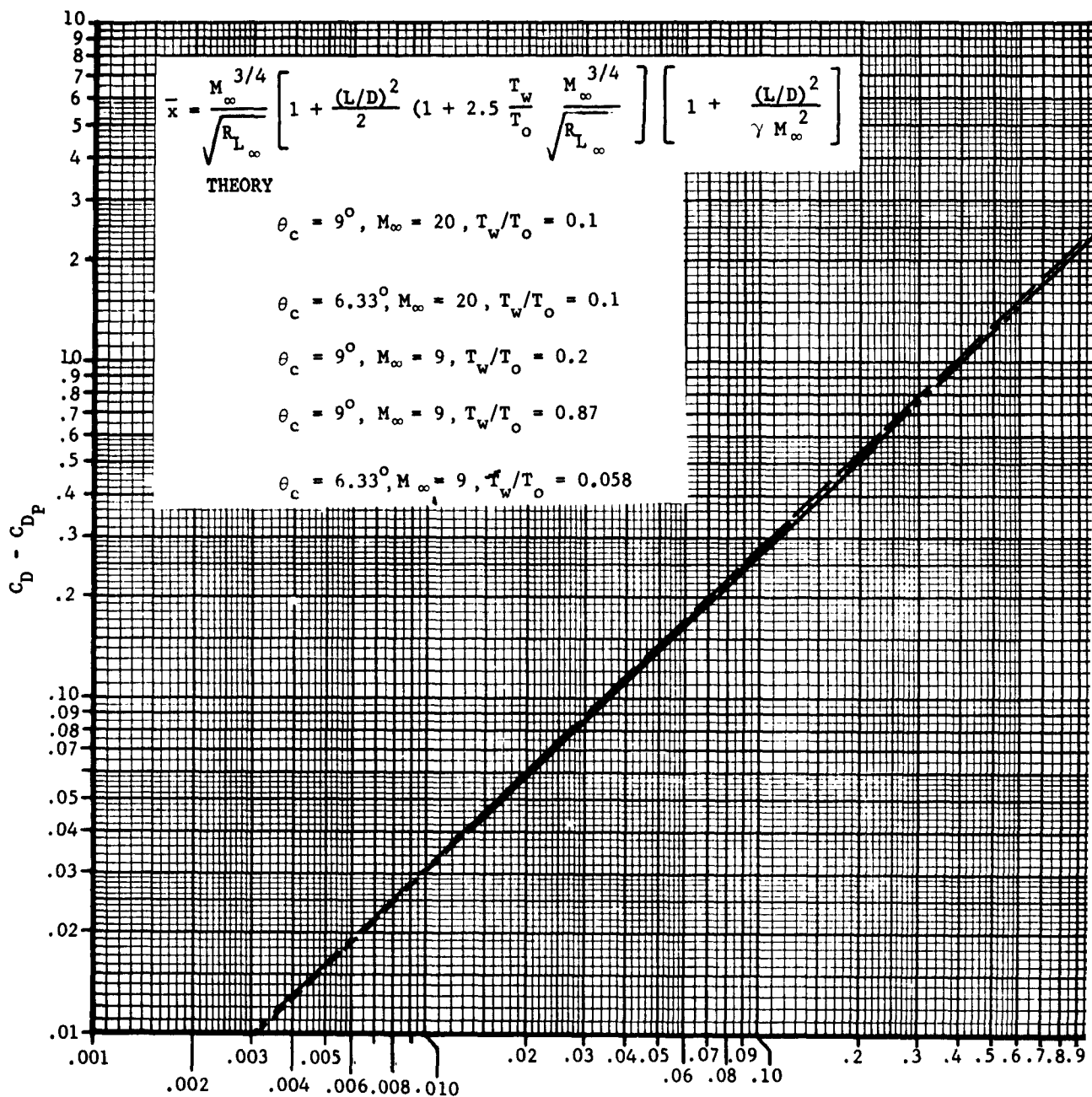


FIGURE 5-2. CORRELATION OF THEORETICALLY CALCULATED DRAG CURVES

S12010

If, on the other hand, we use the more accurate Equation 5.26 to represent the pressure ratio, we have:

$$\cot \theta \frac{q_c}{q_\infty} \sqrt{\frac{C_c}{(R_L)_c}} \approx 2 \ell/D \left(c_p \frac{\gamma M_\infty^2}{2} \right)^{1/2} \cdot \left[1 + \frac{1}{c_p \frac{\gamma M_\infty^2}{2}} \right]^{1/2} \sqrt{C_\infty} \quad 5.28$$

It is apparent that Equation 5.28 is identical to Equation 5.27 except for the correction factor

$$\left[1 + \frac{1}{c_p \frac{\gamma M_\infty^2}{2}} \right]^{1/2}$$

Since $\frac{1}{c_p \frac{\gamma M_\infty^2}{2}}$ is generally small compared to 1, the correction factor can be further approximated:

$$\left[1 + \frac{1}{c_p \frac{\gamma M_\infty^2}{2}} \right]^{1/2} \approx 1 + \frac{1/2}{c_p \frac{\gamma M_\infty^2}{2}} + \dots$$

or expressing C_p as $2 \sin^2 \theta \approx \frac{1}{2 (\ell/D)^2}$

$$\left[1 + \frac{1}{c_p \frac{\gamma M_\infty^2}{2}} \right]^{1/2} \approx 1 + \frac{2 (\ell/D)^2}{\gamma M_\infty^2} + \dots \quad 5.29$$

This is the form of the correction factor that must be applied to the correction parameter X to account for the pressure effects on skin friction.

It was found in the process of correlating the theoretically calculated drag curves, that best agreement was obtained when the constant 2 was dropped from the correction factor. This is probably due to additional implicit approximations which have not been directly accounted for. (The assumption of a constant value for the coefficient F; for example.) In final form the correlation parameter is:

$$X = \frac{M_{\infty}^{3/4}}{\sqrt{(R_{L\infty})}} \left[1 + \frac{(\ell/D)^2}{2} \left(1 + 2.5 \frac{T_w}{T_0} \right) \frac{M_{\infty}^{3/4}}{(R_{L\infty})} \right] \left[1 + \frac{(\ell/D)^2}{\gamma M_{\infty}^2} \right] \quad 5.30$$

It is apparent from Figure 5-2 that good correlation is obtained between the various theoretically calculated drag curves.

We now proceed to the correlation of experimental data.

5.3 CORRELATION OF EXPERIMENTAL DATA

Most of the available hypersonic experimental test data have been obtained at very low freestream temperatures (i.e., 50° to 100°K). This requires that some caution be exercised in use of the correlation parameter X as defined in the previous section.

The problem is centered about the fact that the viscous drag of a cone is a function of local conditions behind the shock while the correlation parameter X is based on conditions in front of the shock. In the derivation of X, the approximate equation,

$$\frac{(R_x)_c}{(R_x)_{\infty}} \approx \frac{P_c}{P_{\infty}} \left(\frac{M_c}{M_{\infty}} \right)^{1/2} \quad 5.31$$

was used to express the Reynolds number transformation across the shock. This equation is based on the power law temperature-viscosity relationship ($\omega = 3/4$) and assumes that the Reynolds number ratio is independent of the freestream temperature. This is not strictly true, particularly at the lower freestream temperatures. A more accurate representation of the Reynolds number ratio across the shock is given by the equation (based on the Southerland relation):

$$\frac{(R_x)_c}{(R_x)_\infty} = \frac{P_c}{P_\infty} \frac{M_c}{M_\infty} \frac{T_\infty}{T_c} \left[\frac{1 + \frac{110^\circ K}{T_\infty} \frac{T_\infty}{T_c}}{1 + \frac{110^\circ K}{T_\infty}} \right] \quad 5.32$$

According to this latter representation, a given viscous drag level (which corresponds to a fixed unit Reynolds number behind the shock) occurs at different values of the freestream unit Reynolds number as the freestream temperature is changed.

Alternately, for a fixed freestream Reynolds number, the cone drag varies as a function of freestream temperature.

Because the correlation parameter X is based on the approximate Equation 5.31, this variation with freestream temperature is not accounted for.

It is noted, however, that if an effective freestream Reynolds number is substituted, so that the power law gives the correct downstream conditions, then the correlation parameter X is valid.

The relationship between the effective Reynolds number that must be used for X and the true freestream Reynolds number as measured in a test is:

$$R_\infty \text{ Effective} = R_\infty \text{ Measured} \left(\frac{1 + \frac{110^\circ K}{T_\infty} \frac{T_\infty}{T_c}}{1 + \frac{110^\circ K}{T_\infty}} \right) \left(\frac{T_\infty}{T_c} \right)^{1/4} \quad 5.33$$

It may be observed that as the freestream temperature approaches 0 the above equation reduces to

$$T_\infty \rightarrow 0; \quad \frac{R_{\text{effective}}}{R_{\text{measured}}} \rightarrow \left(\frac{T_\infty}{T_c} \right)^{3/4}$$

while for large freestream temperatures:

$$T_{\infty} \longrightarrow \infty ; \quad \frac{R_{\text{effective}}}{R_{\text{measured}}} \longrightarrow \left(\frac{T_{\infty}}{T_c} \right)^{1/4}$$

Between these two limits there must be a temperature range where

$\frac{R_{\text{effective}}}{R_{\text{measured}}} = 1$. This is the temperature range where the power law

viscosity relationship is accurate. For slender bodies this usually occurs between 200° and 300°K.

The corrected correlation parameter which unites the experimental data is, then:

$$X = \frac{M_{\infty}^{3/4}}{\sqrt{\left| R_{L\text{Eff}} \right|_{\infty}}} \left[1 + \frac{(\ell/D)^2}{2} \left(1 + 2.5 \frac{T_w}{T_0} \right) \sqrt{\frac{M_{\infty}^{3/4}}{\left| R_{L\text{Eff}} \right|_{\infty}}} \right] \left[1 + \frac{(\ell/D)^2}{\gamma M_{\infty}^2} \right] \quad 5.34$$

The last obstacle to be overcome in order to achieve correlation of the experimental data is: The inviscid cone pressure drag level C_{Dp} ,

is different for different cone angles and Mach numbers. Therefore, even assuming that the cones approach a uniform drag level (i.e., $C_D \rightarrow C_{DFM} \approx$

2.0), as the Reynolds number goes to zero, the asymptote of the variable $C_{D_{\text{exp}}} - C_{Dp}$ will lie at different levels, and correlation at the lower

Reynolds numbers will not be obtained. This difficulty can be avoided by using the quantity $(C_D - C_{Dp})/(C_{DFM} - C_{Dp})$ as the ordinate parameter. At

the same time, a modification must be made to the abscissa to retain correlation at high Reynolds numbers. This modification consists of replacing X by X/X_{FM} , where X_{FM} is the value of X at the point where the interaction theory drag curve passes through the free molecule drag level.

In practice this reduces to:

$$X_{FM} = \frac{C_{D\ FM} - C_{D_P}}{2.5} \quad 5.35$$

Figure 5.3 shows the correlation between the experimental drag data obtained for various cones at various Mach numbers, Reynolds numbers, and wall temperature ratios. It is apparent that excellent agreement is obtained between the various test conditions and that a single curve representing the viscous interaction drag can be faired through all the data points. The particular shape of the faired curve represents additional information not presented here. This information is related to sphere drag correlations which will be the subject of a separate memorandum.

With the correlation curve presented here, the drag of a given cone under given conditions can be calculated by evaluating X/X_{FM} for the appropriate values of M , R and T_w/T_0 and reading the corresponding value of

$$\frac{C_D - C_{D_P}}{C_{D_{FM}} - C_{D_P}}$$

The drag calculated in this manner is not restricted to Reynolds number ranges where interaction theory is known to apply. Deviations from interaction theory due to slip flow, etc. are accurately reflected and extrapolations into the transition regime can be made with confidence.

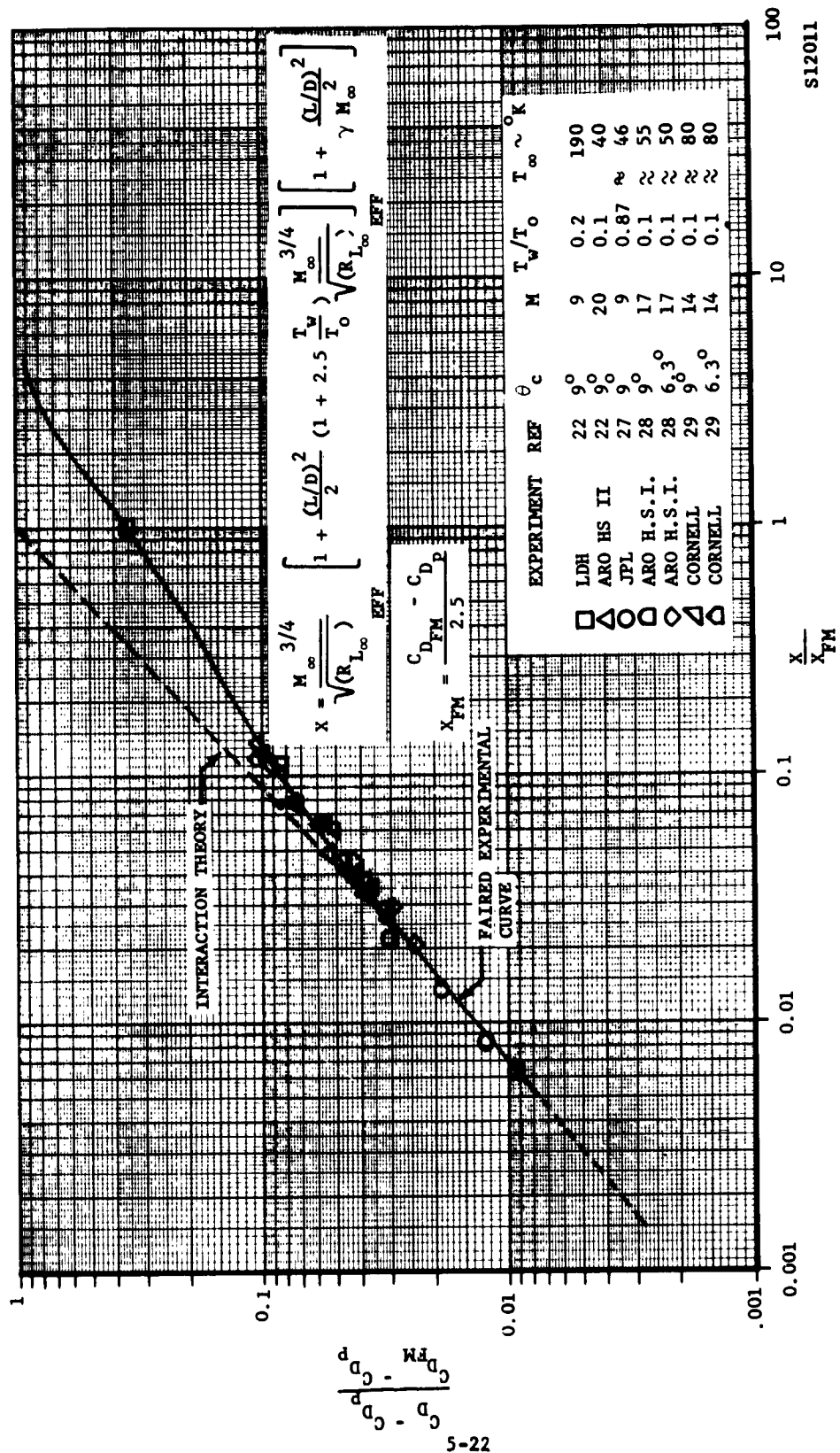


FIGURE 5-3. CORRELATION OF EXPERIMENTAL DATA

S12011

CHAPTER 6

FLOW OVER CONES AT ANGLE OF ATTACK

6.1 GENERAL

The complexity of the three-dimensional flow fields occurring over cones at arbitrary angle of attack is so great that rigorous solutions to the equations of motion have not yet been obtained. This is not a deterrent to many engineering designs since certain restrictive assumptions can be made and solutions obtained for special cases. For example, in hypersonic flow, the assumption of high Reynolds numbers permits an estimate of the aerodynamic forces on bodies by neglecting skin friction effects. The necessity of including the skin friction forces in low-density flows due to boundary layer effects, however, is an added complication which requires considerably more effort to solve. When these boundary layer effects become important, the determination of the flow field must consider not only cross flow and real gas effects, for sufficiently high angle of attack, but also the viscous interaction occurring at the smaller angles of attack. This latter phenomenon causes a local increase in the magnitude of both pressure and skin friction forces as well as displacing the shock wave to perturb the local temperature-density field.

If the freestream density is sufficiently low, the inclusion of the skin friction forces may still be required at high angles of attack, even though any viscous interaction has disappeared due to an effective blunt body flow situation. The determination of the flow field at intermediate angles of attack may be subject to serious errors since the local flow properties must be determined accurately to estimate the magnitude of the low-density flow effects.

The question then naturally arises as to what would be the proper approach in examining the flow field over slender cones at arbitrary angle of attack for current engineering designs is controlled by the following: If primary consideration is given to the aerodynamic forces acting on the body, then a detailed examination of the distribution of local flow variables may not be required. In the present case, primary emphasis will be placed on the estimation of the aerodynamic force coefficients. An attempt will be made to estimate local flow properties from a brief examination of the shock shape insofar as these are used to predict the force coefficients. The general approach will be to examine two limiting cases: (1) the small angle of attack case, where cross flow effects are small or negligible, and (2) the high angle of attack case, where cross flow predominates and any viscous interaction effects are negligible.

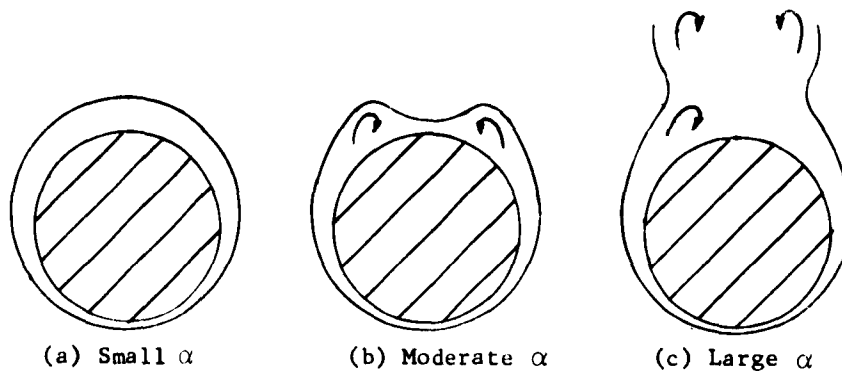
The small angle of attack case may be considered to be a perturbation of the results already presented. It will be shown that the applicability of the predictions extend over a range of angle of attack up to the order of the cone semi-vertex angle. Progressive increases in the angle of attack beyond this point produces increasing error as the cross flow increases. The cone at high angle of attack ($90^\circ \geq \alpha \gg 0$) will be examined by the application of a modified infinite swept cylinder theory. This greatly simplifies the problem since similar solutions are available to the boundary layer equations for swept cylinders, which include variable properties and the inter-dependence of the axial-and-cross-flow. This approach has previously been used in calculating the stagnation line heat transfer on a slender cone¹⁵. In the intermediate angle of attack range, the assumption will be made that a smooth interpolation curve between the limiting cases is adequate. This simple patching procedure will be made by arbitrarily fairing the curve tangent to both calculated portions.

6.2 LAMINAR BOUNDARY LAYER ON A CONE AT ANGLE OF ATTACK.

The laminar boundary layer flow about a circular cone at small angle of attack has been analyzed in the plane of symmetry by several investigators^{15,30,31}. Each points out the difficulty of obtaining solutions away from the stagnation line. Moore³⁰, however, has a discussion on the general behavior of the boundary layer over a cone at angle of attack which is pertinent to the present problem. He shows that the boundary layer tends to be thicker on the top of the cone at angle of attack. Quoting from Moore, "This is to be expected since the fluid near the base of the boundary layer has low inertia, is therefore inclined to follow the direction of the circumferential pressure gradient more closely than in the outer flow, and thus tends to drain away from beneath the cone and accumulate near the top. No separation is encountered because, for small angle of attack, the pressure gradient is always favorable*".

*Approximately for $\alpha < \text{cone half-angle}, \sigma$.

"For larger angles of attack, when the pressure gradient reverses direction near the top of the cone, experiment indicates the formation of boundary-layer 'lobes'. When the angle of attack is further increased the lobe pattern finally breaks away from the body to form a vortex street." This may be illustrated by the following cross-sectional views of the boundary layer on a cone at various angles of attack:



The angle of attack where these different conditions occur may be considerably modified in the present case by the very high Mach numbers and effects of viscous interaction on slender cones. In the limiting case of small angle of attack, a major consideration of the analysis is the determination of what angle of attack does crossflow become non-negligible in estimating the aerodynamic forces. If streamlines are traced over a conical body at angle of attack by following the pressure gradient, the turning angle of the flow (which is a measurement of the crossflow) increases with increasing distance away from the meridian plane of symmetry or stagnation line. A rigorous analysis to determine the magnitude of the crossflow should therefore include the entire surface of the cone. This cannot be accomplished for arbitrary α . A simple estimate of the crossflow magnitude, however, may be made for the present analysis in the following manner:

- (1) A criteria for negligible crossflow is arbitrarily assumed by taking the crossflow velocity gradient at the stagnation line as zero. Solutions are available for this case; at least in the case where the boundary layer is thin and viscous interaction unimportant.

- (2) The analysis will estimate the magnitude of the stagnation line crossflow velocity gradient as a function of freestream Mach number, cone half-angle and α .

We have already confined ourselves to the case of $M_\infty \gg 1$ and slender cones (i.e., $20^\circ > \sigma > 5^\circ$). The validity of the estimate for negligible crossflow will be subsequently determined by comparison with experiment insofar as estimates of aerodynamic force coefficients are concerned. The crossflow velocity gradient, W_ϕ , at the stagnation line has been calculated in the MIT tables³²⁻³⁴ and reproduced in Reference 15 for a range of conditions. These calculations indicate a linear decrease in W_ϕ with increasing Mach number at a given value of α and σ . The examination of 5- and 10-degree half-angle cone values of W_ϕ presented in Reference 15 further indicates that W_ϕ would be very small or negligible for α of the order of or less than σ . This will then be taken as the limiting region of small angle of attack. This region will be treated by assuming negligible crossflow, i.e., assuming the boundary layer grows from the cone vertex as in the case $\alpha = 0$ providing local properties are used at each point in the flow field. The results of the zero angle of attack case may be utilized, assuming that the local shock slopes are independently known. It is to be expected that the increasing error occurring with increasing angle of attack is perhaps not as large or important in the determination of aerodynamic force coefficients where local property variations are integrated out, as in the determination of local heat transfer coefficients which depend directly on local phenomena.

As previously noted, solutions for the other limiting region of large angle of attack will be developed from infinite swept cylinder theory for the slender cones and neglecting the effects of any viscous interaction. Beginning at $\alpha = 90$ degrees, the solution is a two-dimensional blunt body problem. As α is decreased, the contribution of skin friction to the forces becomes more important, at least in the axial direction. The question as to the region of importance of viscous interaction then arises. Calculations have been made of the interaction parameter, $\bar{\chi}_\phi = 0$, for $\sigma = 5$ and 10 degrees and as a function of altitude in Figure 6-1 for $M_\infty = 20$ and $x = 1$ ft. The method for obtaining local shock slope at the stagnation line (and resultant flow properties) will be examined in Section 6.3. Figure 6-1 indicates that for the slender cones of interest fairly definitive limits may be set for the lowest angle of attack at which viscous interaction effects should not appreciably influence the forces. For example, based on the interaction regions already established (criteria here being taken as limiting value of $\bar{\chi} =$ one-tenth of the value of $\bar{\chi}$ for onset of strong interaction),

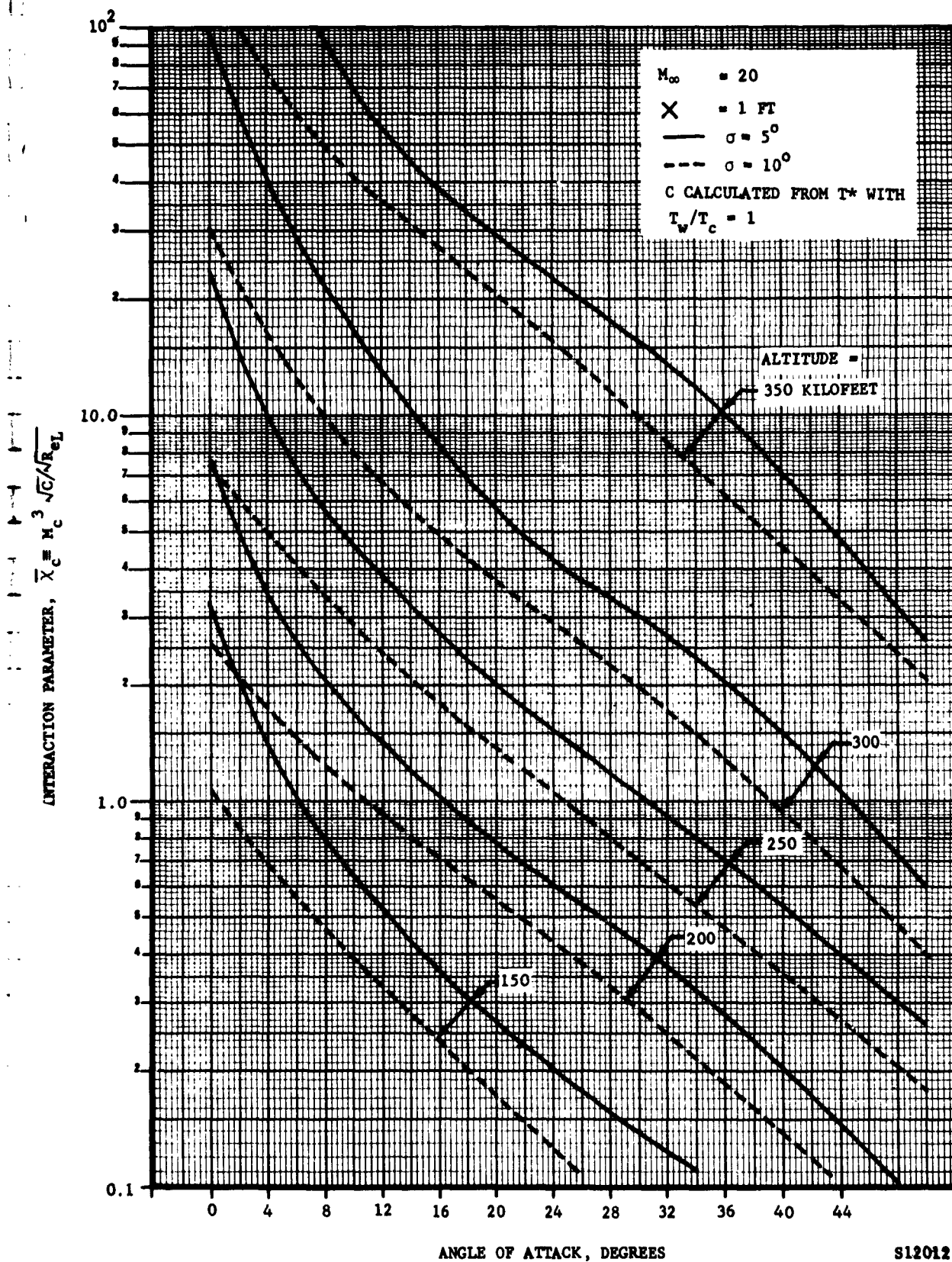


FIGURE 6-1. INTERACTION PARAMETER, χ_c , AT STAGNATION LINE ON CONE

an insulated 10-degree half-angle cone should not have any appreciable viscous interaction effects noticeable for $\alpha \gtrsim 45$ degrees at 200 kilo-feet altitude; whereas this would change for a highly cooled cone to $\alpha \gtrsim 10$ degrees for the same conditions. The stagnation line region just examined represents the region of maximum compression at angle of attack, and consequently, the region of lowest viscous interaction on the surface of the cone. This is particularly true at sufficiently low angles of attack where the flow originates at the cone vertex, instead of at the stagnation line.

6.3 SHOCK SHAPE AT ARBITRARY ANGLE OF ATTACK

In Section 6.2, requirements were outlined for obtaining local flow properties. A considerable knowledge of the properties in the hypersonic flow field may be obtained from the local slope of the shock wave. The conical shock angle at $\alpha = 0$ was determined numerically in Reference 32 and graphically presented in NACA Number TR1135 for a perfect gas. The shock shape was also obtained in References 33 and 34 for very small angles of attack; but these are insufficient for the present problem. A past for an approximate estimation of the shock angle in the plane of symmetry is to use an equivalent cone method where the shock angle is obtained from an equivalent cone with $\sigma_{\text{equiv}} = \sigma + \alpha$. This approximation becomes progressively worse with increasing α , and approaches the two-dimensional wedge value at large α . The use of hypersonic small perturbation theory is also inadequate, as the assumptions for its validity are violated except at very small angle of attack.

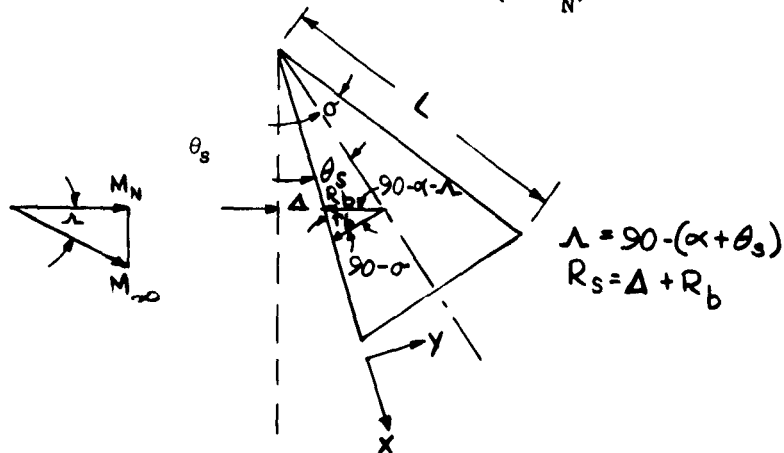
More recently, Gonor^{35,36} has examined the conical flow field at angle of attack for $M_\infty \gg 1$, and derived an analytical expression for the shock angle in the plane of symmetry. This expression has the form:

$$\theta_{\pm}^{\pm} = \sigma + \frac{\tan(\sigma \pm \alpha)}{t^2} \left[(1+t) \ln(1+t) - t \right] \frac{\gamma-1}{\gamma+1} \left[1 + \frac{2}{(\gamma-1)M_\infty^2 \sin^2(\sigma \pm \alpha)} \right] \quad 6.1$$

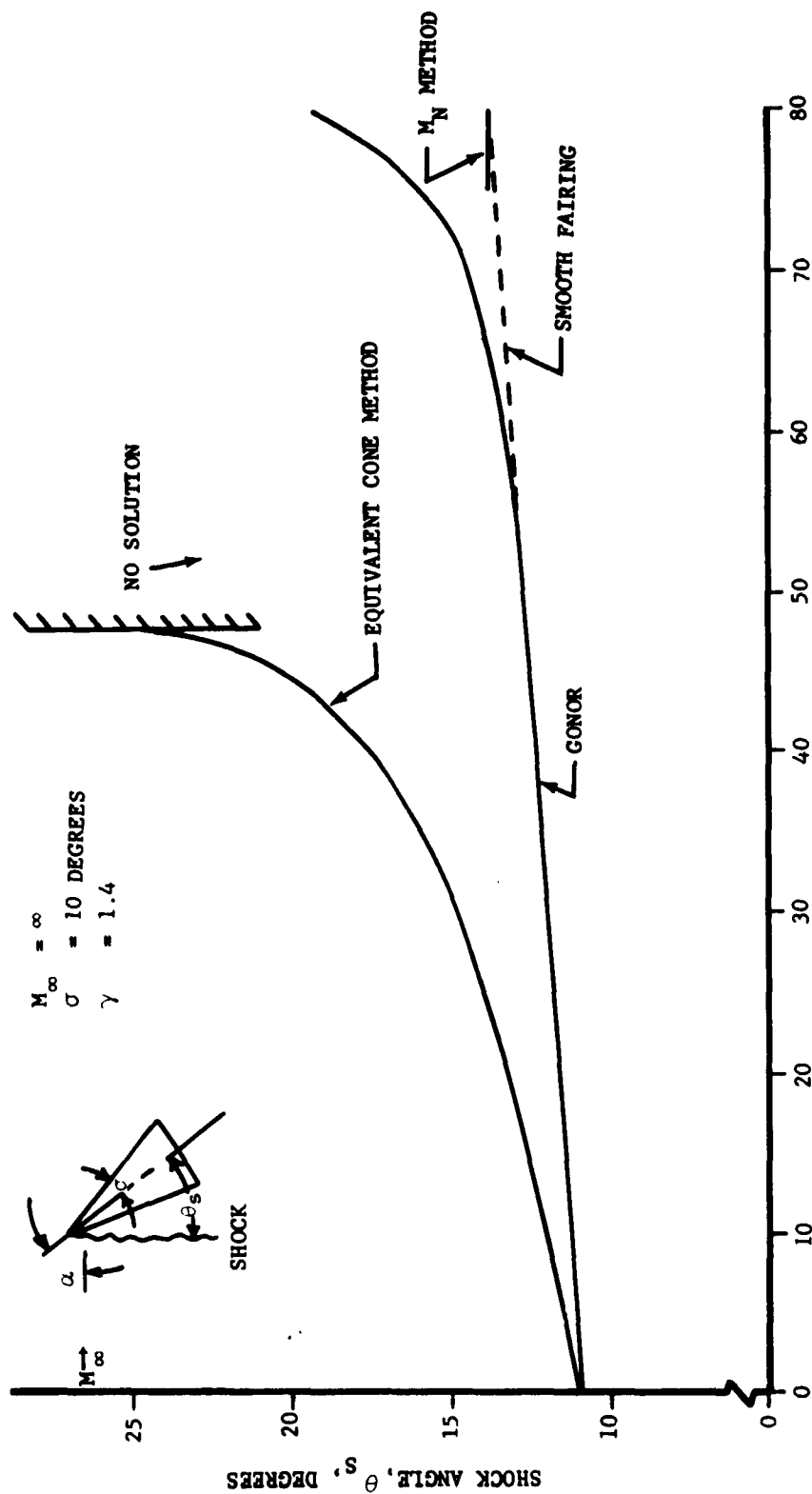
where $t = \pm \sin \alpha / \sin \sigma \cos(\sigma \pm \alpha)$

The upper sign in Equation 6.1 refers to a meridional plane located on the most windward side, and the lower sign to a meridional plane on the most leeward side. The term $\frac{\gamma-1}{\gamma+1} \left[1 + \frac{2}{(\gamma-1)M_\infty^2 \sin^2(\sigma+\alpha)} \right]$ is approximately the density ratio, ϵ , across the conical shock wave in a very high Mach number flow. Gonor has compared Equation 6.1 with experiment and found satisfactory agreement at small angles of attack at $M_\infty = 4.0$. The leeward side solution is invalid for $\alpha > \sigma$. The windward side solution has been examined for $\alpha > \sigma$ and is compared with the equivalent cone method in Figure 6-2 for $\sigma = 10$ degrees at $M_\infty = \infty$. Both solutions exhibit sudden asymptotic increases as α increases. In the region of large α , θ_s should approach an equivalent value for a blunt body standoff distance. The limiting value of θ_s at large α , for which Equation 6.1 can be expected to be valid, is uncertain. Such experiments as those in Reference 37, however, indicate a near conical flow up to an angle of attack of approximately 60 degrees.

An estimation of the shock angle's limiting value at very large angle of attack may be made by considering the flow over a swept cylinder at zero yaw. The shock standoff distance varies inversely as the local radius of curvature. If this type solution is applied to a slender cone by using an equivalent local radius, a shock standoff distance is generated which varies linearly with axial distance. It may be considered to be a shock angle in the conical sense. A solution of this type will now be considered and termed the normal Mach number (or M_N) method.



In the above sketch, the cone is assumed to act as a cylinder whose local radius of curvature, R_b , is parallel to the flow normal to the shock wave.



Ford Motor Company
AERONUTRONIC DIVISION

Then

$$r_b = x \tan \sigma \quad 6.2$$

$$R_b = r_b \sin(90 - \sigma) / \sin(\sigma + \alpha + \Delta) \quad 6.3$$

$$= x \sin \sigma / \cos(\theta_s - \sigma) \quad 6.3a$$

$$R_s = x \sin \theta_s \quad 6.4$$

$$\Delta / R_b = \frac{\sin \theta_s \cos(\theta_s - \sigma)}{\sin \sigma} - 1 \quad 6.5$$

and

$$\sin \theta_s \cos(\theta_s - \sigma) = (1 + \frac{\Delta}{R_b}) \sin \sigma \quad 6.6$$

Equation 6.6 is an implicit relationship for θ_s which must be solved by trial and error or an iteration procedure. It is seen that in a hypersonic flow, $\cos(\theta_s - \sigma) \approx 1$, so that a good approximation for Equation 6.6 is:

$$\sin \theta_s \approx (1 + \frac{\Delta}{R_b}) \sin \sigma \quad 6.6a$$

This solution for the shock angle at very large α is very similar to that developed in Reference 38. An empirical relationship for the shock stand-off distance, Δ , is also presented in Reference 38:

$$\frac{\Delta}{R_b} = 0.38 + 2.4 / (M_N^2 - 1) + 1.4 / (M_N^2 - 1)^2 \quad 6.7$$

Substitution of 6.7 into 6.6 gives

$$\sin \theta_s \cos(\theta_s - \sigma) = \left[1.38 + 2.4 / (M_N^2 - 1) + 1.4 / (M_N^2 - 1)^2 \right] \sin \sigma \quad 6.8$$

or

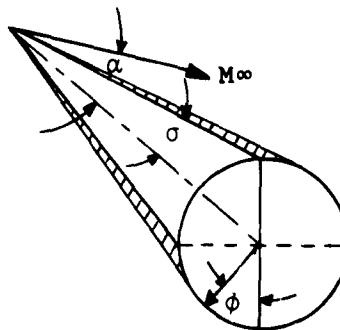
$$\sin \theta_s \approx \left[1.38 + \frac{2.4}{M_N^2 - 1} + \frac{1.4}{(M_N^2 - 1)^2} \right] \sin \sigma \quad 6.8a$$

The use of equation 6.8 in connection with the method of Gonor (Equation 6.3) has been compared with experimental values³⁸ at $M_\infty = 3.86$ in Figure 6-3. The agreement generally good, except at $\alpha = 0$ for the 5-degree cone. Calculations show that values obtained by Gonor's method are in poor agreement with NACA Number 1135 at $\alpha = 0$ for $M_\infty \tan \sigma \gtrsim 1$. At $\alpha = 0$, values from NACA Number 1135 should therefore be used. At large angles of attack, the procedure of fairing a smooth curve tangent to the Gonor curve and through the point at $90^\circ - \theta_s$ obtained from the M_N method produces good agreement with the experimental data. Results for $\sigma = 5, 10$ and 20 degrees are presented in Figure 6-4 for $M_\infty = 10, 25$ and infinity.

At small α the shock wave will still be approximately conical in shape, although the shock angle on the windward side may be greater than on the leeward side⁹. A cross-section of the shock wave tends to be elliptical in shape. An estimation of the local shock angle at a point exactly 90 degrees away from the plane of symmetry gives an approximate value of that at $\alpha = 0$, based on the local body inclination to the freestream. The local inclination of a $\theta = 90$ degree generator is

$$\sin \sigma_{\text{effective}} = \cos \alpha \sin \sigma \quad 6.9$$

where



Calculations for $\sigma = 5$ and 10 degrees show that σ effective to the $\phi = 90^\circ$ generator decreases very slightly at small α :

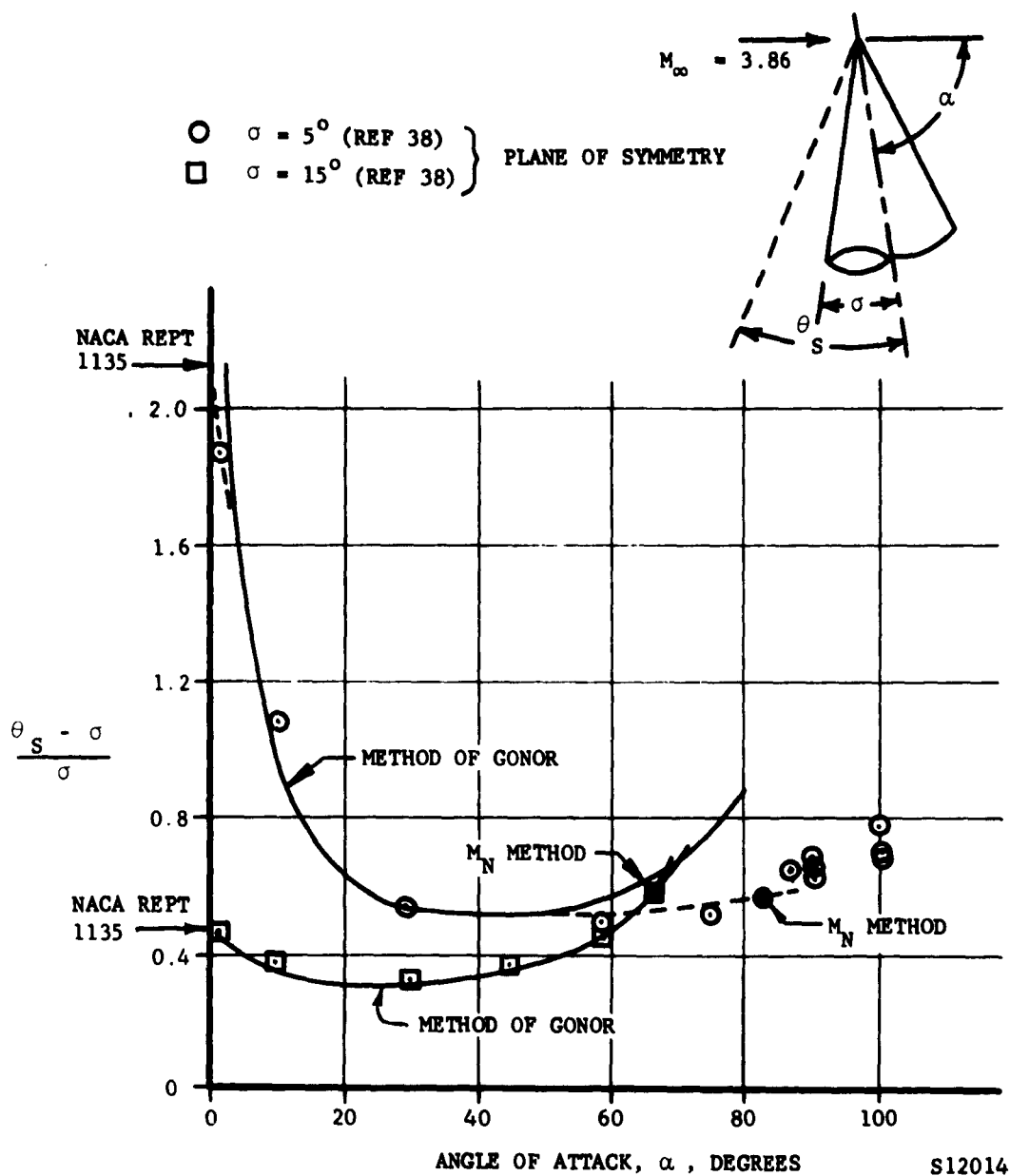


FIGURE 6-3. COMPARISON OF THEORY AND EXPERIMENT FOR SHOCK ANGLE ON SLENDER CONES

Ford Motor Company
AERONAUTRONIC DIVISION

| σ | α | $\sigma_{\text{effective}}$ |
|----------|----------|-----------------------------|
| 5 | 0 | 5.00 |
| | 2 | 4.99 |
| | 5 | 4.98 |
| | 7-1/2 | 4.95 |
| 10 | 0 | 10.00 |
| | 5 | 9.96 |
| | 10 | 9.85 |
| | 12 | 9.78 |

Within the accuracy of the negligible cross flow approximation and the distribution assumptions to be subsequently employed in estimating the aerodynamic force coefficients, it is felt that $\phi = 90$ degrees corresponds to $\alpha = 0$ for a reasonable engineering approximation.

At large α , the shock angle in the plane of symmetry has been discussed. The need to know the shock slope in order to determine local properties is not so great as in the case of small α . At large α , a major portion of the flow has passed through the shock wave near the plane of symmetry, and then mixes with the flow coming through the local portion of the shock wave as the flow expands around the body. An expanding blunt body flow has been previously examined³⁹ and the results are available from the author. The detached shock shape for cylinders has been estimated by Love⁴⁰. The pertinent equations as applied to the case of a slender cone at large angle of attack are presented in Appendix A.

CHAPTER 7

THEORETICAL ESTIMATES OF AERODYNAMIC FORCE COEFFICIENTS AT ANGLE OF ATTACK

7.1 AXIAL FORCES AT SMALL ANGLE OF ATTACK

The major assumption to be employed in analyses of the present kind is the one with respect to what are the distributions of pressures and skin friction shear forces over the surface of the cone. This consideration normally leads one to the conclusion that the solution may be divided into regions, $\alpha \leq \sigma$, and $\alpha > \sigma$ (where the back side of the cone is in shadow). In the second region, the back side pressures are very low, and the usual procedure is to neglect it in any consideration of forces acting on the body. A further division of the solution can be made by examining the front half ($-\pi/2 \leq \phi \leq \pi/2$) and back half ($\pi/2 < \phi < 3\pi/2$) of the cone separately. In low density flows, however, the effects of viscous interaction complicate this picture. As pointed out in Chapter 2, the magnitude of these effects increase as one proceeds away from the compression region at angle of attack towards the back side. It is not immediately apparent what the combined effects of low pressures (or local dynamic pressure) and large viscous interaction effects are on the back side, and at what angle of attack the back side can finally be ignored. It is logically assumed that the pressure contribution for $\alpha > \sigma$ to the axial force would be small although not necessarily negligible since the trigonometric factor for determining the pressure component varies as $\sin \sigma$. The same thing cannot be said for the skin friction contribution, where the trigonometric factor is $\cos \sigma$. This problem will be examined further in Chapter 7.6 when comparisons of theory and experiment are made.

In the determination of the axial force coefficient the following assumptions will be made:

- (1) Modified Newtonian pressure distribution for the inviscid pressures,

$$\frac{C_p}{C_{p_{\phi=0}}} = \cos^2 \beta$$

$$\cos \beta = (\sin \sigma \cos \alpha + \cos \sigma \sin \alpha \cos \phi) / \sin (\alpha + \sigma)$$

$C_{p_{\phi=0}}$ to be determined from the shock slope.

- (2) Induced pressures,

$$\frac{P}{P_c} = 1 + F_c \bar{\chi}_c \quad (\text{Reference Equation 2.22.})$$

- (3) Linear variation of viscous interaction effects for $0 \leq \phi \leq \pi/2$, and $\pi/2 \leq \phi \leq \pi$ as determined by the interaction parameter, $\bar{\chi}_c$. Also, a linear variation of local dynamic pressure and skin friction coefficient with ϕ .

The pressure contribution to the axial force coefficient is assumed to be

$$C_A^P = \frac{1}{q_\infty A_{\text{ref}}} \int_A P_A dA = \frac{2}{q_\infty A_{\text{ref}}} \int_0^L \int_0^\pi P \sin^2 \sigma d\phi dx \quad 7.1$$

With assumptions 1 to 3, Equation 7.1 becomes

$$C_A^P = \frac{2}{q_\infty A_{\text{ref}}} \left\{ \int_0^L \int_0^{\pi/2} P_{c0} \left[\frac{P_\infty}{P_{c0}} + \left(1 - \frac{P_\infty}{P_{c0}} \right) \cos^2 \beta \right] \left[1 + F_c \bar{\chi}_0 + \frac{2}{\pi} \left(F_c \bar{\chi}_{\pi/2} - F_c \bar{\chi}_0 \right) \phi \right] \sin^2 \sigma d\phi dx + \int_0^L \int_{\pi/2}^\pi P_{c0} \left[\frac{P_\infty}{P_{c0}} + \left(1 - \frac{P_\infty}{P_{c0}} \right) \cos^2 \beta \right] \left[1 + 2 F_c \bar{\chi}_{\pi/2} - F_c \bar{\chi}_\pi + \frac{2}{\pi} \left(F_c \bar{\chi}_\pi - F_c \bar{\chi}_{\pi/2} \right) \phi \right] \sin^2 \sigma d\phi dx \right\} \quad 7.2$$

Ford Motor Company,
AERONUTRONIC DIVISION

The first integral represents the contribution of the front side of the cone, and the second integral that of the back side. Integration of 7.2 results in, for the front side,

$$C_{A_1}^P = \frac{2 \sin^2 \sigma P_{c_0} L^2}{q_{\infty} A_{ref}} \left\{ \left[a^2 + (1 - a^2) \frac{P_{\infty}}{P_{c_0}} \right] \frac{\pi}{2} + \left[2ab + \frac{\pi}{4} b^2 \right] \left(1 - \frac{P_{\infty}}{P_{c_0}} \right) \left(\frac{1}{2} + \frac{2}{3} F_c \bar{\chi}_0 \right) + \left[\frac{P_{\infty}}{P_{c_0}} \frac{\pi^2}{8} + \left(1 - \frac{P_{\infty}}{P_{c_0}} \right) \left(\frac{a^2 \pi^2}{8} + 2ab \frac{\pi - 2}{2} + \frac{b^2}{4} \frac{\pi^2 - 4}{4} \right) \right] \right. \\ \left. \left[\frac{4}{3\pi} \left(F_c \bar{\chi}_{\frac{\pi}{2}} - F_c \bar{\chi}_0 \right) \right] \right\} \quad 7.3$$

For the back side, the integral will be assumed to hold for $\alpha \leq \sigma$:

$$C_{A_2}^P = \frac{2 \sin^2 \sigma P_{c_0} L^2}{q_{\infty} A_{ref}} \left\{ \left[a^2 + (1 - a^2) \frac{P_{\infty}}{P_{c_0}} \right] \frac{\pi}{2} + \left(\frac{\pi b^2}{4} - 2ab \right) \left(1 - \frac{P_{\infty}}{P_{c_0}} \right) \cdot \right. \\ \left(\frac{1}{2} + \frac{4}{3} F_c \bar{\chi}_{\frac{\pi}{2}} - \frac{2}{3} F_c \bar{\chi}_{\pi} \right) + \left[\frac{P_{\infty}}{P_{c_0}} \frac{3\pi^2}{8} + \left(1 - \frac{P_{\infty}}{P_{c_0}} \right) \left(\frac{3\pi^2}{8} a^2 - 2ab \frac{\pi + 2}{2} + \right. \right. \\ \left. \left. b^2 \left(\frac{3\pi^2}{16} + \frac{1}{4} \right) \right) \right] \left[\frac{4}{3\pi} \left(F_c \bar{\chi}_{\pi} - F_c \bar{\chi}_{\frac{\pi}{2}} \right) \right] \right\} \quad 7.4$$

Similarly, the skin friction contribution to the axial forces is

$$C_A^F = \frac{1}{q_{\infty} A_{ref}} \int_A C_f(x, \phi) q_{\theta}(\phi) \cos \sigma dA \quad 7.5$$

The value for $C_f(x)$ and resultant integration was taken from Equations 4.2 and 4.3, where both the viscous interaction and transverse curvature effects are included:

$$C_{A_1}^F = \frac{\cos \sigma \sin \sigma L^2}{q_\infty A_{ref}} \frac{\pi}{3} \left[\left(q_0 + \frac{q_{\pi/2}}{2} \right) \frac{C_{F_0}}{2} \frac{q_\infty}{q_c} + \left(q_\pi + \frac{q_0}{2} \right) \frac{C_{F_\pi}}{2} \frac{q_\infty}{q_c} \right] \quad 7.6$$

$$C_{A_2}^F = \frac{\cos \sigma \sin \sigma L^2}{q_\infty A_{ref}} \frac{\pi}{3} \left[\left(q_{\pi/2} + \frac{q_\pi}{2} \right) \frac{C_{F_{\pi/2}}}{2} \frac{q_\infty}{q_c} + \left(q_\pi + \frac{q_{\pi/2}}{2} \right) \frac{C_{F_\pi}}{2} \frac{q_\infty}{q_c} \right] \quad 7.7$$

The subscripts 0, $\pi/2$, π refer to ϕ , and the values of $(C_F \phi/2) q_\infty/q_c$ may be obtained from Equation 4.3 by using local properties at each value of ϕ . The total axial force coefficient is

$$C_A^T = C_{A_1}^P + C_{A_2}^P + C_{A_1}^F + C_{A_2}^F \quad 7.8$$

where any base contribution has been neglected. Any base pressure would subtract from the value of C_A^T given in Equation 7.9.

7.2 NORMAL AND MOMENT FORCES AT SMALL ANGLE OF ATTACK

The same assumptions will be employed for the normal and moment forces as in the determination of the axial forces. The integral for the normal force coefficient then becomes

$$C_N = \frac{2}{q_\infty A_{ref}} \int_0^L \int_0^\pi \left[P_N \cos \sigma \sin \sigma \cos \phi d\phi dx - C_f(x, \phi) q_\phi(\phi) \cos \phi \sin^2 \sigma d\phi dx \right] \quad 7.9$$

Integration of Equation 7.9 gives

$$C_{N_1}^P = \frac{2 \cos \sigma \sin \sigma P_{c_0} L^2}{q_\infty A_{ref}} \left\{ \frac{1}{2} \left[\frac{P_\infty}{P_{c_0}} + \left(1 - \frac{P_\infty}{P_{c_0}} \right) \left(a^2 + \frac{\pi}{2} ab + \frac{2}{3} b^2 \right) \right] \left[1 + \frac{4}{3} F_c \bar{\chi}_0 \right] + \frac{4}{3\pi} \left[\left(\frac{\pi}{2} - 1 \right) \frac{P_\infty}{P_{c_0}} + \left(1 - \frac{P_\infty}{P_{c_0}} \right) \left(\frac{\pi-2}{2} a^2 + \left(\frac{\pi}{2} - 1 + \frac{\pi^4}{16} \right) \frac{ab}{2} + \left(\frac{\pi}{3} - \frac{7}{9} \right) b^2 \right) \right] \left[F_c \bar{\chi}_{\pi/2} - F_c \bar{\chi}_0 \right] \right\} \quad 7.10$$

$$C_{N_2}^P = \frac{2 \cos \sigma \sin \sigma P_{c_0} L^2}{q_\infty A_{ref}} \left\{ \frac{1}{2} \left[\left(1 - \frac{P_\infty}{P_{c_0}} \right) \left(\frac{\pi}{2} ab - a^2 - \frac{2b^2}{3} \right) - \frac{P_\infty}{P_{c_0}} \right] \right. \\ \left. \left[1 + \frac{8}{3} F_c \bar{\chi}_{\frac{\pi}{2}} - \frac{4}{3} F_c \bar{\chi}_\pi \right] + \frac{4}{3\pi} \left[\left(1 - \frac{P_\infty}{P_{c_0}} \right) \left(2ab \left(\frac{\pi^4}{4} \frac{15}{16} - \frac{\pi}{8} + \frac{1}{4} \right) - \right. \right. \right. \\ \left. \left. \left(\frac{\pi+2}{2} \right) a^2 - \left(\frac{7}{9} + \frac{\pi}{3} \right) b^2 \right) - \frac{P_\infty}{P_{c_0}} \left(\frac{\pi+2}{2} \right) \right] \left[F_c \bar{\chi}_\pi - F_c \bar{\chi}_{\frac{\pi}{2}} \right] \right\} \quad 7.11$$

$$C_{N_1}^F = \frac{-2 \sin^2 \sigma L^2}{q_\infty A_{ref} \pi^2} \left\{ \left[(4\pi - 8)q_0 + (8 - 2\pi)q_{\frac{\pi}{2}} \right] \frac{C_{F_0}}{2} \frac{q_\infty}{q_c} + \right. \\ \left. \left[(8 - 2\pi)q_0 + (\pi^2 - 8)q_{\frac{\pi}{2}} \right] \frac{C_F}{2} \frac{\pi}{2} \frac{q_\infty}{q_c} \right\} \quad 7.12$$

$$C_{N_2}^F = \frac{2 \sin^2 \sigma L^2}{q_\infty A_{ref} \pi^2} \left\{ \left[(4\pi - 8)q_\pi + (8 - 2\pi)q_{\frac{\pi}{2}} \right] \frac{C_{F_\pi}}{2} \frac{q_\infty}{q_c} + \right. \\ \left. \left[(8 - 2\pi)q_\pi + (\pi^2 - 8)q_{\frac{\pi}{2}} \right] \frac{C_F}{2} \frac{\pi}{2} \frac{q_\infty}{q_c} \right\} \quad 7.13$$

$$C_N^T = C_{N_1}^P + C_{N_2}^P + C_{N_1}^F + C_{N_2}^F \quad 7.14$$

Equations 7.11 and 7.13 are assumed valid for $\alpha \leq \sigma$. By applying the same assumptions, the integral for the moment coefficient takes the form:

$$C_M^{(nose)} = \frac{-1}{q_\infty A_{ref} l_{ref}} \int_A [P_N x dA - C_f(x, \phi) q_\phi(\phi) \cos \phi \sin \sigma x dA] \quad 7.15$$

A positive moment is taken here as the clockwise direction.

The integration of Equation 7.15 gives

$$C_{M_1}^P = \frac{-2 \cos \sigma \sin \sigma L^3 P_{c_0}}{q_\infty A_{\text{ref}} l_{\text{ref}}} \left\{ \left[\frac{P_\infty}{P_{c_0}} + \left(1 - \frac{P_\infty}{P_{c_0}} \right) \left(a^2 + \frac{\pi}{2} ab + \frac{2}{3} b^2 \right) \right] \right. \\ \left. \left[\frac{1}{3} + \frac{2}{5} F_c \bar{\chi}_0 \right] + \frac{4}{5\pi} \left[\frac{\pi - 2}{2} \frac{P_\infty}{P_{c_0}} + \left(1 - \frac{P_\infty}{P_{c_0}} \right) \left(\frac{\pi - 2}{2} a^2 + \right. \right. \right. \\ \left. \left. \left(\frac{\pi}{2} - 1 + \frac{\pi^4}{16} \right) \frac{ab}{2} + \left(\frac{\pi}{3} - \frac{7}{9} \right) b^2 \right) \right] \left[F_c \bar{\chi}_{\frac{\pi}{2}} - F_c \bar{\chi}_0 \right] \right\} \quad 7.16$$

$$C_{M_2}^P = \frac{-2 \cos \sigma \sin \sigma L^3 P_{c_0}}{q_\infty A_{\text{ref}} l_{\text{ref}}} \left\{ \left[\left(1 - \frac{P_\infty}{P_{c_0}} \right) \left(\frac{\pi}{2} ab - a^2 - \frac{2b^2}{3} \right) - \frac{P_\infty}{P_{c_0}} \right] \right. \\ \left[\frac{1}{3} + \frac{4}{5} F_c \bar{\chi}_{\frac{\pi}{2}} - \frac{2}{5} F_c \bar{\chi}_\pi \right] + \frac{4}{5\pi} \left[\left(1 - \frac{P_\infty}{P_{c_0}} \right) \left(2ab \left(\frac{\pi^4}{4} \cdot \frac{15}{16} - \frac{\pi}{8} + \frac{1}{4} \right) - \right. \right. \\ \left. \left. \frac{\pi + 2}{2} a^2 - \left(\frac{7}{9} + \frac{\pi}{3} \right) b^2 \right) - \frac{P_\infty}{P_{c_0}} \frac{\pi + 2}{2} \right] \left[F_c \bar{\chi}_\pi - F_c \bar{\chi}_{\frac{\pi}{2}} \right] \right\} \quad 7.17$$

$$C_{M_1}^F = \frac{2 \sin^2 \sigma L^3}{q_\infty A_{\text{ref}} l_{\text{ref}} \pi^2} \left[H_{1_0} J_0 + H_{2_0} J_{\frac{\pi}{2}} \right] \quad 7.18$$

$$C_{M_2}^F = \frac{-2 \sin^2 \sigma L^3}{q_\infty A_{\text{ref}} l_{\text{ref}} \pi^2} \left[H_{1_\pi} J_\pi + H_{2_\pi} J_{\frac{\pi}{2}} \right] \quad 7.19$$

Ford Motor Company
AERONUTRONIC DIVISION

where

$$H_{1\phi} = (4\pi - 8) q_{\phi} + (8 - 2\pi) q_{\frac{\pi}{2}}$$

$$H_{2\phi} = (8 - 2\pi) q_{\phi} + (\pi^2 - 8) q_{\frac{\pi}{2}}$$

$$J_{\phi} = (1 + F_c \bar{\chi}_{\phi})^{3/2} \sqrt{\frac{3C}{Re_L}} \left\{ 0.266 + 0.332 \xi \left(0.517 + 0.913 \frac{T_w}{T_c} + \right. \right. \\ \left. \left. 0.121(\gamma - 1) M_c^2 \right) - 0.232 F_c \bar{\chi}_{\phi} + F \bar{\chi}_{\phi} \left[1.162 F_c \bar{\chi}_{\phi} - \right. \right. \\ \left. \left. 1.660 \xi \left(0.517 + 0.913 \frac{T_w}{T_c} + 0.121 (\gamma - 1) M_c^2 \right) \right] \left[\frac{1}{6} - \right. \right. \\ \left. \left. \frac{F_c \bar{\chi}_{\phi}}{8} + \frac{\gamma F_c \bar{\chi}_{\phi}}{10} (1 + F_c \bar{\chi}_{\phi})^{-1/2} + \frac{1}{16} \left(\frac{F_c \bar{\chi}_{\phi}}{(1 + F_c \bar{\chi}_{\phi})^{1/2}} \right)^3 \right. \right. \\ \left. \left. \ln \frac{1 + (1 + F_c \bar{\chi}_{\phi})^{1/2}}{(F_c \bar{\chi}_{\phi})^{1/2}} \right] \right\}$$

$$a = \sin \sigma \cos \alpha / \sin (\sigma + \alpha)$$

$$b = \cos \sigma \sin \alpha / \sin (\alpha + \sigma)$$

$$C_M^T = C_{M_1}^P + C_{M_2}^P + C_{M_1}^F + C_{M_2}^F \quad 7.20$$

7.3 SMALL ANGLE OF ATTACK, $\alpha > \sigma$

In Equations 7.4 to 7.11 the solutions for the back side of the cone apply only for $\alpha < \sigma$. In the region $\alpha > \sigma$, the determination of the terms containing $\gamma F_c \bar{\chi}_{\phi}$ poses a problem as the original derivations are valid for $K_b = M_{\infty} \Theta_b \geq 1$. Since the contribution of the back side is

expected to be smaller than that of the front side, the determination of the viscous interaction effects will be made by assuming a linear variation of $F_c/\gamma = 0.492$ at $K_b = 1$ to $F_c/\gamma = 1$ at $K_b = 0$, in a manner analogous to the case of the flat plate. In the region $\alpha > \sigma$, but still at small α , the determination of the back side contribution to the force coefficients is liable to much uncertainty. The general level of the back side pressure is probably of the order of the free stream value. The consideration of the back side contribution would be approximately equivalent to the use of a pressure differential for the pressure level on the front side in the force integrals ($C\alpha \int_A (P - P_\infty) dA$) and neglecting the back side altogether, if there were no viscous interaction effects.

It is obvious that the general trend of the back side contribution is to decrease with increasing angle of attack. The pressure coefficient across a shock wave varies as the square of the sine of the local shock angle. It will, therefore, be assumed that the back side pressure is reduced approximately by $\cos^2 \alpha$. An estimation of the back side contribution of skin friction forces will then be made by assuming freestream conditions at $\phi = \pi$, $\alpha = \sigma$, and allowing the skin friction coefficient to decrease as $\cos^2 \alpha$ so that $C_{A_2}^F = C_{A_2}^F \cos^2 \alpha$ in the case $\alpha=0$

of the axial skin friction force coefficient. An examination of the skin friction forces contributing to C_N and C_M reveals the front and back side are of the same order of magnitude and of opposite sign. The net contribution of shearing forces is negligible. A similar estimation in the case of the back side pressure contribution will be made from the $\alpha = \sigma$ condition by assuming a constant inviscid pressure on the back side of freestream magnitude. This gives for $\alpha > \sigma$:

$$C_{A_2}^P = \frac{\pi P_\infty L^2 \sin^2 \sigma \cos^2 \alpha}{q_\infty A_{ref}} \left[\frac{1}{2} + \frac{1}{3} \left(F_c \bar{\chi}_{\frac{\pi}{2}} + F_c \bar{\chi}_\pi \right) \cos^2 \alpha \right] \quad 7.21$$

$$C_{N_2}^P = \frac{\pi \cos \sigma \sin \sigma \cos^2 \alpha P_\infty L^2}{q_\infty A_{ref}} \left[\frac{1}{2} + \frac{1}{3} \left(F_c \bar{\chi}_{\frac{\pi}{2}} + F_c \bar{\chi}_\pi \right) \cos^2 \alpha \right] \quad 7.22$$

$$C_{M_2}^P = \frac{\pi \cos \sigma \sin \sigma \cos^2 \alpha P_\infty L^3}{q_\infty A_{ref} l_{ref}} \left[\frac{1}{3} + \frac{1}{5} \left(F_c \bar{\chi}_{\frac{\pi}{2}} + F_c \bar{\chi}_\pi \right) \cos^2 \alpha \right] \quad 7.23$$

where the interaction parameters are to be evaluated at $\alpha = \sigma$.

7.4 CENTER OF PRESSURE

The center of pressure for the cone may be determined once the previous normal and moment force coefficients are known. It is given by

$$\frac{l_{c.p.}}{l_{ref}} = \frac{-C_M}{C_N} \quad 7.24$$

7.5 AERODYNAMIC FORCES AT LARGE ANGLE OF ATTACK

In the large angle of attack region, the viscous interaction effects have essentially disappeared. In addition, any contribution from the back side is assumed negligible, so that only a consideration of the forces acting on the front side is of interest. For simplicity, the pressure forces are assumed to be given by Newtonian theory. The Newtonian force coefficients as obtained from Reference 41 are:

$$C_A^P = \left(\frac{\delta}{\pi} + \frac{1}{2}\right) \left[2 \sin^2 \sigma + \sin^2 \alpha (1 - 3 \sin^2 \sigma) \right] + \frac{3}{4\pi} \cos \delta \sin 2\alpha \sin 2\sigma \quad 7.25$$

$$C_N^P = \frac{\cos^2 \sigma \sin 2\alpha}{\pi} \left\{ \delta + \frac{\pi}{2} + \frac{1}{6} \sin^2 \delta (1 + 2 \csc^2 \delta) \right\} \quad 7.26$$

$$C_M^P = \frac{-2}{3} \frac{\sin 2\alpha}{\pi} \left[\delta + \frac{\pi}{2} + \frac{1}{6} \sin 2\delta (1 + 2 \csc^2 \delta) \right] \quad 7.27$$

where

$$\sin \delta = \tan \sigma / \tan \alpha$$

$$A_{ref} = A_{base}$$

The center of pressure for Newtonian theory is given by the expression

$$\frac{l_{c.p.}}{L} = \frac{2}{3} \sec^2 \sigma \cos \sigma = \frac{2}{3} / \cos \sigma \quad 7.28$$

(L = slant length)

These expressions are also applicable to the small angle of attack case, if δ is set equal to $\pi/2$ for $\alpha \leq \sigma$.

At large angle of attack it will be assumed that infinite swept cylinder theory⁴²⁻⁴⁴ can be applied to the slender cones of interest. Solutions are obtained by assuming local similarity and satisfying the requirement that the chordwise and spanwise boundary layer development are not independent for variable fluid properties. In the nomenclature of Reference 44, the spanwise and chordwise skin friction shear forces are, respectively;

$$\tau_{w,s} = \left[2H_e (1 - t_s) \frac{\rho_w \mu_w}{\beta} \frac{t_s}{t_e} \frac{du_e}{dx} \right]^{1/2} g'_w \quad 7.29$$

$$\tau_{w,c} = \left[2H_e (t_s - t_e) \frac{\rho_w \mu_w}{\beta} \frac{t_s}{t_e} \frac{du_e}{dx} \right]^{1/2} f''_w \quad 7.30$$

The development of the spanwise skin friction solution into the axial skin friction force coefficient is as follows: The definition of the pressure gradient parameter, β , is

$$\beta = \frac{2}{u_e} \frac{du_e}{dx} \frac{t_s/t_e}{\rho_w \mu_w} \int_0^\phi \rho_w \mu_w u_e R_b d\phi \quad 7.31$$

For an isothermal wall, substitution of 7.22 into 7.29 gives

$$\tau_{w,s} = \left[\frac{2H_e (1 - t_s) (\rho_w \mu_w)^2 u_e^2 / 2}{R_b \mu_w \int_0^\phi \rho_w u_e d\phi} \right]^{1/2} g'_w \quad 7.32$$

The axial skin friction force coefficient is given by

$$C_A^F = \frac{2}{q_\infty A_{ref}} \int_0^L \int_0^{\pi/2} \tau_{w,s} \cos \sigma \sin \sigma d\phi dx \quad 7.33$$

This integral cannot be integrated in closed form unless suitable simplifying distributions for the local velocity and density are assumed. For this reason an average or barred value of ρ_e will be assumed and a linear variation of u_e with ϕ such that $u_e/U_\infty = 2/7 \pi \phi \sin^2(\alpha + \theta_s)$. Then

$$\tau_{w,s} = \left\{ \frac{H_e (1 - t_s) \bar{\rho}_w \mu_w \left[\frac{2}{\pi} U_\infty \phi \sin^2(\alpha + \theta_s) \right]^2}{R_b \int_0^\phi \frac{2}{\pi} U_\infty \phi \sin^2(\alpha + \theta_s) d\phi} \right\} g'_w \quad 7.34$$

The axial skin friction force coefficient then becomes

$$C_A^F = \frac{2 \cos \sigma \sin \sigma}{q_\infty A_{ref}} \int_0^L \int_0^{\frac{\pi}{2}} \left[\frac{H_e (1 - t_s) \bar{\rho}_w \mu_w \frac{2}{\pi} U_\infty \cdot 2 \sin^2(\alpha + \theta_s)}{R_b} \right]^{1/2} g'_w d\phi dx \quad 7.35$$

or

$$C_A^F = \frac{2 \cos \sigma \sin \sigma}{q_\infty A_{ref}} \left[H_e (1 - t_s) \bar{\rho}_w \mu_w \frac{4}{\pi} U_\infty \sin^2(\alpha + \theta_s) \right]^{1/2} \int_0^L \int_0^{\frac{\pi}{2}} \frac{g'_w d\phi dx}{\sqrt{R_b}} \quad 7.36$$

Solutions for g'_w as a function of β and heat transfer have been tabulated in Reference 44. To the accuracy employed in the previous assumptions for ρ_w and u_e , it will also be appropriate to assume an average value of g'_w such that a linear variation of β with ϕ gives

$$\bar{g}'_w = \frac{1}{1 - \beta_0} \int_0^{\beta_0} g'_w d\beta \quad 7.37$$

with $\beta_0 \approx \cos(\alpha + \theta_s)$

This assumption in connection with Equation 6.3 gives for the final integration:

$$C_A^F = \frac{2\pi}{3} \frac{\cos \sigma \sin \sigma L^2}{q_\infty A_{ref}} \left[\frac{4H_e(1 - t_s) \bar{\rho}_w \mu_w U_\infty \sin^2(\alpha + \theta_s) \cos(\theta_s - \sigma)}{\pi L \sin \sigma} \right]^{1/2} \bar{g}'_w \quad 7.38$$

The only undetermined value in Equation 7.38 is that of the average density, $\bar{\rho}_w$. A modified Newtonian pressure distribution with ϕ , and a linear viscosity-temperature relationship gives

$$\bar{\rho}_w \mu_w \approx 0.5 \rho_\infty \mu_\infty C_w \left(\frac{P_{t_o}}{P_\infty} + 1 \right) \quad 7.39$$

where the total pressure P_{t_o} is the value obtained at the stagnation line from the normal Mach number component. Substitution of 7.38 into 7.37 and algebraic rearrangement gives for the final solution:

$$C_A^F = \frac{4\sqrt{\pi}}{3} \frac{\cos \sigma \sin \sigma L^2}{A_{ref}} \left[\frac{(1 - t_s) \sin^2(\alpha + \theta_s) \cos(\theta_s - \sigma) C_w \left(\frac{P_{t_o}}{P_\infty} + 1 \right)}{Re_{\infty L} \sin \sigma} \right]^{1/2} \bar{g}'_w \quad 7.40$$

The values obtained for \bar{g}'_w are presented in Figure 7-1 for a Prandtl number of 1.0.

The total axial force coefficient is given by

$$C_A^T = C_A^{NEWT} + C_A^F \quad 7.41$$

The skin friction contribution to the normal force coefficient may be obtained in a similar manner to that for the axial coefficient by using Equation 7.30 in place of 7.29.

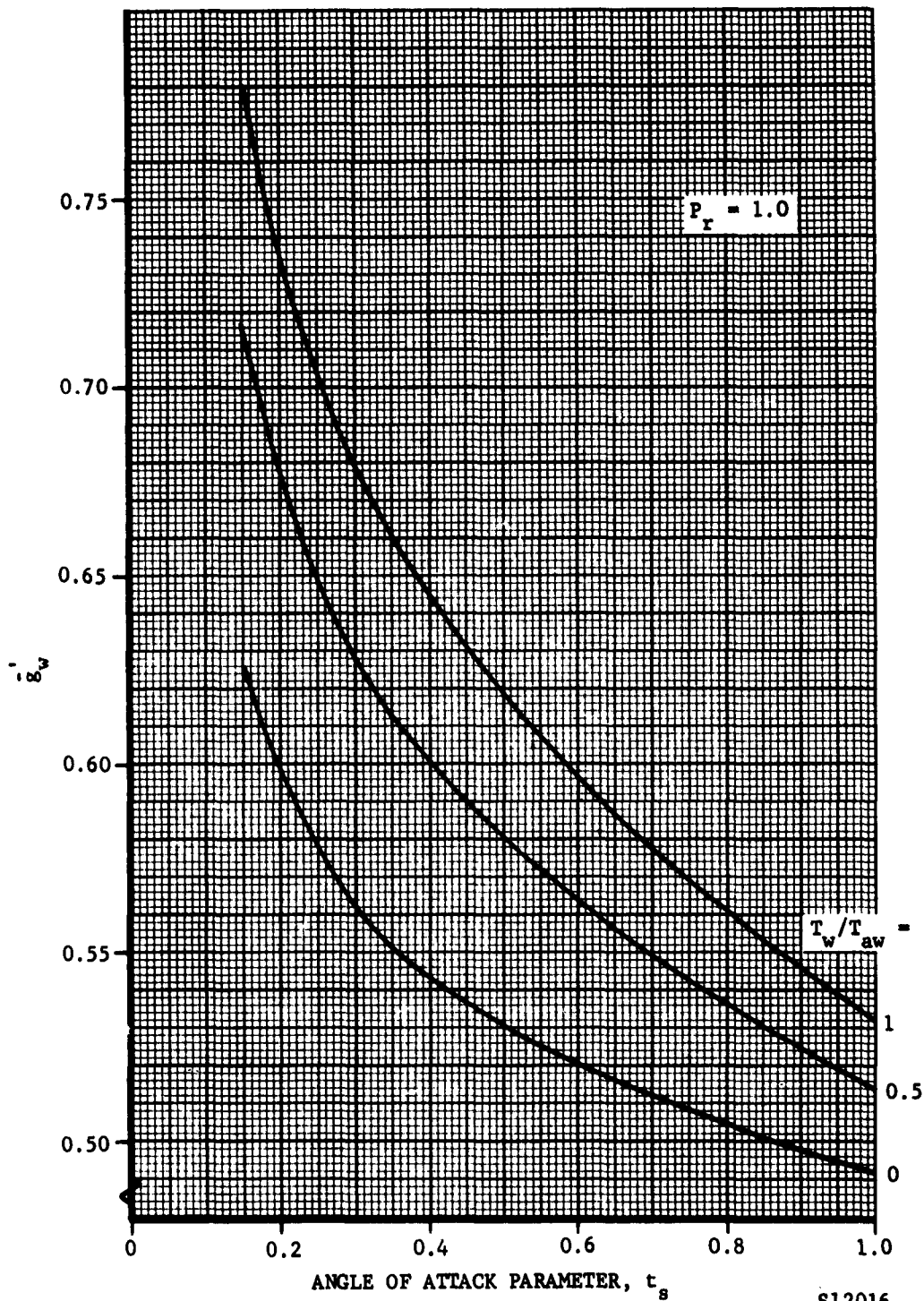


FIGURE 7-1. VARIATION OF $\frac{p}{p_0}$ WITH ANGLE OF ATTACK

$$C_N^F = \frac{2}{q_\infty A_{\text{ref}}} \int_0^L \int_0^{\frac{\pi}{2}} \tau_{w,c} \sin \phi \sin \sigma d\phi dx \quad 7.42$$

or,

$$C_N^F = \frac{16 \sin \sigma L^2 \sin^3 (\theta_s + \alpha)}{3\pi^{3/2} A_{\text{ref}}} \left[\left(\frac{P_{t_o}}{P_\infty} + 1 \right) \frac{C_w \cos (\theta_s - \sigma)}{Re_{\infty L} \sin \sigma} \right]^{1/2} f''_w \quad 7.43$$

Values of f''_w for $Pr = 1$ are given in Figure 7-2. It is noted that the variation of f''_w with Prandtl number is much larger than in the case of g'_w , with f''_w decreasing as the Prandtl number decreases.

The moment coefficient, based on the cone axial length as the reference length follows from Equation 7.42 by multiplying the integrand by the moment arm, and is given by

$$C_M^F = \frac{-3}{5} \frac{C_N^F}{\cos \sigma} \quad 7.44$$

The center of pressure is again given by Equation 7.24 where the total normal and moment coefficients are obtained by summing up the individual contributions. The moment about the c.g. location is given by

$$C_M(c.g.) = -C_N \left[\frac{\ell_{c.p.} - \ell_{c.g.}}{\ell_{\text{ref}}} \right] \quad 7.45$$

7.6 COMPARISON OF EXPERIMENT AND THEORY

The analytical solutions presented have been compared with experiment in Figures 7-3 to 7-10. Also shown for comparison are the Newtonian estimates of the aerodynamic forces. The region of intermediate angle of attack are estimated by a smooth curve arbitrarily faired between the small and large angle of attack solutions.

Data from Reference 45 for an insulated 9-degree half-angle cone at $M_\infty \approx 5.8$ are used for the experimental data in Figures 7-3 to 7-5. These data are approximated by Newtonian theory for the normal

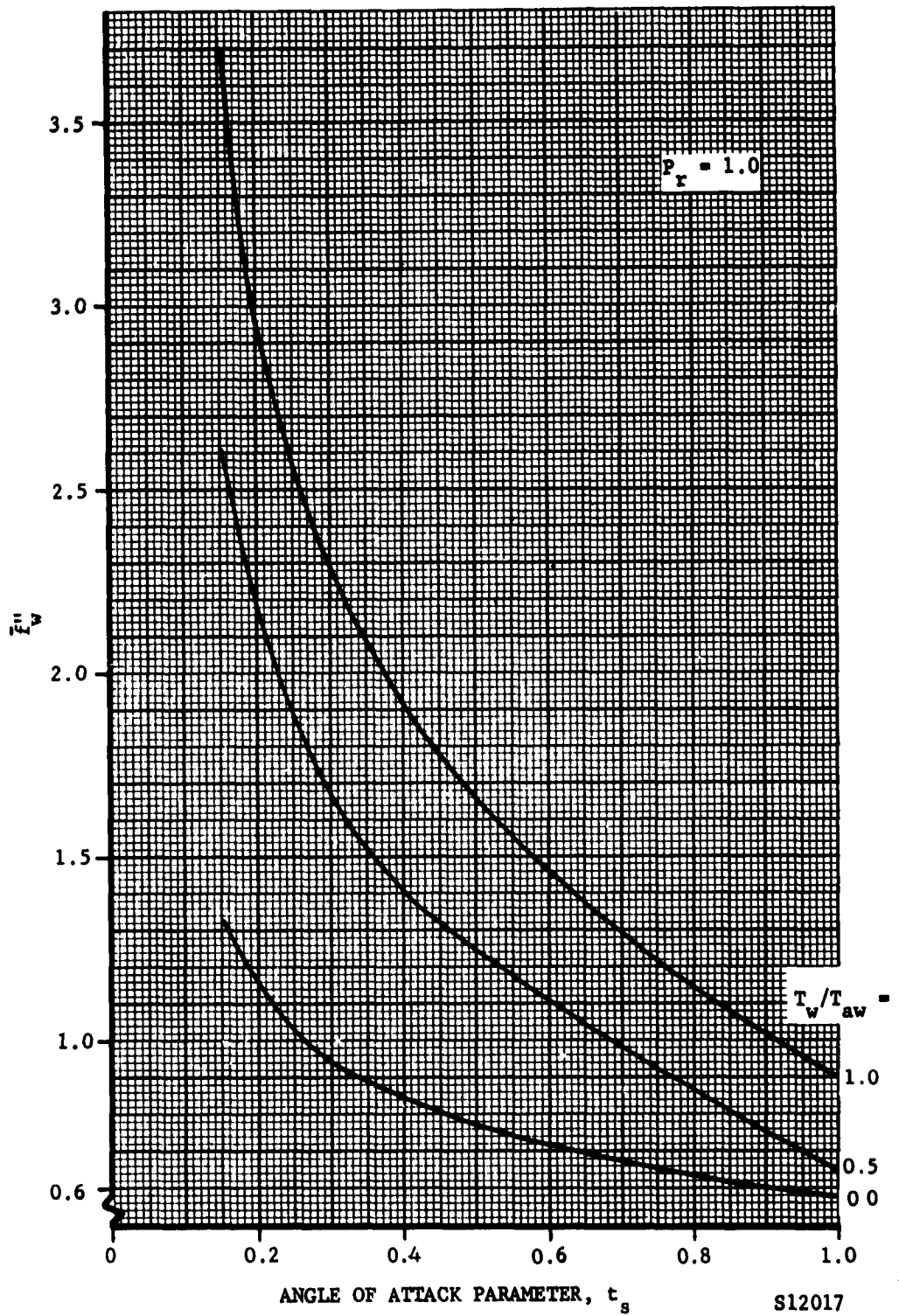


FIGURE 7-2. VARIATION OF \ddot{f}_w'' WITH ANGLE OF ATTACK

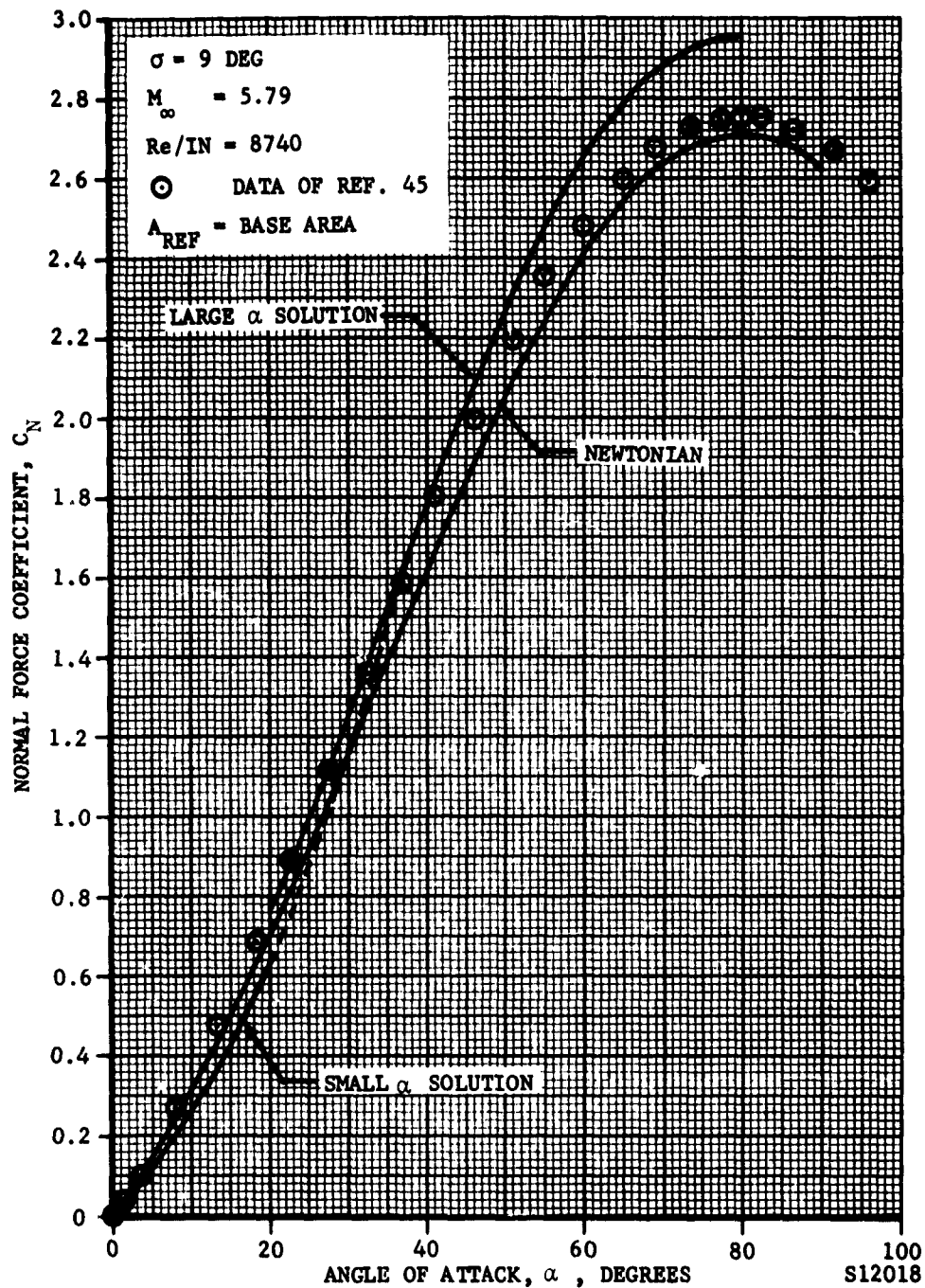
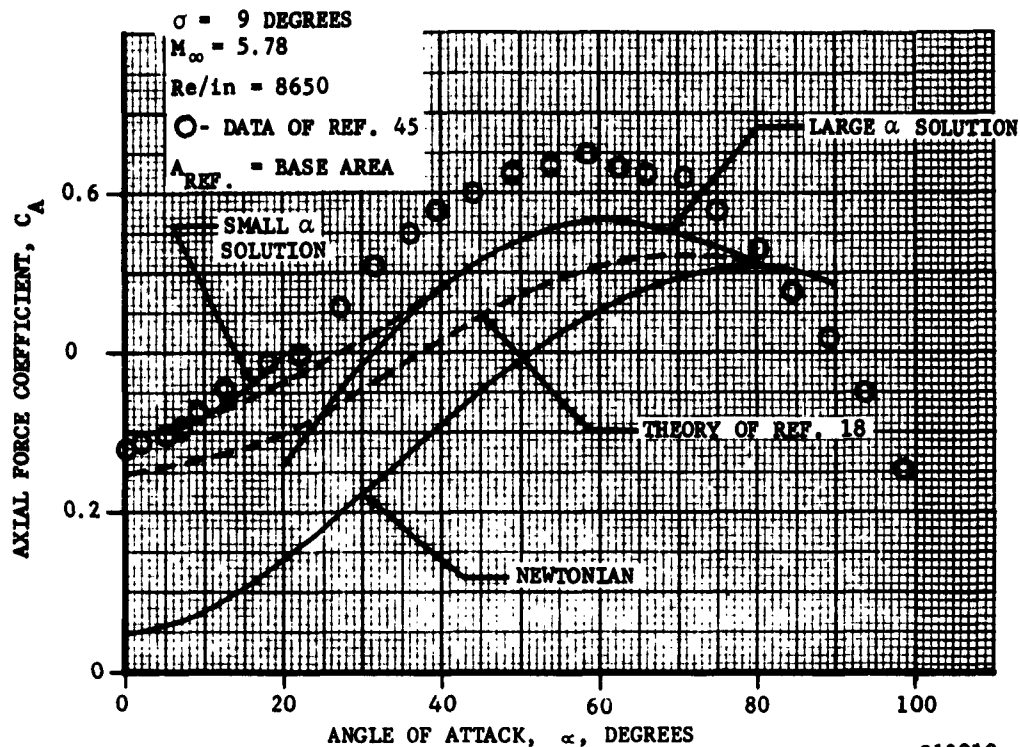
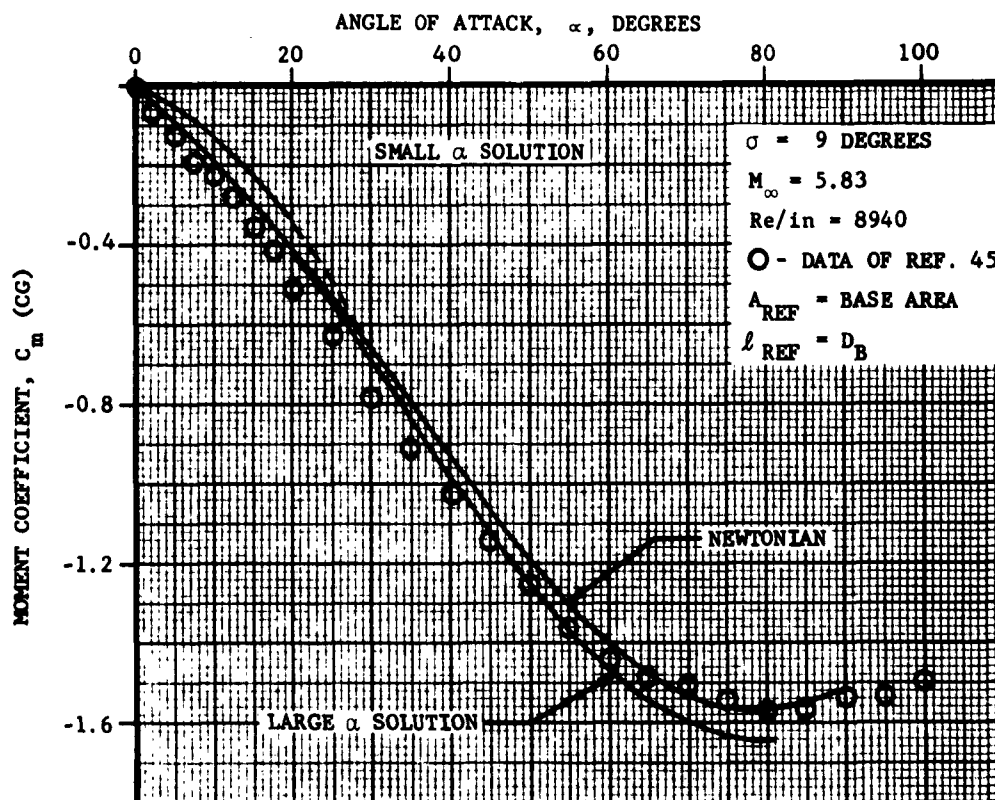


FIGURE 7-3. COMPARISON OF THEORY AND EXPERIMENT (NORMAL COEFFICIENT).



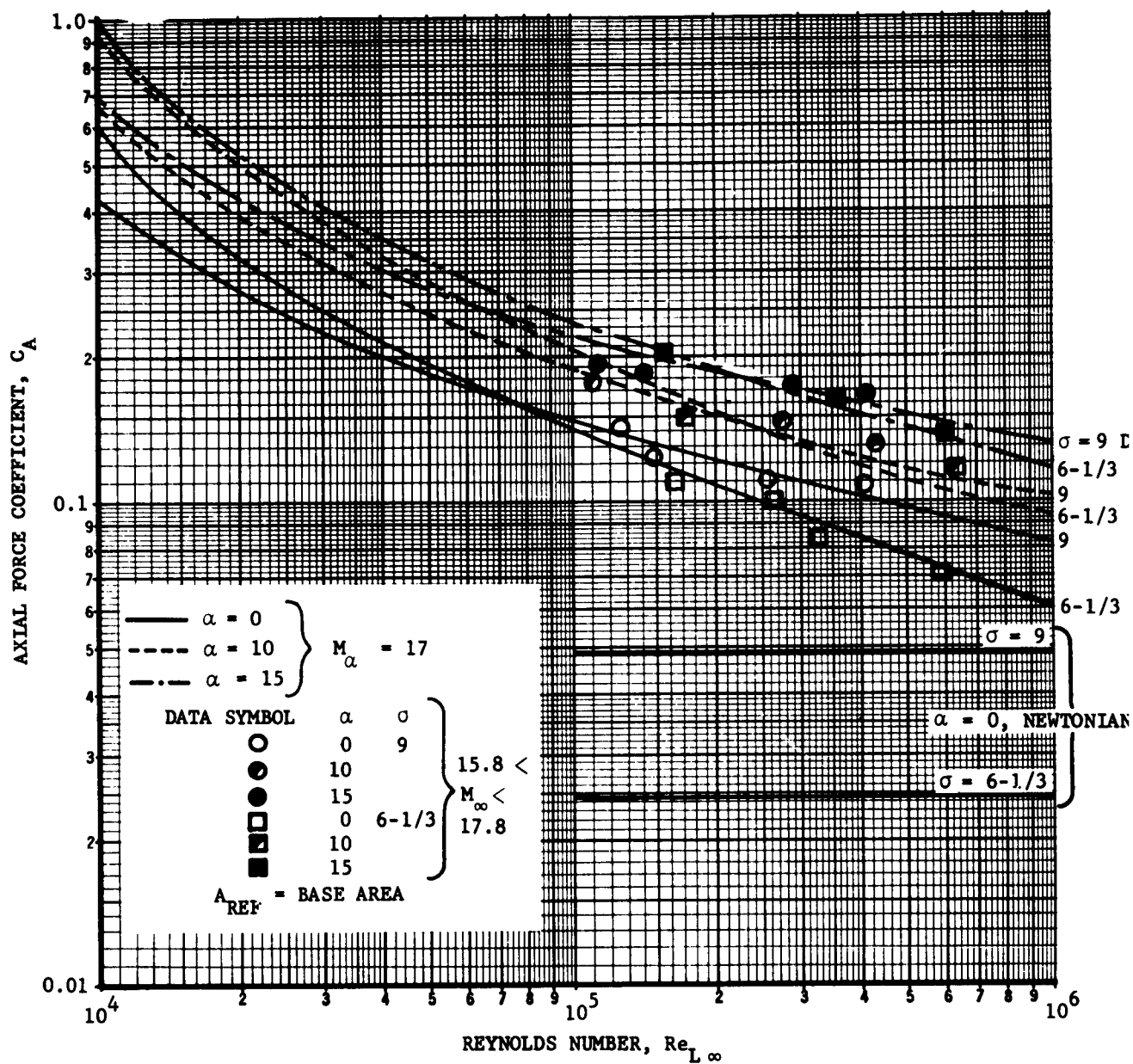
S12019

FIGURE 7-4. COMPARISON OF THEORY AND EXPERIMENT AXIAL COEFFICIENTS



S12020

FIGURE 7-5. COMPARISON OF THEORY AND EXPERIMENT (MOMENT COEFFICIENTS)



S12021

FIGURE 7-6. COMPARISON OF THEORY AND EXPERIMENT (AXIAL FORCE COEFFICIENT)

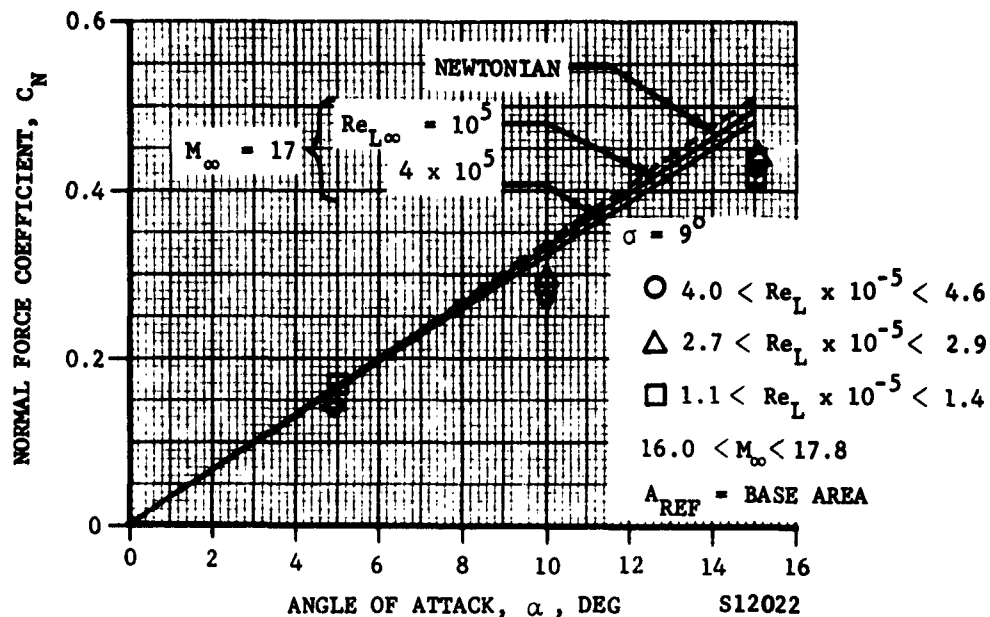


FIGURE 7-7. COMPARISON OF THEORY AND EXPERIMENT (NORMAL FORCE COEFFICIENT)

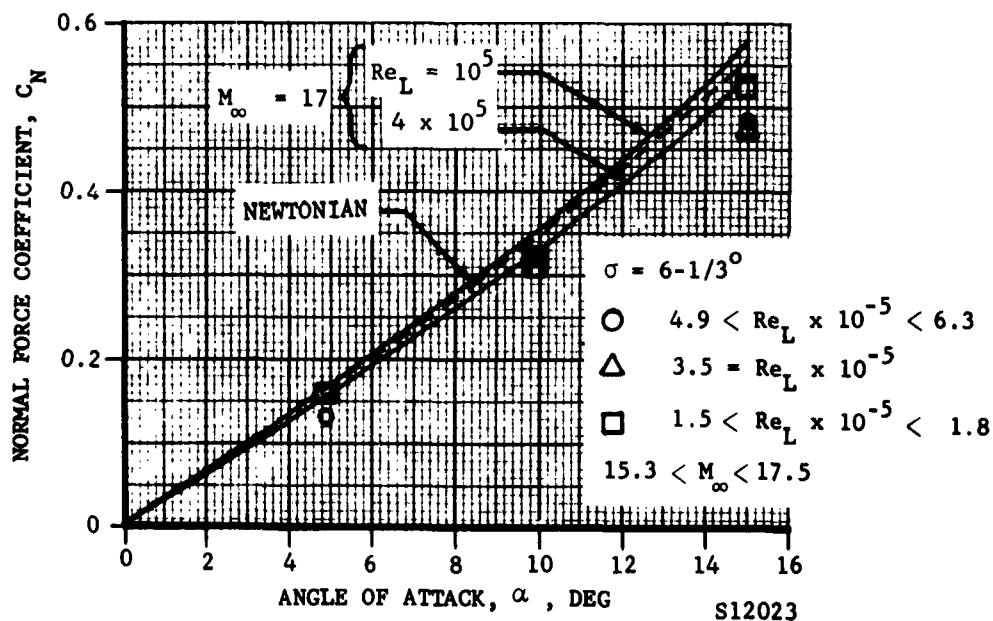


FIGURE 7-8. COMPARISON OF THEORY AND EXPERIMENT (NORMAL FORCE COEFFICIENT)

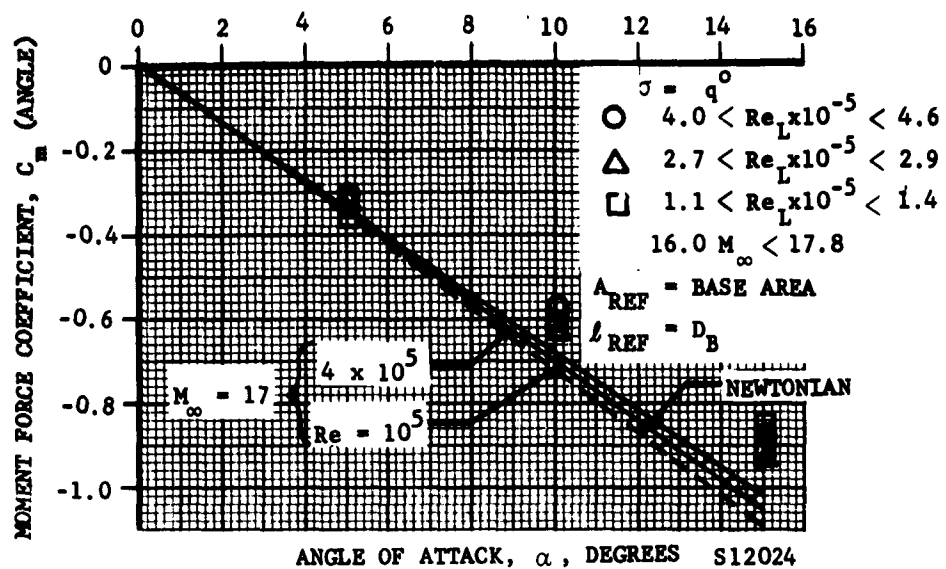


FIGURE 7-9. COMPARISON OF THEORY AND EXPERIMENT (MOMENT FORCE COEFFICIENT)

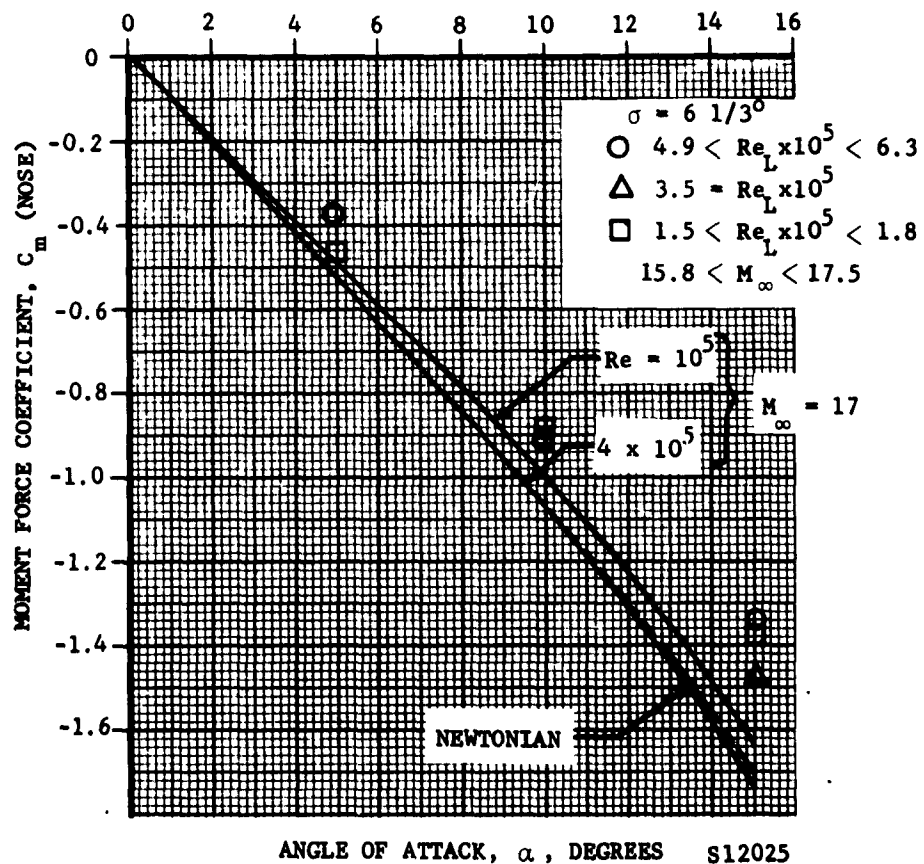


FIGURE 7-10. COMPARISON OF THEORY AND EXPERIMENT (MOMENT FORCE COEFFICIENT)

Ford Motor Company
AERONUTRONIC DIVISION

and moment forces, but are seriously underestimated by Newtonian theory in the case of the axial forces. The latter condition is caused by large viscous interaction effects at small α , and non-negligible skin friction contributions at large α . According to Reference 45, trailing edge drag effects could also be present at large α which might partially account for the increase of experimental values over the predicted ones.

The contribution of the back side of the cone to the forces was found to be very important in the region $\alpha > \sigma$ at small angle of attack. The method described in Section 7.3 was employed to estimate the various contributions to the total force. It was found that the magnitude of the skin friction forces on the back side was of the same order as that on the front side. The viscous interaction effects tend to compensate for the decrease in dynamic pressure. In the case of the axial force (Figure 7-4), this provides a continuous increase in C_A with increasing α , corresponding to the experimental results. In the case of the normal and moment forces (Figures 7-3 and 7-5), the skin friction forces on the front and back side tend to cancel each other, thereby contributing very little to the net forces in the low-density flow. An examination of the pressure forces acting on the cone was sufficient for an approximate analysis of the normal and moment forces.

The unavailability of high Mach number data characteristic of re-entry has prompted Aeronutronic to initiate a series of tests to correct this deficiency. The first information obtained on sharp cones of 6-1/3- and 9-degree semi-vertex angle was obtained in the AEDC Von Karman Gas Dynamics Facility in Hotshot Tunnel Number 1 by ARO, Inc. Aerodynamic forces were measured for $0 \leq \alpha \leq 15$ degrees. Test conditions and geometry were as follows:

| σ | Axial Length | D_N/D_B | T_w/T_t | T_∞ | M_∞ | $Re_{\infty L}$ |
|----------|--------------|-----------|-----------|------------|------------|---------------------------|
| 9° | 8.00 in. | 0.03 | ~ 0.1 | ~ 55°K | ~ 17 | 10^5 to 6×10^5 |
| 6-1/3° | 11.34 in. | 0.03 | ~ 0.1 | ~ 55°K | ~ 17 | 10^5 to 6×10^5 |

This data has been examined and compared with theory in Figures 6-10 to 6-14.

In Figure 7-6, the viscous interaction effects become apparent on the axial force coefficient. Theory predicts a crossover of the 6-1/3- and 9-degree cone curves, with the 6-1/3-degree cone having greater values of C_A at the lower Reynolds numbers. This is caused by the increased skin friction due to the transverse curvature effect. Theory also predicts

a change in the crossover to higher Reynolds numbers with increasing α . The data were obtained in this region where the crossover occurs, and tend to verify the predicted trends. In the case of the normal and moment force coefficients (Figures 7-7 and 7-9), the data for the 9-degree cone are lower than the Newtonian estimation, in contrast to the previous data of Reference 18, but in agreement with prediction at small α . For the 6-1/3-degree cone, the transverse curvature effect is sufficiently strong to increase the predicted values for $Re_{\infty L} = 10^5$ over the Newtonian. The experimental data, however, are still below the theoretical estimates. As the angle of attack continues to increase, the data should rise above the Newtonian, similar to the predicted trend in Figure 7-3. At the large angle of attack where the Newtonian estimate adequately accounts for the pressure contribution to the forces, any increase in the data over the Newtonian must be attributed to skin friction shear forces. These should always be relatively small in comparison to the pressure forces, although not necessarily negligible.

The methods outlined previously have also been applied to conditions obtained in the Cornell Aeronautical Labs' shock tunnel for hypersonic flow data. The tests were conducted for Aeronutronic under BSD contract to ARO, Inc., as an extension to a current ARO contract. The comparison of the theory with experiment is presented in Figure 7-11 for the axial force coefficient, and in Figures 7-12 and 7-13 for the normal and moment force data, respectively. Tabulated data are given in Table III for all of the force measurements. The tabulated data also include measurements on a blunt 6.34° half-angle cone.

The agreement between theory and experiment for the sharp cones is found to be good. The viscous interaction and transverse curvature effects are strongly exhibited in the axial force data (Figure 7-11). At the same length Reynolds number, the data for 6.34° cone are seen to crossover the data for the 9-degree cone as α increases, and actually becomes larger than the 9-degree cone data. The zero angle of attack data exhibit the same characteristics. It is noted that the disagreement between Newtonian theory and experiment in the case of the moment force data is not as bad as might seem from a cursory examination. In the form presented, the accuracy of the data is probably ± 50 percent or greater, and is really a measure of the agreement between theory and experiment of the center of pressure location. On this basis, the agreement is considered good.

A comparison of the sharp and blunt 6.34° cone axial force data are given in Figure 7-14. The viscous interaction effects become even more evident for this case, as the axial force data for the sharp cone has increased to equal that of the blunt cone over the Reynolds number range examined.

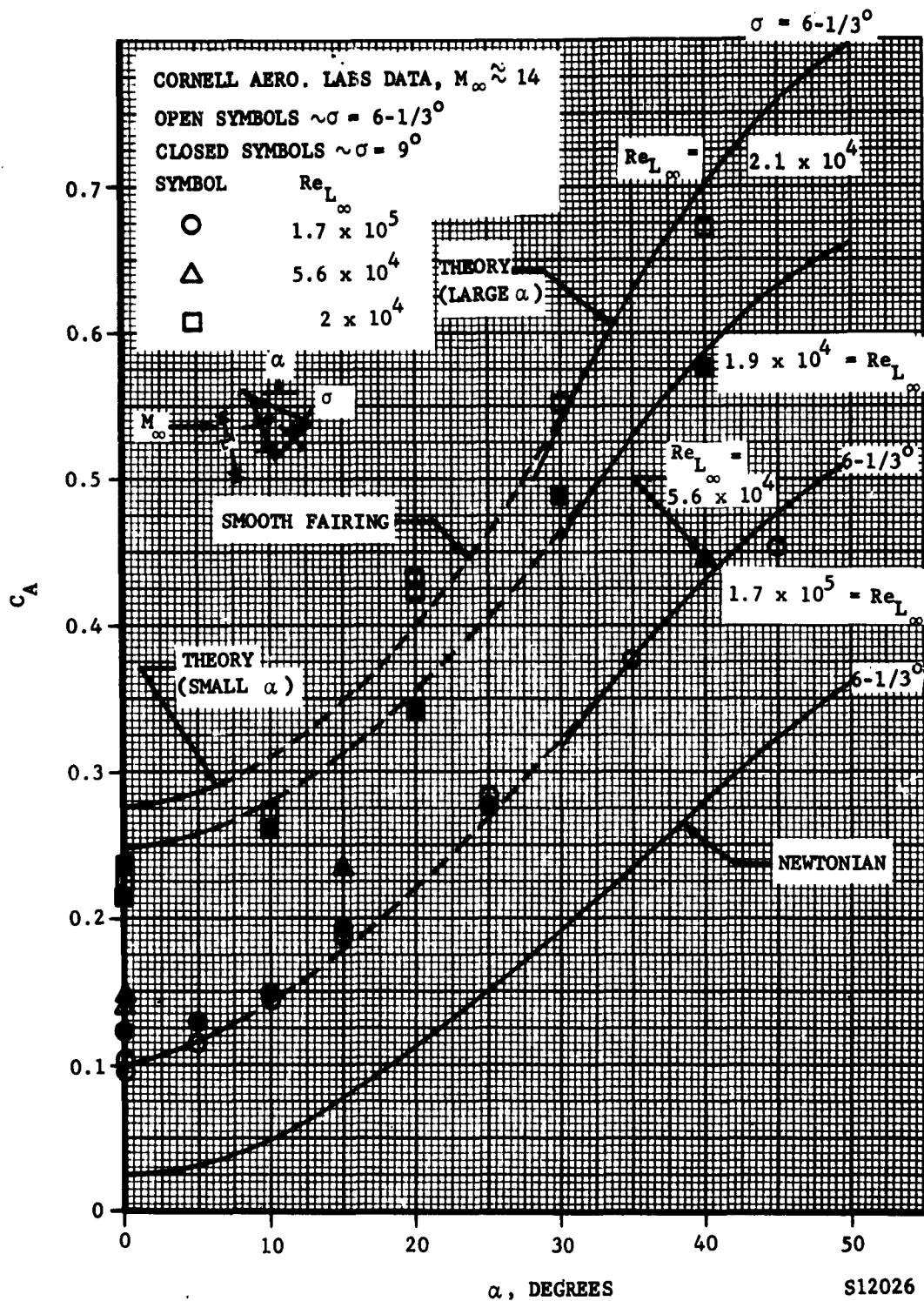
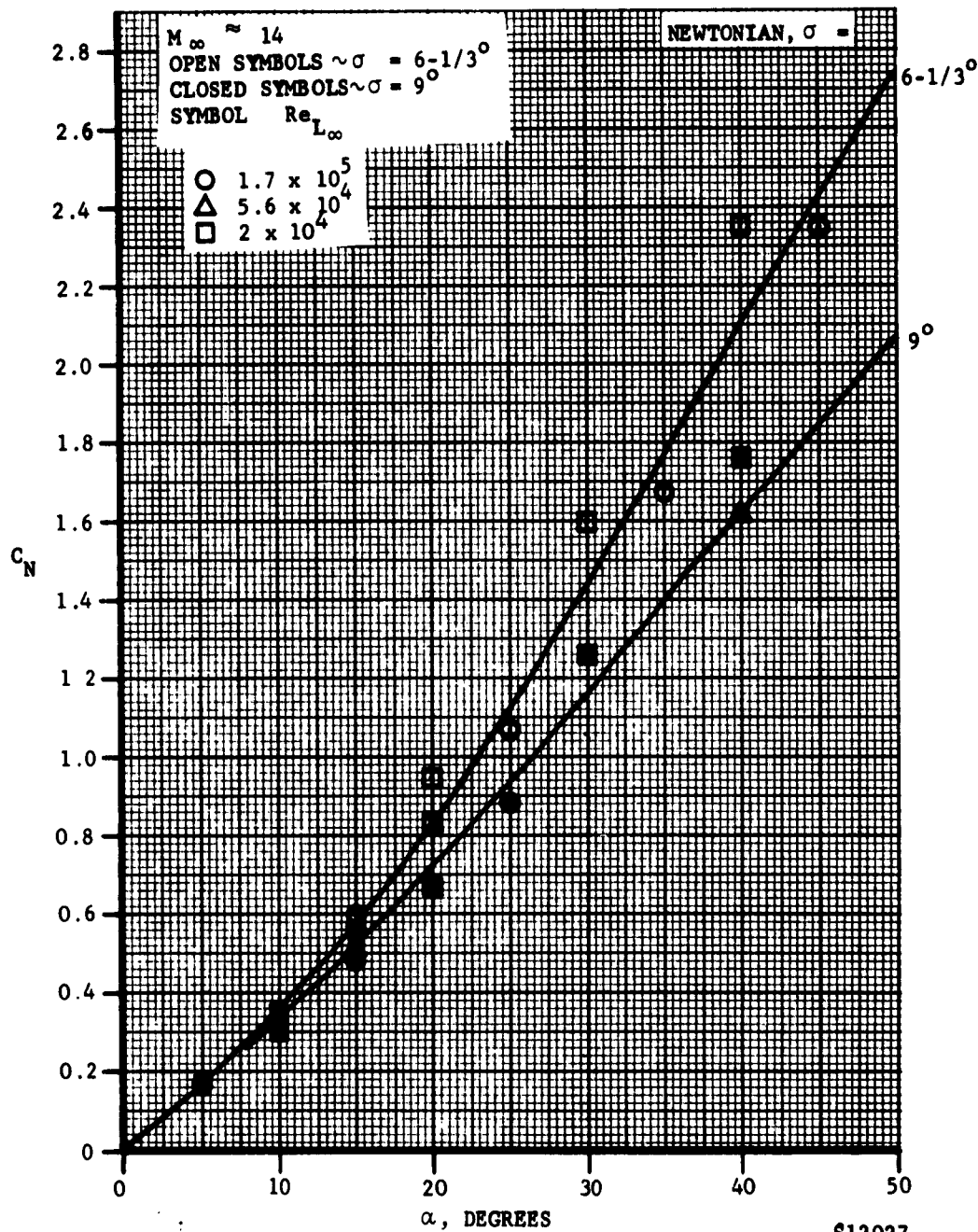


FIGURE 7-11. AXIAL FORCE COEFFICIENT VERSUS ANGLE OF ATTACK



S12027

FIGURE 7-12. NORMAL FORCE COEFFICIENT VERSUS ANGLE OF ATTACK

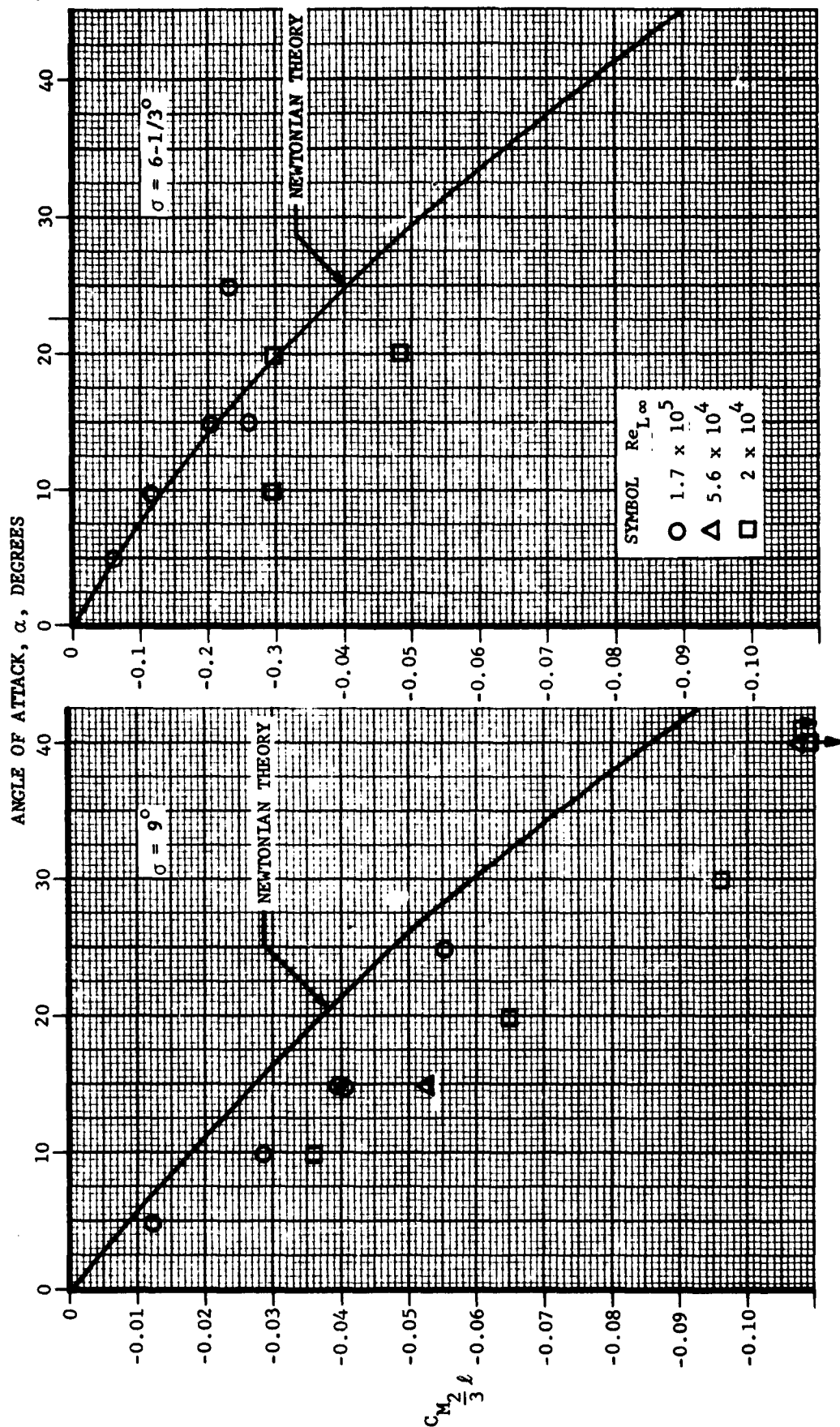


FIGURE 7-13. MOMENT FORCE COEFFICIENT VERSUS ANGLE OF ATTACK ($M_\infty \approx 14$)

S12028

TABLE III

$l_{ref} = D_B$
 $A_{ref} = A_B$
 l = model length from theoretical
nose

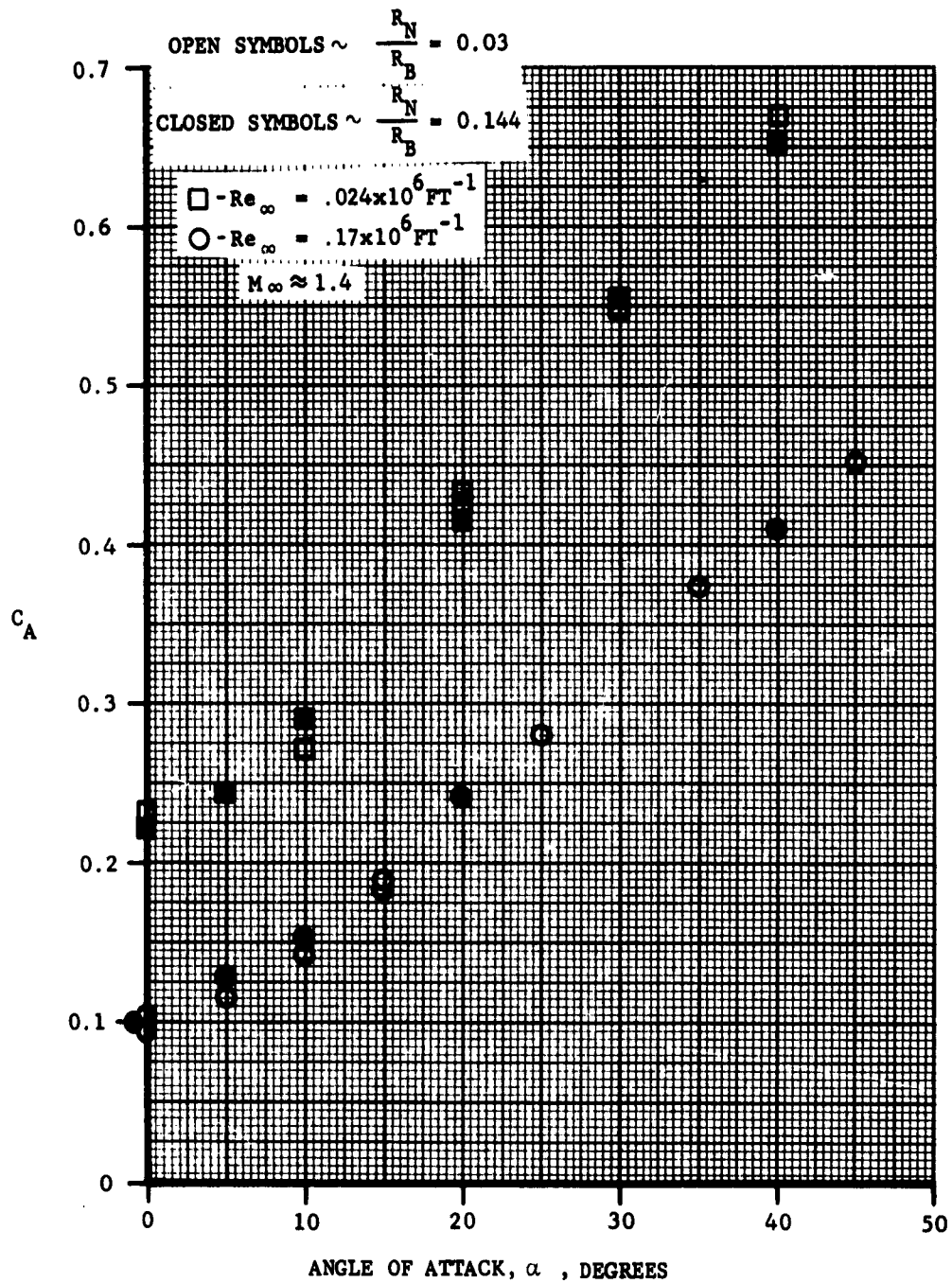
| RUN NO. | σ , DEGREES | R_N/R_B | M_∞ | Re_∞ FT ⁻¹ $\times 10^{-6}$ | α , DEGREES | C_A | C_N | C_M (about 2/3 l) | BASE DIAMETER INCHES |
|---------|-----------------------|-----------|------------|---|-----------------------|--------|---------|------------------------------|----------------------------|
| 1 | 9 | 0.03 | 14.86 | 0.193 | 0 | 0.1228 | 0.0008 | -0.0002 | 3.0 |
| 2 | 9 | 0.03 | 14.72 | 0.180 | 5 | 0.1301 | 0.1617 | -0.0127 | 3.0 |
| 3 | 9 | 0.03 | 14.70 | 0.182 | 10 | 0.1485 | 0.3165 | -0.0291 | 3.0 |
| 4 | 9 | 0.03 | 14.67 | 0.172 | 15 | 0.1891 | 0.5006 | -0.0398 | 3.0 |
| 6 | 9 | 0.03 | 14.65 | 0.171 | 15 | 0.1943 | 0.4924 | -0.0403 | 3.0 |
| 5 | 9 | 0.03 | 14.67 | 0.169 | 25 | 0.2756 | 0.8821 | -0.0555 | 3.0 |
| 7 | 9 | 0.03 | 13.63 | 0.022 | 0 | 0.2196 | 0.0014 | -0.0003 | 3.0 |
| 12 | 9 | 0.03 | 13.64 | 0.023 | 0 | 0.2363 | 0.0087 | 0.0015 | 3.0 |
| 8 | 9 | 0.03 | 13.70 | 0.023 | 10 | 0.2604 | 0.3077 | -0.0363 | 3.0 |
| 9 | 9 | 0.03 | 13.75 | 0.024 | 20 | 0.3416 | 0.6686 | -0.0652 | 3.0 |
| 10 | 9 | 0.03 | 13.73 | 0.024 | 30 | 0.4888 | 1.2528 | -0.0966 | 3.0 |
| 11 | 9 | 0.03 | 13.87 | 0.024 | 40 | 0.5758 | 1.7534 | -0.1509 | 3.0 |
| 13 | 9 | 0.03 | 14.36 | 0.068 | 0 | 0.1482 | -0.003 | 0.0002 | 3.0 |
| 14 | 9 | 0.03 | 14.30 | 0.065 | 15 | 0.2373 | 0.5151 | -0.0523 | 3.0 |
| 15 | 9 | 0.03 | 14.31 | 0.065 | 40 | 0.4456 | 1.6165 | -0.1263 | 3.0 |
| 16 | 6.34 | 0.03 | 14.66 | 0.172 | 0 | 0.0988 | -0.0017 | 0.009 | 2.375 |
| 21 | 6.34 | 0.03 | 14.64 | 0.168 | 0 | 0.1031 | -0.0008 | 0.0005 | 2.375 |
| 17 | 6.34 | 0.03 | 14.65 | 0.171 | 5 | 0.1177 | 0.1672 | -0.0066 | 2.375 |
| 18 | 6.34 | 0.03 | 14.64 | 0.170 | 10 | 0.1457 | 0.3480 | -0.0117 | 2.375 |
| 19 | 6.34 | 0.03 | 14.61 | 0.167 | 15 | 0.1917 | 0.5960 | -0.0269 | 2.375 |
| 22 | 6.34 | 0.03 | 14.63 | 0.168 | 15 | 0.1886 | 0.5638 | -0.0205 | 2.375 |

TABLE III (Continued)

$l_{ref} = D_B$
 $A_{ref} = A_B$
 l = model length from
theoretical nose

| RUN NO. | α , DEGREES | R_N/R_B | M_∞ | Re_∞ FT^{-1} $\times 10^{-6}$ | α , DEGREES | C_A | C_N | C_M (about 2/3 l) | BASE DIAMETER INCHES |
|---------|-----------------------|-----------|------------|--|-----------------------|--------|---------|------------------------------|----------------------------|
| *20 | 6.34 | 0.03 | 14.64 | 0.171 | 25 | 0.2828 | 1.0631 | -0.0232 | 2.375 |
| 23 | 6.34 | 0.03 | 13.79 | 0.024 | 0 | 0.2323 | 0.0106 | 0.0087 | 2.375 |
| 27 | 6.34 | 0.03 | 14.36 | 0.067 | 0 | 0.1413 | -0.0003 | -0.0046 | 2.375 |
| 28 | 6.34 | 0.03 | 13.65 | 0.022 | 0 | 0.2219 | 0.0065 | 0.0020 | 2.375 |
| 24 | 6.34 | 0.03 | 13.72 | 0.023 | 10 | 0.2720 | 0.3460 | -0.0294 | 2.375 |
| 25 | 6.34 | 0.03 | 13.65 | 0.022 | 20 | 0.4332 | 0.9477 | -0.0489 | 2.375 |
| 30 | 6.34 | 0.03 | 13.77 | 0.024 | 20 | 0.4239 | 0.8330 | -0.0297 | 2.375 |
| *26 | 6.34 | 0.03 | 13.69 | 0.023 | 30 | 0.5516 | 1.5918 | -0.0443 | 2.375 |
| *29 | 6.34 | 0.03 | 13.72 | 0.023 | 40 | 0.6720 | 2.3421 | -0.0381 | 2.375 |
| *31 | 6.34 | 0.03 | 14.59 | 0.171 | 35 | 0.3756 | 1.6705 | -0.0177 | 2.375 |
| *32 | 6.34 | 0.03 | 14.54 | 0.162 | 45 | 0.4529 | 2.3402 | -0.0053 | 2.375 |
| 33 | 6.34 | 0.144 | 14.59 | 0.162 | 0 | 0.1007 | -0.0030 | -0.0007 | 2.375 |
| 34 | 6.34 | 0.144 | 14.59 | 0.166 | 5 | 0.1240 | 0.1549 | -0.0384 | 2.375 |
| 45 | 6.34 | 0.144 | 14.62 | 0.165 | 5 | 0.1275 | 0.1548 | -0.0389 | 2.375 |
| 35 | 6.34 | 0.144 | 14.60 | 0.170 | 10 | 0.1531 | 0.3256 | -0.0426 | 2.375 |
| 36 | 6.34 | 0.144 | 14.61 | 0.166 | 20 | 0.2432 | 0.7752 | -0.0522 | 2.375 |
| 46 | 6.34 | 0.144 | 14.63 | 0.166 | 40 | 0.4115 | 2.1096 | -0.0546 | 2.375 |
| 37 | 6.34 | 0.144 | 13.63 | 0.023 | 0 | 0.2217 | 0.0015 | 0.0040 | 2.375 |
| 38 | 6.34 | 0.144 | 13.72 | 0.024 | 5 | 0.2447 | 0.1689 | -0.0426 | 2.375 |
| 39 | 6.34 | 0.144 | 13.67 | 0.024 | 10 | 0.2928 | 0.3694 | -0.0535 | 2.375 |
| 40 | 6.34 | 0.144 | 13.67 | 0.023 | 20 | 0.4194 | 0.8791 | -0.0846 | 2.375 |
| 42 | 6.34 | 0.144 | 13.80 | 0.024 | 30 | 0.5567 | 1.6587 | -0.1105 | 2.375 |
| 41 | 6.34 | 0.144 | 13.76 | 0.024 | 40 | 0.6576 | 2.4687 | -0.1669 | 2.375 |

* Validity of moment force data is questionable.



S12029
 FIGURE 7-14. COMPARISON OF C_A FOR SHARP AND BLUNT SLENDER CONES
 AT ANGLE OF ATTACK

Ford Motor Company,
AERONUTRONIC DIVISION

In conclusion, a reasonable engineering approximation to the forces acting on sharp, slender cones, even with low-density flow effects, would be to apply Newtonian estimates for the normal and moment forces in hypersonic flow. The axial forces, however, must consider the viscous interaction effects which greatly increase both the pressure and skin friction contributions.

CHAPTER 8

NOMENCLATURE

| | | |
|-----------------|---|---|
| a_1, a_2, a_3 | = | coefficients given by Equation 5.20 |
| a_1, η_b | = | parameters describing shock shape in hypersonic small disturbance theory (equation 3.26) |
| A | = | area |
| A_b | = | cone base area |
| A, B | = | coefficients given in Equation 2.2 |
| C | = | coefficient in linear viscosity-temperature relationship, $\mu / \mu_e = C T / T_e$ |
| C_p | = | specific heat |
| c_p | = | pressure coefficient |
| C_f | = | local skin friction coefficient \equiv shear force/ $q_\infty A_c$ |
| C_F | = | mean skin friction coefficient \equiv total shear force/ $q_\infty A_c$ |
| C_D | = | drag coefficient, $D/q_\infty A_b$ |
| C_A | = | axial force coefficient |
| C_N | = | normal force coefficient |
| C_M | = | moment force coefficient |
| d, G | = | coefficients expressing heat transfer effects in viscous interaction theories, Equations 2.2, 2.7 |
| D | = | cone base diameter |
| E | = | Equation 5.9 |

NOMENCLATURE (Continued)

| | |
|------------|---|
| F_c | = coefficient given by Equation 2.22 |
| F_o, F_1 | = Equations 3.13, 3.14 |
| f_p | = function describing induced pressures in strong interaction region (equation 2.8) |
| f_δ | = function describing boundary layer thickness in strong interaction region (equations 2.2a, 2.2b) |
| h | = static enthalpy also, heat transfer coefficient |
| H | = total enthalpy |
| I_1 | = integral given in Equation 2.9 |
| J_1, J_2 | = coefficients given in Equations 2.3 and 2.4 |
| K | = hypersonic similarity parameter, $M_\infty \theta_b$ also, constant of proportionality in boundary layer growth, $\delta^* = Kx^n$ |
| L | = slant length |
| l | = length |
| M | = Mach number |
| m | = exponent describing power law body, $r_b \propto x^m$ |
| n | = exponent describing boundary layer growth, $\delta^* \propto x^n$ |
| P | = pressure |
| Pr | = Prandtl number |
| Q/A | = heat flux |
| q | = dynamic pressure |

NOMENCLATURE (Continued)

| | |
|------------|--|
| R | = cylindrical radius of shock wave also, gas constant also, equivalent radius of curvature |
| Re | = Reynolds number |
| r | = local cylindrical radius |
| St | = Stanton number |
| T | = temperature |
| T* | = reference temperature |
| u, v | = velocity components |
| x, y | = coordinate system dimensions, x taken along slant length, and y normal to surface |
| Z | = compressibility factor in equation of state |
| α | = angle of attack |
| β | = shock shape parameter $\frac{1}{m} - 1$ also, pressure gradient parameter, $-\frac{\gamma-1}{\gamma} \cdot \frac{n}{1+n}$ |
| γ | = ratio of specific heats |
| δ | = boundary layer thickness |
| δ^* | = displacement thickness |
| ϵ | = density ratio, ρ_1/ρ_2 |
| θ | = total flow deflection angle |
| θ_s | = angle between local tangent to shock wave and body axis (shock angle) |
| θ_b | = local body angle |
| λ | = non-dimensional distance, Equation 3.6 |

NOMENCLATURE (Continued)

| | |
|--------------|---|
| μ | = viscosity |
| ζ | = Equation 3.15 |
| ρ | = density |
| σ | = semi-vertex angle of sharp cone |
| $\bar{\chi}$ | = viscous interaction parameter, $M^3 \sqrt{C} / \sqrt{Re}$ |
| ϕ | = circumferential body angle ($\phi = 0$ at stagnation line) |
| Λ | = angle of yaw |
| Δ | = shock standoff distance |

Subscripts

| | |
|----------|--|
| 0, orig | = original inviscid value, also stagnation value |
| w | = wall |
| c | = cone |
| t | = total, or stagnation value |
| e | = local value at edge of boundary layer |
| 1,2 | = values before and after shock wave, respectively |
| ∞ | = freestream |
| b | = body, or base |
| M | = Mangler solution |
| Aw | = adiabatic wall |
| p | = local value |
| L | = slant length |

NOMENCLATURE (Continued)

Subscripts (continued)

| | | |
|-----|---|----------------------------|
| M | = | normal |
| s | = | shock |
| ref | = | reference value |
| FM | = | free molecule flow |
| P | = | pressure contribution |
| F | = | skin friction contribution |

CHAPTER 9

REFERENCES

1. Hayes, W. and Probstein, R., Hypersonic Flow Theory, Academic Press, New York, 1959.
2. Feldman, S., "Hypersonic Conical Shocks for Dissociated Air in Thermodynamic Equilibrium", Jet Propulsion, Vol. 27, No. 12, December 1957, pp 1253 - 1255.
3. Lees, L. and Probstein, R. F., "Hypersonic Flows of a Viscous Fluid", Princeton University Aeronautical Engineering Department (unpublished) 1953.
4. Probstein, R. F., "Interacting Hypersonic Laminar Boundary Layer Flow Over a Cone", Brown University Technical Report AF 2793/1, 1955.
5. Bertram, M. H., "Boundary-Layer Displacement Effects in Air at Mach Numbers of 6.8 and 9.6", NASA TR R-22, 1959.
6. Dewey, C. F., Jr., "The Use of Local Similarity Concepts in Hypersonic Viscous Interaction Problems, and Application to Yawed Lifting Surfaces with Mass Transfer", ARS Preprint No. 2207-61, presented at ARS Space Flight Report to the Nation, New York, October 9-15, 1961.
7. Van Driest, E. R., "Investigation of Laminar Boundary Layer in Compressible Fluids Using the Crocco Method", NACA TN 2597, January, 1952.
8. Talbot, L., Koga, T. and Sherman, P. M., "Hypersonic Viscous Flow Over Slender Cones", NACA TN 4327, September 1958.
9. Cheng, H. K., Hall, J. G., Golian, T. C., and Hertzberg, A., "Boundary-Layer Displacement and Leading-Edge Bluntness Effects in High-Temperature Hypersonic Flow", Journal of the Aerospace Sciences, Vol. 28, No. 5, May 1961, pp 353-380.
10. Sommer, S. C. and Short, B. J., "Free-Flight Measurements of Turbulent Boundary-Layer Skin Friction in the Presence of Severe Aerodynamic Heating at Mach Numbers From 2.8 to 7.0", NACA TN 3391, 1955.

REFERENCES (Continued)

11. Eckert, E. R. G., "Survey on Heat Transfer at High Speeds", WADC TR-54-70, University of Minnesota, April 1954.
12. Lees, L., "Note on the Hypersonic Similarity Law for an Unyawed Cone", Reader's Forum, Journal of the Aeronautical Sciences, Vol. 18, No. 10, pp 700-702, October 1951.
13. Moore, F. K., "On Local Flat-Plate Similarity in the Hypersonic Boundary Layer", J. Aerospace Sciences, Vol. 28, n 10, October 1961, pp 753-762.
14. deSoto, S., and Woft, H., "Application of the Mangler Transformation in Boundary Layer Flow", ARS Journal, Vol. 31, n 4, April 1961, pp 553-555.
15. Reshotko, E., "Laminar Boundary Layer with Heat Transfer on a Cone at Angle of Attack in a Supersonic Stream", NACA TN 4152, December 1957.
16. Probstein, R. F., and Elliott, D., "The Transverse Curvature Effect in Compressible Axially Symmetric Laminar Boundary-Layer Flow", J. Aero Science, Vol. 23, n. 3, March 1956, pp 208-224, 236.
17. Talbot, L., Koga, T., and Sherman, P. M., "Hypersonic Viscous Flow over Slender Cones", NACA TN 4327, September 1958.
18. Van Dyke, M. D., "A Study of Hypersonic Small-Disturbance Theory", NACA Report 1194, 1954.
19. Mirels, H., "Approximate Analytical Solutions for Hypersonic Flow Over Slender Power Law Bodies", NASA Tech. Rpt. R-15, 1959.
20. Moeckel, W. E., and Weston, K. C., "Composition and Thermodynamic Properties of Air in Chemical Equilibrium", NACA TN 4265, April 1958.
21. Li, T. Y. and Nagamatsu, H. T., "Similar Solutions for Compressible Boundary Layer Equations", GALCIT Memo No. 22, September 10, 1954.
22. Lukasiewicz, J., Whitfield, J. D., and Jackson, R., "Aerodynamic Testing at Mach Numbers from 15 to 20", ARS Preprint 1969-61, August 1961.

REFERENCES (Continued)

36. Gonor, A. L., "Location of Frontal Wave in Asymmetrical Flow of Gas at High Supersonic Speed Over a Pointed Body", Russian Supplement, Vol. 30, No. 9, ARS Journal, September 1960, pp 841-842.
37. Conti, R. J., "Laminar Heat Transfer and Pressure Measurements at a Mach Number of 6 on Sharp and Blunt 15° Half-Angle Cones at Angles of Attack up to 90°", NASA TN D-962, October 1961.
38. Amick, J. L., "Pressure Measurements on Sharp and Blunt 5°- and 15°- Half-Angle Cones at Mach Number 3.86 and Angles of Attack to 100°", NASA TN D-753, February 1961.
39. Edwards, A. C., and Francis, W. L., "Turbulent Heat Transfer on Blunt Bodies at Supersonic and Hypersonic Speeds", Lockheed Report No. 14978 (LAC/557191), 14 April 1961 (Title Unclassified), SECRET.
40. Love, E. S., "A Reexamination of the Use of Simple Concepts for Predicting the Shape and Location of Detached Shock Waves", NACA TN 4170, December 1957.
41. Seaman, D. J., and Dore, F. J., "Force and Pressure Coefficients of Elliptic Cones and Cylinders in Newtonian Flow", Report No. ZA-7-004, San Diego Division, CONVAIR, 16 May 1952.
42. Reshotko, E. and Beckwith, I. E., "Compressible Laminar Boundary Layer Over a Yawed Infinite Cylinder with Heat Transfer and Arbitrary Prandtl Number", NACA Report 1379, 1958 (Supersedes NACA TN 3986).
43. Beckwith, I. E., "Similar Solutions for the Compressible Boundary Layer on a Yawed Cylinder with Transpiration Cooling", NASA TR R-42, 1959.
44. Beckwith, I. E., and Cohen, N. B., "Application of Similar Solutions to Calculation of Laminar Heat Transfer on Bodies with Yaw and Large Pressure Gradient in High-Speed Flow", NASA TN D-625, January 1961.
45. Maslach, G. J., and Talbot, L., "Low Density Aerodynamic Characteristics of a Cone at Angle of Attack", Tech Report HE-150-172, Inst. Eng. Res. Univ. of California, Berkeley, California, October 30, 1959.

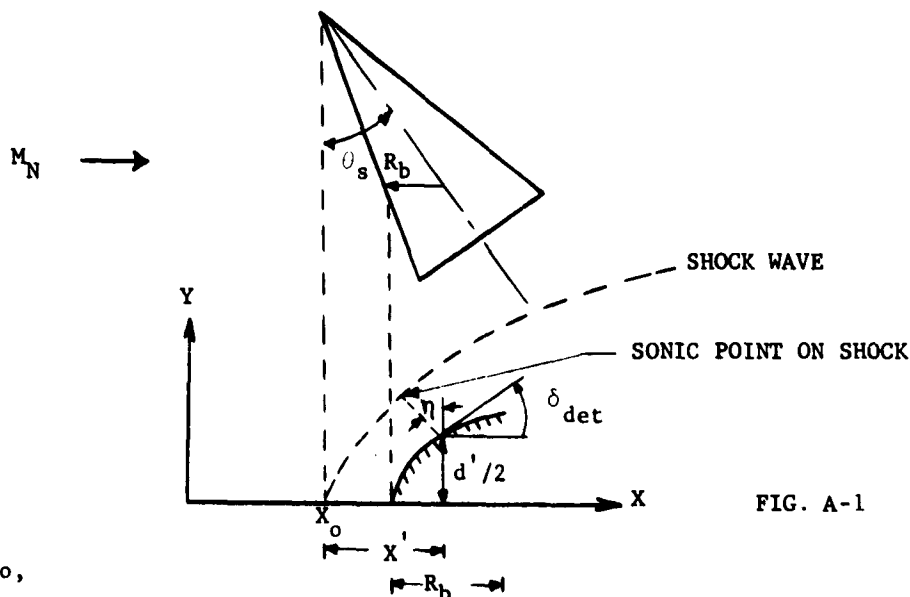
REFERENCES (Continued)

23. Kavanau, L. L., "Base Pressure Studies in Rarefied Supersonic Flows", J. Aero. Sci. Vol. 23, n 3, March 1956, p 193.
24. Schlichting, H., "Boundary Layer Theory", Pergamon Press, New York, 1955.
25. Lehnert, R. and Schermerhorn, V. L., "Correlation of Base Pressure and Wake Structure of Short and Blunt-Nose Cones with Reynolds Number Based on Boundary-Layer Momentum Thickness", Journal of Aero/Space Sciences, Vol. 26, No. 3, pp 185, March 1959.
26. Aeronutronic Test PA-1, NOL Ballistic Range (unpublished).
27. Experimental Investigation of the Aerodynamic Characteristics of a 9 Degree Half-angle Cone at Mach Number 9, Aeronutronic Report 1638.
28. Aeronutronic Test PA-4, Arnold Center Hotshot 1 (unpublished).
29. Aeronutronic Test PA-7, Corness (unpublished).
30. Moore, F. K., "Laminar Boundary Layer on Cone in Supersonic Flow at Large Angle of Attack", NACA Report 1132, 1953.
31. Brunk, W. E., "Approximate Method for Calculation of Laminar Boundary Layer with Heat Transfer on a Cone at Large Angle of Attack in Hypersonic Flow", NACA TN 4380, September 1958.
32. Kopal, Z. (ed.), "Tables of Supersonic Flow Around Cones", Tech. Report No. 1, Dept. Eng., M.I.T., 1947.
33. Kopal, Z. (ed.), "Tables of Supersonic Flow Around Yawing Cones", Tech. Report No. 3, Dept. Elec. Eng., M.I.T., 1947.
34. Kopal, Z. (ed.), "Tables of Supersonic Flow Around Cones of Large Yaw", Tech. Report No. 5, Dept. Elec. Eng., M.I.T., 1949.
35. Gonor, A. L., "Flow Over a Cone at an Angle of Attack for High Mach Number", Russian Supplement, Vol. 32, No. 1, ARS Journal, January 1962., pp 130-132.

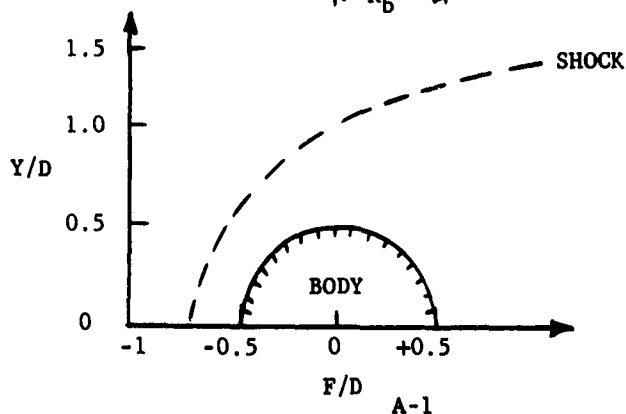
APPENDIX

PROCEDURE FOR CALCULATING SHOCK SHAPE AT LARGE ANGLES OF ATTACK

The slender cone is assumed to act as a cylinder with an equivalent radius of curvature, R_b (equation 6.3 of text). At large angles of attack a swept cylinder is approximately equivalent to another cylinder which is unswept to the normal Mach number component, M_N . If a slender cone is considered whose equivalent freestream Mach number is $M_N = M_\infty \sin(\theta_s + \alpha)$, the results of Love may be applied to determine the local shock slope relative to the direction M_N :



also,



Ford Motor Company
AERONUTRONIC DIVISION

The input quantities required to compute the shock wave are:

$$M_N = M_\infty \sin (\theta_s + \alpha)$$

$$\beta = \sqrt{M_N^2 - 1}$$

ϵ_s = shock angle (with respect to x = axis) that gives sonic velocity behind the shock wave (to be obtained from NACA Report 1135)

δ_{det} = semi-vertex angle of wedge that just produces shock detachment (NACA Report Number 1135)

$\left. \begin{matrix} C_c \\ \eta \end{matrix} \right\}$ = values from NACA TN 4170 for 2-dimensional circular face (e.g. cylinder normal to flow), see following tables:

| M_N | C_c | η , degrees |
|----------|-------|------------------|
| 1.0 | --- | 0 |
| 1.5 | --- | 4 |
| 1.6 | 0.780 | --- |
| 2.0 | .806 | 11.6 |
| 2.4 | .816 | --- |
| 2.5 | --- | 20.0 |
| 2.8 | .823 | --- |
| 3.0 | --- | 27.5 |
| 3.5 | --- | 34.5 |
| 3.6 | .836 | --- |
| 4.0 | --- | 41.0 |
| 4.4 | .845 | --- |
| 4.5 | --- | 46.5 |
| 5.0 | --- | 52.0 |
| 5.2 | .850 | --- |
| 5.5 | --- | 57.0 |
| 6.0 | .854 | 62.0 |
| 7.2 | .856 | --- |
| ∞ | 0.857 | ~137. |

Ford Motor Company
AERONUTRONIC DIVISION

The equations for the shock shape are as follows:

$$\frac{x'}{d'} = 0.50 C_c \cot \delta_{det} \quad A.1$$

$$\frac{x_o}{d'} = \frac{\beta \sqrt{\beta^2 \tan^2 \epsilon_s - 1} \left(\frac{x'}{d'} + \frac{\tan \eta}{2} \right)}{\beta^2 \tan \epsilon_s - \beta \sqrt{\beta^2 \tan^2 \epsilon_s - 1} + \tan \eta} \quad A.2$$

$$\frac{y}{d'} = \frac{1}{\beta} \sqrt{\left(\frac{x}{d'} \right)^2 - \left(\frac{x_o}{d'} \right)^2} \quad A.3$$

$$\frac{y}{D} = \frac{y}{d'} \cos \delta_{det} \quad A.4$$

$$\frac{F}{D} = \left(\frac{x}{d'} - \frac{x_o}{d'} \right) \cos \delta_{det} - \frac{\sin^2 \delta_{det} + C_c \cos^2 \delta_{det}}{2 \sin \delta_{det}} \quad A.5$$

The local shock slope is

$$\frac{dy}{dx} = (x/d') / \beta \sqrt{\left(\frac{x}{d'} \right)^2 - \left(\frac{x_o}{d'} \right)^2} \quad A.6$$

Experimental data indicates that the shock detachment distance given by equation 6.7 should be used. Then

$$d'/2 = R_b \cos \delta_{det} \quad A.7$$

and in place of equation A.1, we have

$$\frac{x'}{d'} = \left[\frac{\Delta}{R_b} + (1 - \sin \delta_{det}) \right] \bigg/ \frac{d'}{R_b} \quad A.1a$$